Molecular dynamics modelling of complex-rheology heat transfer liquids

Bharath Ravikumar

Department of Engineering
City, University of London

This dissertation is submitted for the degree of
Doctor of Philosophy

School of Science & Technology   July 2024

I would like to dedicate this thesis to all my teachers...

Declaration

I hereby declare that the content of this dissertation is original and has not been submitted in whole or in part for consideration for any other degree or qualification in this, or any other university. This dissertation is my own work, except where specific reference is made to a joint effort in the text and acknowledged accordingly. I have not used any AI tools to write the dissertation. The financial support for the research reported in the dissertation is provided by EU Framework Programme for Research and Innovation Horizon 2020 under the grant agreement number 899659 (I-BAT).

I grant powers of discretion to the University Librarian to allow the thesis to be copied in whole or in part without further reference to me. This permission covers only single copies made for study purposes, subject to normal conditions of acknowledgement.

<div align="right">

Bharath Ravikumar
July 2024

</div>

Acknowledgements

A long and an intense journey has come to its destination. The presented dissertation stands as a proof of all the work done during this time frame. However, the thesis would not be complete without acknowledging the efforts of some very important people.

Firstly, I wholeheartedly thank my supervisor Dr. Ioannis Karathanassis for entrusting me with the research. He was instrumental in guiding me at important junctures and providing me with the infrastructure for all the tasks carried out. He gave me all the encouragement and support to investigate novel areas, that would ultimately bring a professional researcher out of me. The learning curve did not feel hectic given his constant supervision.

Secondly, I express my gratitude to my second supervisor, Prof. Manolis Gavaises for being a voice of reason during the research. His involvement was essential in making my work presentable to a larger audience.

Additionally, I would like to express my sincere thanks to Dr. Tim Smith from Lubrizol UK, who was an exceptional collaborator throughout the process. I am grateful to my colleagues at ETH Zurich and FAU Erlangen, who made the I-BAT project, that this research contributed to, a successful endeavour.

I am extremely grateful to Dr. Raghuram Chetty, Dr. Mahesh Mynam and Dr. Beena Rai for having given me the greatest introduction possible to serious scientific research. No amount of gratitude will be enough to express how thankful I am towards my parents Anitha and Ravikumar, for having presented me excellent opportunities to pursue in my life. I remember my grandparents very fondly for being guiding lights in my life. I thank all my friends for being a great support in this voyage.

Lastly, to my wife and the love of my life, Arya- this would not have been possible without you on my side. Thank you.

Bharath

Abstract

Fluids of complex rheology (polymer solutions, nanofluids, biological specimens and so on) are utilised in consumer products, heavy industry as well as biomedical applications driving the technological advancements. They find uses in crude oil recovery, pharmaceuticals, micro-electromechanical systems, lubrication, and thermal management systems to name a few. Despite this, the behaviour of such fluids as a response to various physical conditions and external stimuli is yet to be elucidated convincingly. In the present study, novel heat transfer liquids are sought for immersive-cooling applications of electric vehicle (EV) battery thermal management systems (BTMS). The application limits the families of base solvents to dielectric compounds that can be utilised to design the coolants. Niche requirements such as this demand computational modelling and simulation methods suitable for the design and property predictions of the engineered fluids. The computational research in this field must be able to link the chemistry of the complex liquids to the anticipated heat transfer effectiveness performance in BTMS. Molecular dynamics (MD) simulations founded on statistical and Newtonian mechanics can provide insights into the relationship between the chemical structure and rheological behaviour of the non-Newtonian fluids. Additionally, a bottom-up approach of modelling the liquids based on MD can complement experimental studies. The current MD research on this front is severely scattered.

The research begins with the systematic study of oil-based polymer solutions that are compounds of interest in heat transfer applications. Atomistic MD studies are performed to obtain the structural, transport and rheological properties of the compounds. The addition of the polymer chain in oil shows the early onset of shear-thinning which helps maintain stable vortices, which in turn enhance heat transfer by disrupting the thermal boundary layer. At the same time, the thermal conductivity of the resultant solution increases with the addition of polymer. Satisfactory models based on the comparison of properties with atomistic MD simulations are used as building blocks for mesoscale many-body dissipative particle dynamics (mDPD) modelling. The coarse-grained (CG) mDPD simulations are capable of modelling the rheological behaviour of polymers solutions at spatial-temporal scales relevant to engineering. The CG modelling framework is able to reproduce the structural characteristics observed at atomistic scale MD. The modelling strategy is able to showcase the non-Newtonian behaviour

of oligomers and dilute polymer solutions, demonstrating the sensitivity of the model. Also, the mDPD model is able to distinguish the viscoelastic behaviour of polymers of different chemistries in a solution. Thus, the framework can bridge the information obtained at atomistic levels with the macroscale non-Newtonian behaviour.

An additional objective of the research is to investigate how the presence of the nanoparticles in such polymer solutions impacts the performance of the fluids as heat transfer media. Atomistic scale MD simulations of nanoparticles of different chemistries and shapes dispersed in the polymer solutions are performed. The investigation clearly shows higher thermal conductivities with the addition of nanoparticles. Subsequently, it is found that heat transfer coefficients of nanofluids in the presence of polymer chains are higher than in their absence. The structural analysis indicates how the underlying interactions of polymer and nanoparticles shrinks the thermal boundary layer, thus assisting heat transfer in laminar flow. The research concludes with an understanding of the capabilities of different nanofluids that can be used for immersive-cooling applications, and a potential to extend the mDPD models to include nanofluids.

Present Contributions

The contributions of this thesis to the scientific community are the following:

- **Establish relationship between the polymer morphology and relaxation**: Olefin co-polymer (OCP) predominantly acts as a thickening agent while dissolved in polyalpha-olefin (PAO-2) because the radius of gyration of the polymer chain does not change with an increase in temperature. This is in contrast to polydodecylmethacrylate (PMA), which expands more with increasing temperature when dissolved in PAO-2. Thus, a branched PMA polymer acts as a viscosity index improver (VII) in PAO-2. The differences in the behaviour are observed in the relaxation times of the two polymer solutions as a function of temperature. The viscoelastic nature of PMA becomes more prominent beyond 353 K when compared to OCP for the same monomer length.

- **Design guidelines for novel heat transfer liquids**: Dilute viscoelastic nanofluids have better heat transfer capabilities emerging from their structural mechanisms of thermal transport. While comparing the nanofluids in the presence of OCP at the same weight fraction dispersed in PAO-2, carbon nanotube-based nanofluids show the highest heat transfer coefficient, followed by 2-dimensional (2D) graphene with the lowest for copper nanospheres. A combination of the high thermal conductivity of CNT, favourable vibrational density of states (DOS) and expansion of the OCP polymer chain during Couette flow make them ideal additives in PAO-2-based solutions for immersive cooling applications.

- **Multiscale MD framework for rheological characterisation of viscoelastic fluids**: Important properties such as deformation response, relaxation modulus and normal stress coefficients cannot be computed at atomistic scale due to computational shortcomings. Building a coarse-grained model requires the conservation of flow characteristics such as transport properties specified by Schmidt numbers, and consistency with observations made at atomistic scale to ensure accuracy of mapping. The mesoscale model developed via mDPD scheme in this work can quantitatively relate the observations made in the reduced units to the real (SI) units. This provides an accessible model to compare experimental results at scales relevant to continuum mechanics along with capturing the chemistries at the atomistic scale, in the case of dilute non-Newtonian polymer solutions. The rheological properties obtained can be fed into computational fluid dynamics (CFD) modelling approaches and complement experimental measurements where non-feasible.

Table of contents

List of figures

List of tables

Nomenclature

Roman Symbols

A_{ij} Conservative force parameter

B Tait equation constant 1

B_{ij} Short-range repulsive force parameter

b Bond distance

C Tait equation constant 2

C_p Specific heat capacity

$C(t)$ End-to-end vector autocorrelation

D Self-diffusion coefficient

$\mathbf{E}_{kinetic}$ Kinetic Energy

E Energy

$\mathbf{F(r)}$ Force vector

F Force

F_{ij}^{C} Conservative force

F_{ij}^{SRP} Segment-repulsive potential

F_{ij}^{D} Dissipative force

F_{ij}^{R} Random force

$G^{'}$ Storage modulus of elasticity

$G^{''}$ Loss modulus of elasticity

$g(r)$ Radial distribution function

$G(t)$ Green-Kubo stress auto-correlation function

$g(t)$ Mean-squared displacement

h^* Hydrodynamic screening parameter

J   Heat flux vector

J_z Component of heat flux vector in z-direction

k_{angle} Angle stiffness energy

k_θ Angle energy constant

k_B Boltzmann constant

k_b Bond energy constant

k_ϕ Dihedral energy constant

k_f FENE bond energy

K_ϕ Improper energy constant

k   Thermal conductivity

m Mass

M Molecular mass

n Term index

N_a Avogadro number

P   Stress Tensor

p Pressure

Q Q factor

q_i Point charge of atom i

q   Heat flux

r   Position vector

R   Universal gas constant

r Position

R Polymer bond distance

r_C	Force cutoff-radius
r_D	Dissipative force cut-off radius
r_d	Density-dependent conservative force cut-off radius
R_e	End-to-end distance
R_g	Radius of gyration
r_H	Hydrodynamic radius
$\mathbf{R}(t)$	End-to-end displacement vector
$\hat{r}$	Unit displacement vector
$\hat{\mathbf{R}}_{mn}$	Unit vector between two bonds m and n
$S_{\text{alignment}}$	Square of ratio of end-to-end distance
Sc	Schmidt number
T	Temperature
t	Time
$V(r)$	Potential function,i.e., force-field
V_{angle}	Angle potential
V_{FENE}	FENE bond potential
V_b	Bonded component of force-field
V_{nb}	Non-bonded component of force-field
V	Volume of the simulation box
v	Velocity
$\mathbf{v}$	Velocity vector
x	x-direction
y	y-direction
z	z-direction

Greek Symbols

θ	Angle

χ_{ij}	Flory-Huggins interaction parameter
δ_{DOS}	Matching degree of density of state
ϕ	Dihedral/Improper angle
ε	van der Waals energy
η	Dynamic viscosity
ω	Angular frequency
γ_{ij}	Dissipative force parameter
κ_T	Isothermal compressibility
∇	Gradient
ν	Kinematic viscosity
ω^C	Conservative force weight parameter
ω^D	Dissipative force weight parameter
ω^d	Short-range repulsive force weight parameter
ω^R	Random force weight parameter
ε_0	Permittivity of vacuum
ψ_1	First normal stress coefficient
ρ	Density, number density (Chapter 2)
Σ	Sum of variables
σ	van der Waals distance
σ_{xy}	Stress tensor component
η_{sp}	Specific viscosity
$\dot{\gamma}$	Shear rate
τ_s	Time constant of shear thinning
τ_Z	Zimm relaxation time
τ_f	Relaxation time of the fluid
τ_{term}	Terminal relaxation time

ζ Gaussian random variable of random force

Superscripts

$*$ Superscript for variable in real units

Subscripts

b Bead

i Subscript index

j Subscript index

k Subscript index

0 Subscript of constant

Other Symbols

$\langle\rangle$ Ensemble average

Acronyms / Abbreviations

AA   All Atomistic

BTMS   Battery Thermal Management System

CGMD   Coarse-Grained Molecular Dynamics

CNT   Carbon nanotube

DFT   Density Functional Theory

DOS   Density of state

DPD   Dissipative Particle Dynamics

EAM   Embedded atom model

eDPD   Energy-conserving Dissipative Particle Dynamics

EV   Electric Vehicle

FENE   Finite Extensible Non-linear Elastic

GPR   Gaussian Process Regression

HFO   Hydrofluoroolefins

K-G   Kremer-Grest

LAMMPS Large scale atomic and molecular modelling parallel simulator

LJ   Lennard-Jones

MD   Molecular Dynamics

mDPD   Many-body Dissipative Particle Dynamics

MWCNT Multi-walled carbon nanotube

NEMD   Non-Equilibrium Molecular Dynamics

OCP   Olefin co-polymer

OPLS   Optimized Potential for Liquid Simulations

PAO   Polyalphaolefin

PBC   Periodic Boundary Conditions

PMA   Polydodecylmethacrylate

PPPM   Particle-particle-particle mesh

SANS   Small-Angle Neutron Scattering

VII   Viscosity Index Improver

VI   Viscosity Index

VM   Viscosity Modifier

Chapter 1

Introduction

1.1 Background

With advances in technology to cater to the needs of the growing global population and significant strides required for slowing down climate change, efforts are made to reduce heat losses [1, 2]. In addition, research on recovering waste heat is ongoing. Apart from this, improving the life of any machine or equipment is at the core of circular economy [3]. When it comes to electrochemical sources of power such as batteries and supercapacitors, they depend thoroughly on thermal management [4]. Several different electronics and electrical devices also require the handling of Joule heating appropriately to improve performance [5]. Given the importance of electrical and electromechanical systems towards a fully decarbonised modern economy, energy-efficiency is of primary importance. This is where research on novel cooling technologies has a crucial role to play.

The mechanisms of heat transfer can be conduction, convection or phase change. The textbook definitions of each of these mechanisms is as follows: (a) Conduction - Transfer of heat via microscopic collisions of atoms, molecules and electrons within a body. (b) Convection - Transfer of heat via the bulk flow of the medium of a fluid. (c) Phase change - Transfer of heat by absorption of the heat to change the physical state of the medium.

Historically, water or aqueous solutions have been at the forefront of cooling. However, limitations of water in the case of electrical equipment such as leakages leading to short-circuiting and shocks, prevent it from wider usage. The other commonly used class of coolants involves oils and petrochemical compounds. For example, transformers do not use water but oil for cooling. Another medium of cooling is air whose thermal conductivity is very low compared to that of liquids. Some inorganic salts in the molten state are used for heat transfer using the principle of phase change. However, they too struggle with toxicity and safety issues. In such an environment, where the future is going to be about rampant electrification, we need

new chemicals and compounds that can be utilised for cooling. The future belongs to designer chemicals made for specific uses. This is where viscoelastic liquids come into the picture.
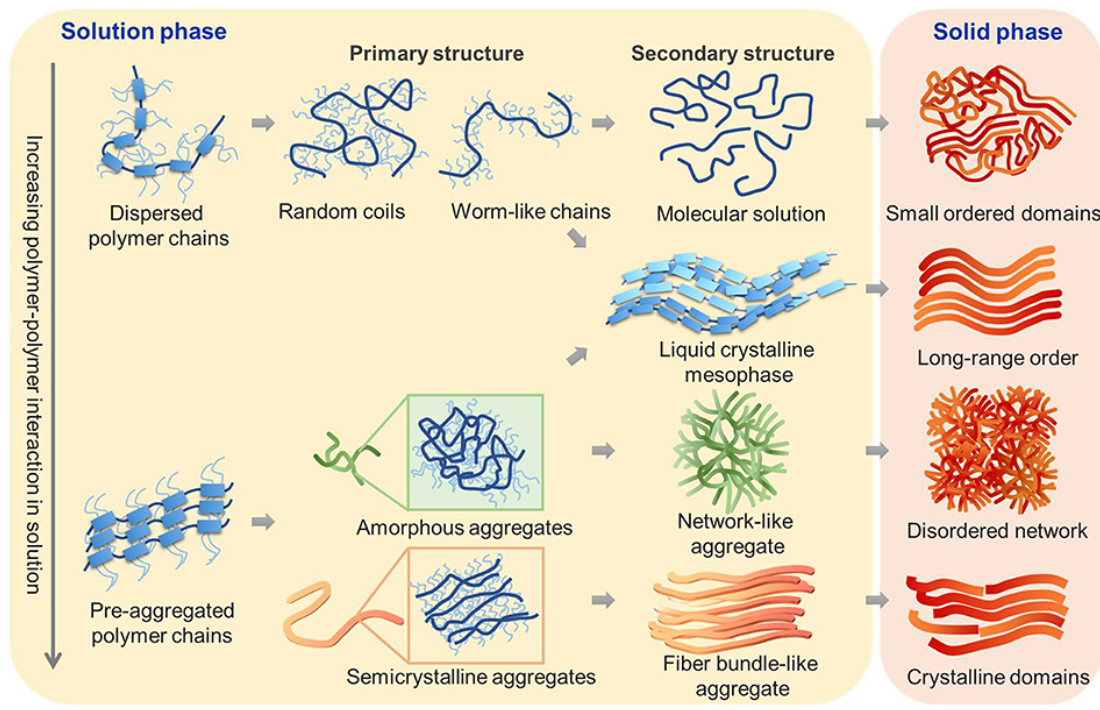
Figure 1.1: The different conformations of polymer in the solution and solid phase that induces novel properties to various materials. Figure reproduced from Reference [11] published under the terms of Creative Commons Attribution 4.0 license (CC BY 4.0).

In our research, we are interested in studying the fluids that are of importance to immersive-cooling of electric vehicle (EV) batteries. The submerged-cooling battery thermal management system (BTMS) aims to achieve a significant increase in heat flux that can be handled at a specific temperature difference. Typically, today's BTMS makes use of indirect cooling by air-, water- or glycol-based coolants [6]. Typical heat production rates for current state-of-the-art batteries are in the range of 10^5 W m^{-3}, while the allowed temperature rise by today's commercial BTMS systems is close to 30 °C [7]. This affects the charging time of the battery, leads to battery degradation, and impacts the lifetime of the battery pack [8]. It consequently acts as a big obstacle in front of the much-needed expansion of EVs in the transport sector. It calls for advanced cooling paradigms such as direct contact immersive cooling of battery packs. There are very few works done in this aspect [9, 10].

From a scientific or flow-physics point of view, immersive cooling will be achieved by manufacturing and testing new viscoelastic nanofluids with efficient thermal and flow performance. The collaborative effect of viscoelasticity and nanoscale heat-transfer phenomena have not been investigated in this context and targeting applications for EVs. Information about their rheological properties that cannot be obtained by experimentation or is limited, can be supplemented for a multi-parametric domain by numerical modelling. Synthesis of heat transfer fluids relies on specific estimations provided by various numerical models, which in turn account for the contribution of viscoelastic stresses and shear-thinning effects.

The addition of long-chain polymers or surfactants in the base oil leads to the formation of flexible micelles that can create complex networks under the presence of shear (see Figure 1.1) [11]. This behaviour is macroscopically perceived as viscoelasticity, which can be tailored to manipulate the fluid rheology in a pre-specified manner. Viscoelastic fluids can also exhibit a shear-thinning nature. Complex fluid rheology can disrupt turbulence cascade and lead to pressure drop reduction in turbulent flows as shown in Figure 1.2 [12, 13]. However, and somewhat counter-intuitively, the dispersed polymers or macromolecules can enhance the vortical motion due to elastic instabilities to increase heat transfer [13]. For such materials, we need to simultaneously understand the rheology and heat transfer characteristics.
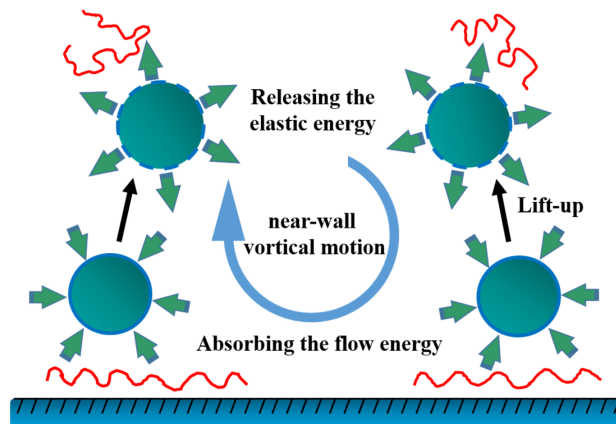
Figure 1.2: Mechanism of drag reduction induced by polymer additives in the solution. Figure reproduced from Reference [13] published under the terms of Creative Commons Attribution 4.0 license (CC BY 4.0).

Oil has reduced thermal conductivity compared to water. The addition of polymer chains is observed to improve the heat transfer capabilities of the resultant polymer solution. The addition of thermally conductive nanoparticles can increase the thermal performance of the formed nanofluids beyond that of respective base liquids as well (see Figure 1.3) [14, 15]. However, the reason for such improved thermal performances is difficult to be gauged using
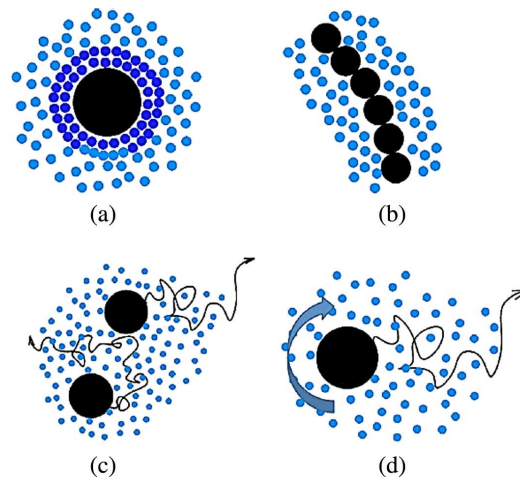
Figure 1.3: Thermal performance enhancement mechanisms in the nanofluids. The nanoparticles are depicted by black spheres and solvent molecules are depicted by blue spheres. The different mechanisms are (a) liquid layering; (b) particle aggregation; (c) particle Brownian motion and (d) Brownian motion induced convection. Figure reproduced from Reference [15] with permission. Copyright 2011, The Americal Society of Mechanical Engineers.

experiments and several macro-scale numerical simulation studies. It requires an understanding of the interactions between the constituent molecules. Therefore, a first-principles methodology at the lower time and length scales is required. There are several important theories and modelling paradigms at these scales (see Figure 1.4). Density functional theory (DFT) is the most fundamental of them. However, the computational cost and incremental gains in understanding the dynamics of the systems we are interested in motivate us to go for the next scale.

Classical molecular dynamics (MD) simulations compute rheological properties of visco-elastic fluids from the theories of statistical thermodynamics. The thermodynamic fluctuations in the simulated system relate to the various macroscopic properties that characterize the material of our interest. These fluctuations arise due to the intrinsic interactions of the atoms composing the material or from an external source. The responses to these stimuli by the system help in the computation of the properties.

1.2 Molecular dynamics

MD is a field of modelling and simulation techniques based on Newtonian mechanics [16]. The methodology involves representing material systems of interest in terms of atoms, molecules or
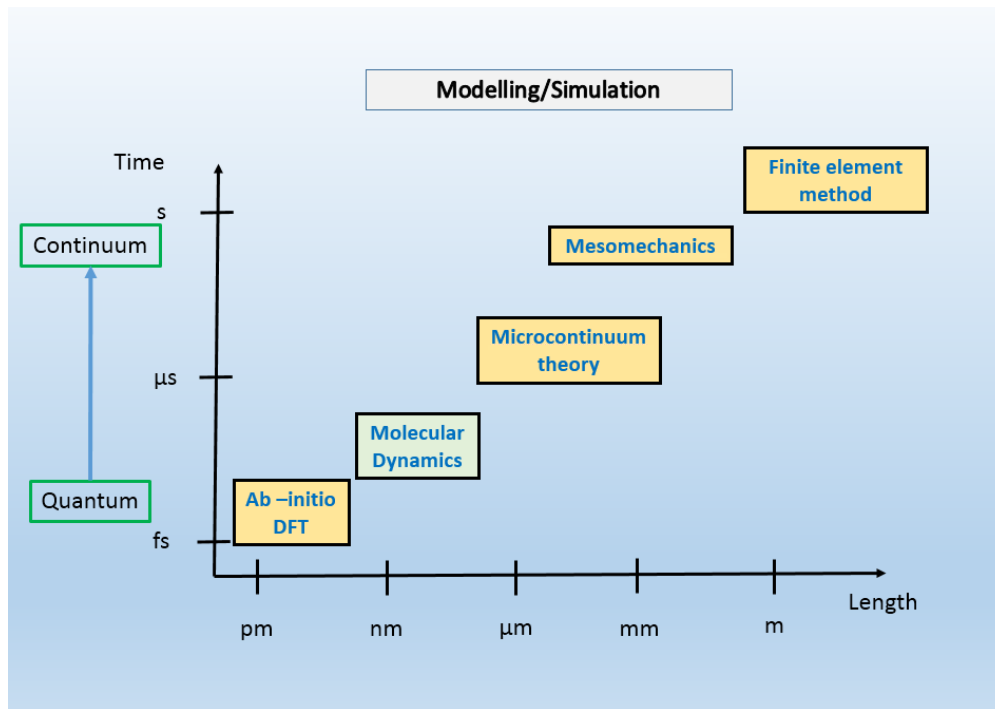
Figure 1.4: The modelling and simulation methodologies at different scales of length and time.

particles (see Figure 1.5). They are simulated to move under the influence of intra-molecular or inter-atomic forces. The forces are defined using potentials, i.e., force-fields that provide information on the nature of the various interactions in the system. The motion thus generated can be characterized by solving the corresponding Newton's equations of motion. The time integration of the equations of motion provides trajectories of the atoms present in the simulated system. The time evolution of these trajectories can be utilised to find the different microscopic and macroscopic properties of interest of the materials.

Classical statistical mechanics provides the theoretical background to relate the time-evolved trajectories of a many-particle system with its various static and transport properties [16]. By computing and averaging the trajectories of the system over a sufficiently long time, we can obtain the property of interest. The assumption is that at sufficiently long times, the system is no longer dependent on the initial conditions. Such systems are said to have achieved *ergodicity*. Time averaging of the properties of an ergodic system is equivalent to the *ensemble* averaging of the properties. This is the basis of equilibrium MD, where properties are computed based on the perturbations within the systems that are in equilibrium at the given physical conditions.

Implementation of MD simulations involves several components and the computation of the required properties has to follow different protocols. The fundamental procedure is to
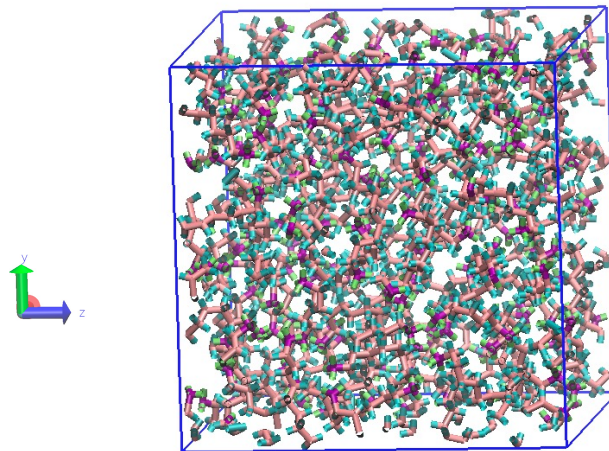
Figure 1.5: The bulk fluid of n-dodecane (used as solvent in lubricants) represented by a group of molecules in a cubic simulation box used to study the fluid in MD.

define a force-field, create the system with an initial configuration, fix the physical conditions at which simulations have to be conducted, time-integrate the equations of motion to update the positions and velocities, and compute the required properties. The following sections describe the key elements of the simulation methodology.

1.2.1 Force-field

The motion of the particles in the system is essentially dependent upon the interaction forces. Therefore, it is important to define the force mathematically to model the interactions. In MD, we use a Lagrangian based on the stationary-action principle. The definition is in the form of a potential of force ($V(r)$) such that:

$$\mathbf{F}(\mathbf{r}) = \frac{dV(r)}{dr} \tag{1.1}$$

where, $\mathbf{F}(\mathbf{r})$ is the force. The expression of potential is also called a force-field. The nature of $V(r)$ is dependent on the design of the system and the extent of interactions to be considered [17, 18]. For example, at the most fundamental scale of MD, i.e., atomistic MD, the systems can be assumed to be composed of single point charges or as beads with polarity depending on the importance of the forces due to electronic charges. The force-field in case of the former is called a non-polarizable force-field (e.g. OPLS-AA, PCFF, AMBER and so on), whereas the force-field used in case of the latter is called a polarizable force-field (e.g. APPLE&P) [19–22].

6

The computational time taken to simulate a system is dependent on the various force-field complexities [23].

Atomistic simulations

The material systems can be represented in the most fundamental form in atomistic MD simulations. Here, the basic entities that interact in the system are atoms. The individual atoms move due to the various inter-atomic and intra-atomic forces. A generic expression of a non-polarizable force-field used in the atomistic simulations is of the form:

$$V(r) = V_{nb}(r) + V_b(r) \tag{1.2}$$

where, V_{nb} is the non-bonded component of force-field and V_b is the bonded component of the force-field. V_{nb} constitutes those forces between atoms due to their distances and individual charges. It accounts for the van der Waals and Coulombic forces. On the other hand, V_b constitutes the forces due to the covalent bonds between the atoms of a molecule. The stretching, bending and twisting of the covalent bonds are accounted by V_b.

Several force-fields for atomistic MD have been developed over time. The differences between the force-fields emerge from the variations in the different terms used to compute V_{nb} and V_b. The parametrization of the force-fields are important to produce the correct description of the system and the results of the properties. Table 1.1 shows the various non-polarizable classical force-fields, and their widespread fields of application.

A different class of force-fields is utilised to model solid-state interactions. The challenges of capturing energetics, stoichiometric non-uniformities, defects and so on require quantum mechanical information in the case of metals and alloys. At the same time, semiconductors having covalent bonds require additional energy terms to accommodate the bonding interactions. For metals and metallic alloys, the embedded-atom method (EAM) [24, 25] is able to predict the cohesion of atoms appropriately. In the EAM model, the potential is formulated such that the atomic energy is computed from the energy required to embed the atom in the local electron density provided by the other atoms of the solid. The basis of this modelling technique is the framework of density functional theory, where the total electronic energy is computed from total electronic density. In the case of metals, the electronic density can be obtained from the linear superposition of the electronic densities of individual atoms.

Materials such as graphene, silicene, germanium and the alloys of carbon group elements are computed using bond-order potentials described by Tersoff [26] and Brenner [27]. They use a formalism where the total energy is based on the sum of bond energies that include

Table 1.1: Widely used classical MD force-fields.

Force-field	Abbreviation	Application
Assisted Model Building and Energy Refinement	AMBER [21]	Simulation of biomolecules.
Consistent Force Field	CFF [20]	Organic compounds and metals.
Chemistry at Harvard Molecular Mechanics	CHARMM [28]	Macromolecules, aqueous solutions.
Consistent Valence Force Field	CVFF [29]	Organic molecules.
Groningen Molecular Simulation	GROMOS [30]	Aqueous solutions, biomolecules and sugars
Optimized Potential for Liquid Simulations	OPLS [19]	General purpose for wide range of molecules.

attractive and repulsive terms. The model requires a systematic solution at least nine parameters depending upon the complexity of the material handled.

Coarse-grained simulations

In coarse-grained MD (CGMD) simulations, the fundamental interacting species are clusters of atoms or molecules combined together as a single bead. The beads act as a low-resolution description of a system with fewer degrees of freedom [31]. In CGMD, the charges of various beads are treated as neutral. The beads can be a cluster of water molecules, monomer units of a polymer chain, biomolecular subunits of proteins and so on. This simplified model increases the computational efficiency of complex systems and processes that evolve slowly over time.

The basis of motion of the beads in CGMD simulations depends on the level of coarse-graining and the principles of interactions [32, 33]. The CGMD simulation force-fields can be described in additive forms similar to the atomistic simulations. The prescribed forces can be based on the distances between beads and the nature of bonds, the description of the hydrodynamics and so on. Typical CGMD simulations are described and properties are reported in reduced units. Hence, proper scaling to physical units is required to validate the observations with the real systems and processes. Several works have been done to scale the reduced units into real units for the various CGMD simulation systems.

1.2.2   Integration algorithms

Once the rules of force computations between the particles in the system are defined by the force-fields, the subsequent component to be discussed is the way to integrate Newton's equations of motion. The numerical integration of the equations of motion is performed using Taylor's series expansion of the position and velocities of particles in the system. Depending upon the level of accuracy and the computational efficiency required for the simulations, there are several algorithms used in MD for numerical integration. Two of the fundamental algorithms predominantly used in MD simulations are discussed in this subsection.

Verlet algorithm

In Verlet algorithm [34], we consider the Taylor expansion of the position of a particle at time t such that

$$r(t+\delta t) = r(t) + \delta t\frac{dr}{dt} + \frac{\delta t^2}{2}\frac{d^2r}{dt^2} + \frac{\delta t^3}{3!}\frac{dr^3}{dt^3} + O(\delta t^4). \tag{1.3}$$

$$\Rightarrow r(t+\delta t) = r(t) + v\delta t + \frac{a}{2}\delta t^2 + \frac{\delta t^3}{3!}\frac{dr^3}{dt^3} + O(\delta t^4). \tag{1.4}$$

According to Newton's second law of mechanics,

$$F(t) = m.a(t) \tag{1.5}$$

Therefore, Equation 1.4 can be rewritten as

$$r(t+\delta t) = r(t) + v\delta t + \frac{F(t)}{2m}\delta t^2 + \frac{\delta t^3}{3!}\frac{dr^3}{dt^3} + O(\delta t^4). \tag{1.6}$$

Similarly,

$$r(t-\delta t) = r(t) - v\delta t + \frac{F(t)}{2m}\delta t^2 - \frac{\delta t^3}{3!}\frac{dr^3}{dt^3} + O(\delta t^4). \tag{1.7}$$

Adding Equation 1.6 and Equation 1.7, and rearranging, we get

$$r(t+\delta t) \approx 2r(t) - r(t-\delta t) + \frac{F(t)}{m}\delta t^2 + O(\delta t^4). \tag{1.8}$$

In Verlet algorithm, we can obtain the velocity of a particle at time t by subtracting Equation 1.7 from Equation 1.6 and rearranging such that

$$v(t) = \frac{r(t+\delta t) - r(t-\delta t)}{2\delta t} + O(\delta t^2). \tag{1.9}$$

Here, the local errors of computing the position and velocity of a particle at time t are of the orders $O(\delta t^4)$ and $O(\delta t^2)$, respectively. In order to improve the accuracy of the velocity calculations, there are other algorithms along similar lines.

Velocity Verlet algorithm

In addition to the computation of the positions as described by Verlet algorithm, the velocities are also explicitly computed in the velocity Verlet algorithm. The Taylor series expansion of velocity is used for this implementation. The scheme is described as below:

- Velocity at half-timestep is computed as

$$v(t + \frac{1}{2}\delta t) = v(t) + a\frac{\delta t}{2}. \tag{1.10}$$

- The positions at full-timestep are computed using Equation 1.10 as

$$r(t + \delta t) = r(t) + v(t)\delta t + a\frac{\delta t^2}{2} \tag{1.11}$$

- The acceleration at full-timestep $a(t + \delta t)$ is subsequently computed using $r(t + \delta t)$ from the force-field by the relationship given in Equation 1.5.

- In the final step, the velocity at full-timestep is computed as

$$v(t + \delta t) = v(t) + (a(t) + a(t + \delta t))\frac{\delta t}{2} \tag{1.12}$$

In the case of the velocity Verlet algorithm, the truncation errors of both positions and velocities are of the order $O(\delta t^3)$. An interesting feature of both the Verlet and velocity Verlet is that the global errors of position and velocity updates are of the order $O(\delta t^2)$.

1.2.3 Ensembles, thermostats and barostats

In an MD simulation, the number of particles (N) and volume of the system (V) are constants by the initial definition of a system. Additionally, the energy (E) is a constant of the positions of the particles. Therefore, MD simulations are in principle defined for a constant NVE ensemble or a microcanonical ensemble. However, the properties of various systems need to be investigated for other physical conditions, such as constant temperature (T), pressure (p), enthalpy (H) or chemical potential (μ). The different ensembles and the corresponding constant physical conditions are provided in Table 1.2 [16].

Table 1.2: Ensembles and constant physical conditions.

Ensemble	Constants
NVE	Number of particles, Volume, Total Energy
NVT	Number of particles, Volume, Temperature
NPT	Number of particles, Pressure, Temperature
NPH	Number of particles, Pressure, Enthalpy
NVK	Number of particles, Volume, Kinetic Energy

In order to maintain the temperatures and pressures at constant values, MD simulations have been improved by the introduction of different thermostat and barostat algorithms. Some of these algorithms are discussed below.

Thermostat

The velocities, as in a microcanonical ensemble, are related to T via the kinetic energy from the Maxwell-Boltzmann distribution of energy

$$\frac{3}{2}k_BT = \frac{1}{2}\Sigma m_i v_i^2. \tag{1.13}$$

Here, k_B is the Boltzmann constant, and m_i is the mass of the ith particle having a velocity v_i for an N-particle system. However, since constant kinetic energy is no guarantee of a constant temperature, several methods have been proposed to maintain the temperature at constant values. The ultimate goal of all thermostats is to add or remove energy from the system. In order to do this, the system is assumed to be surrounded by a hypothetical heat bath. The principles of some of the commonly used thermostats are discussed below:

- **Velocity rescaling**- This is the first and the simplest form of thermostat implemented in MD. In this, the target velocities of particles are achieved using the relationship:

$$v_{i,target} = v_{i,actual}\sqrt{\frac{T_t}{T_a}}. \tag{1.14}$$

where, T_t is the target temperature and T_a is the actual temperature.

- **Berendsen** [35]- Here, the rate of temperature change at every timestep is assumed to be proportional to the difference in temperature between the target and actual temperature. The parameter required for implementing this thermostat is a constant of proportionality called coupling parameter.

- **Langevin** [36]- This thermostat is based on the fluctuation-dissipation theorem. In this, the system is added with hypothetical particles that dampen the motion. The dissipation of energy is compensated by random kicks provided by these particles. The combination of the dampening factor and the stochastic kicks leads to a constant temperature in the system.

- **Andersen** [37]- The system is coupled to a heat bath that provides a totally stochastic form of collisions to randomly selected particles in the system. Analogous to the Berendsen thermostat, here the required parameter is the frequency of these stochastic collisions.

- **Nosé-Hoover** [38, 39]- This is the most widely used thermostat in MD. The thermostat uses an extended Lagrangian form of equations with added fictitious coordinates and velocities of the particles in the system. These fictitious positions and velocities are related to the actual positions and velocities of the particles. The fictitious particles added are parametrized based on their chain size and effective mass.

Barostat

The stress tensor of an MD system is computed by solving the Clausius virial equation of the form

$$\mathbf{P} = \frac{2}{V}(\mathbf{E}_{kinetic} - \frac{1}{2}\Sigma \mathbf{r}_{ij} \cdot \mathbf{F}_{ij}) \tag{1.15}$$

where, V is the volume of the simulation box, $\mathbf{E}_{kinetic}$ is the kinetic energy and $\frac{1}{2}\Sigma \mathbf{r}_{ij} \cdot \mathbf{F}_{ij}$ is the inner virial tensor. The target stress tensor in the case of all the barostats is achieved by modifying the inner virial. The consequent pressure is obtained from the trace of the stress tensor. Some of the commonly used barostats are discussed below:

- **Berendsen** [35]- The implementation is exactly similar to the corresponding thermostat. The rate of pressure change in subsequent timesteps is assumed to be proportional to the difference in target pressure and actual pressure.

- **Andersen** [37]- Here, an extended Lagrangian is used, which in principle is similar to the implementation of the Nosé-Hoover thermostat. The additional fictitious particles are added such that they act as a piston compressing or relaxing the original system of particles. This barostat is used for controlling the isotropic pressure of the system.

- **Parinello-Rahman** [40]- This barostat is an improved version of the Andersen barostat extended to include anisotropic coupling. Here, the heat bath not only modifies the volume of the system corresponding to the stresses, but also allows it to change the shape. The advantage is that, in many cases, the grain boundaries remain unaffected ensuring conservation of the intrinsic properties of the systems. This barostat is used in conjunction with Nosé-Hoover thermostat to maintain constant p and T.

1.2.4   Non-equilibrium molecular dynamics (NEMD)

Molecular dynamics simulations were theorised and developed to simulate systems under equilibrium conditions. However, additional developments were made to simulate systems that are not at equilibrium. Under these non-equilibrium conditions, the system energies achieve equipartition faster than the particle vibrations themselves. Non-equilibrium molecular dynamics (NEMD) is a powerful tool to simulate diffusive flows, viscous flows, plasticisation of materials and several such processes [41, 42].

NEMD uses time-reversible equations of motion as in the case of equilibrium MD. At the same time, the microscopic basis for the macroscopic Second Law of Thermodynamics (i.e., irreversible processes) is constructed such that internal variables can be used to control the temperature and pressure of the system. In other words, the need for external heat baths or pistons to control temperature or pressure is overcome by directly modifying the equations of motion. This helps in localised control of the system conditions in the ensemble. A class of methodologies has been developed using this principle under the umbrella of NEMD, looking into various processes [43–45].

1.2.5   Algorithms and software

The complex systems being handled in several MD simulations require several additional algorithms to ensure efficiency, effectiveness and feasibility. Even though the array of algorithms that are used in MD is long, few of them relevant to our piece of work are described in this section.

Periodicity

Simulation of a macroscopic system ideally requires an infinite number of atoms or particles. However, the creation and simulation of such large systems are impractical in the MD simulation regime. Therefore, a technique to mimic the infinitely large system is implemented with the use of periodic boundary conditions (PBC). Here, a simulation box consisting of the original atoms is assumed to be surrounded by an infinite number of boxes of the same dimensions on the required sides. When an atom moves out of the original box, its image in all the boxes is also expected to move in a similar manner. This periodicity conserves the number of atoms in the box throughout the simulation. PBC implementation uses minimum image convention to determine the distances between the atoms and subsequent force calculations [46]. Here, a simulation box is surrounded by replicas of the same creating an infinitely long superlattice of simulation boxes. The distances are computed for the nearest replicas of the atoms. In other words, the forces are calculated between the nearest periodic images of the two atoms in a simulation box.

Interactions and cut-off

The most time-consuming process of an MD simulation is the computation of forces. Among the force-field terms, the computation of pairwise van der Waals and Coulombic forces is the costliest. In periodic systems, the convergence of these non-bonded forces with distance is slow. Therefore, it is important to ensure that these force calculations are done in a fashion such that there is a balance between accuracy and efficiency. The standard process is to select a distance cut-off beyond which the computation of pairwise interactions does not significantly change the magnitude of the forces and energies. In several systems, the computation of these short-range interactions is sufficient for convergence. So, a hard cut-off is provided in the computation of the non-bonded forces.

The error due to the truncation of the slowly decaying Coulombic forces is significant. The computation of long-range interactions is essential in such scenarios. The Coulombic forces in the case of atomistic MD involve the interactions between the partial charges of the various atoms. In such a case, an algorithm is proposed to compute the interactions faster without losing accuracy. It involves mapping the Coulombic force function to an inverse Fourier plane as a sum of two convergent functions. This ensures a rapid convergence and avoids the problem of truncation errors. A class of such transformations belongs to the family of Ewald summations. All of them depend on the Fast Fourier Transform of a three-dimensional grid making it suitable to be used alongside MD simulations [47, 48].

Neighbour-lists

In addition to the distance cut-offs of the non-bonded forces as described above, a bookkeeping technique is essential to optimize the CPU-time requirement. The calculation of the pairwise forces and energies in the simplest form requires a nested loop with three levels. The computational effort required in this case is of the second-order with respect to the size of the system. Therefore, a technique that involves reducing the frequency of computations of distances and nearest images, is utilised. This is the principle behind the creation of Verlet neighbour-lists of a particle in the periodic system.

The simplest scheme of Verlet neighbour-list implementation is as follows:

- A skin distance, r_{skin} is selected in addition to the cut-off distance $r_{cut-off}$ for the i-th particle such that its neighbouring distance (Verlet distance) is

$$r_n = r_{cut-off} + r_{skin} \tag{1.16}$$

- We generate a list of j particles within r_n. The forces and energies are computed only for these j particles.

- The frequency of the neighbour-list updates are fixed based on a criterion.

In the long term, the net computational effort requirement becomes first-order. The Verlet neighbour-list implementation effects on the system evolution and properties have been studied along with optimum values for the skin distance and the optimal criterion for the update frequency [49].

Modern-day molecular dynamics simulation studies are done using software packages in which the MD simulation codes and several advanced algorithms, such as the ones discussed above are implemented. Some of the software is proprietary and commercial. For example, ADF, CHARMM, CHEMKIN, BIOVIA Discovery Studio, etc. A vast majority of others are open-source. A few examples are, GROMACS, LAMMPS, MDynaMix, PLOP, NAMD, NWChem etc. In our study, we use the open-source code large-scale atomic and molecular modelling parallel simulator (LAMMPS) to conduct MD simulations. It has an array of implementation algorithms suitable for the systems handled.

Large-scale atomic and molecular modelling parallel simulator (LAMMPS)

LAMMPS is a software tool developed by Plimpton [50] based on C++ library. The codes have been implemented as different modules that can be compiled independently. The primary advantage of LAMMPS is in the parallelization capabilities. The simulations can be done on a

vast number of CPU cores. Here, the back-end algorithms ensure division of labour among the individual cores to extract their maximum efficiency.

A typical LAMMPS simulation requires two sets of input. They are explained below in brief:

- **Data**- Depending upon the nature of the MD simulation, the datafiles need to have certain basic information. For an atomistic MD simulation, the following information is required in the datafiles: the size of the simulation system, number and types of the atoms, force-field parameters, partial charges of the atoms, positions of atoms, and information of the bonds between atoms of a molecule.

- **Simulation script**- The file includes the list of actions the algorithm has to take in sequence. For the datafile described above in the case of an atomistic MD simulation, the script should contain the following commands at the very least: the units of computation, the dimensions, the description of the force-field, the name of the datafile and neighbour-list parameters.

The instructions in the simulation script file are read by the LAMMPS execution shell and carried out. The commands in the script are provided depending on the nature of the system being handled and the results of the simulations expected. A typical equilibrium MD simulation progresses in the following fashion in LAMMPS:

- **Minimization**- This is the energy minimization step in MD. Here, the atoms or particles are perturbed from their initial positions and the potential energy of the system is brought to a local minimum. This is to ensure the removal of any unphysical conditions present in the system created for simulation. LAMMPS provides different minimization algorithms: conjugate gradient, steepest descent, Hessian-free truncated Newton algorithm, quickmin, spin, and fire.

- **Equilibration**- In this step, the energy-minimized systems are gradually brought to the physical conditions where we have to compute the properties. We apply various thermostats and barostats to direct the system toward the targeted conditions.

- **Production**- Once the system is equilibrated and brought to the right physical conditions, we provide commands to capture the trajectories of the system. Commands to compute various properties can be provided at this stage of the simulation.

Computation of properties with minimal statistical deviations requires not only long simulation times but also independent runs of MD simulations. Additionally, multiple simulations of the

same system ensure the reproduction capabilities of the force-field and validate the simulation protocol.

LAMMPS has a vast array of commands useful to carry out NEMD simulations. It is possible to find transport properties of systems with methodologies described by Daivis and Evans [51], Müller-Plathe [52] using the software package. The protocols required to do NEMD simulations are well-explained in LAMMPS.

1.3 Critical literature review

The section details the studies conducted in the area of liquids consisting of macromolecules that are used for commercial applications. Literature available on heat-transfer applications is also discussed. The major works of molecular dynamics studies in the area are noted and the existing research gaps and the scope for the current research are summarised.

1.3.1 Soft condensed matter fluids

The substances that cannot be entirely classified into solids or liquids are termed as soft condensed matter. They have properties that can be categorised as both liquid-like and solid-like. These materials (called fluids hereafter) have tremendous scope for commercial applications. They are used in lubrication, for excavation of oil and minerals, as construction materials, as biological substrates and so on [53, 54]. In this work, we are mostly interested in those fluids used at the industrial scale as a medium at the interface of solids. These are synthetic fluids based on several nano or macromolecules present in a flowing medium [55].

Polymer additives

Lubricants are one of the largest subclasses of such fluids. Smeeth et al. [56] studied the film-forming capabilities of a range of polymer solutions between solid surfaces that vary in thickness/viscosity based on the rolling speed. Polymers as viscosity modifiers (VM) in lubricants are detailed by Ver Strate and Struglinski [57]. They can either thicken the solvent medium or act as a viscosity index improver (VII). A VII helps the solution achieve better viscosity at higher temperatures than at lower temperatures. Polymers in the olefin and methacrylate families are known to be useful as VM [58]. Further improvements in lubrication have been achieved by the addition of nanoparticles.

The fluids that are used as lubricants are also considered for heat transfer applications given the anomalously enhanced characteristics they have [59]. The typical coolants used in the metal forming industry are polymer dispersed aqueous solutions [60]. The ability of the polymer to

separate from water molecules and adsorb on the hot solid surface forming a layer helps in controlling the rate of cooling [61, 62]. Thermal conductivity of non-Newtonian polymer fluids has been shown to be shear-dependent [63–65]. The energy and momentum equations have to be solved simultaneously [64].

The compatibility of polymer fluids based on hydrofluoroolefins (HFO) is being considered for use as refrigerants [66]. The advantage of using these compounds is that they can be directly applied in the traditional Organic Rankine Cycle [67, 68]. The chemical and thermal stability of HFO compounds in case of refrigeration applications are reported by Juhasz and Simoni [69], and Invernizzi et al. [70]. The HFOs are found to be less stable against metals such as copper leading to corrosion and fluid decomposition [71].

Nanofluids

Nanoparticle additives are classified into seven based on the basic chemical elements. They are metal-based, metal oxide-based, carbon-based, sulphur-based, rare-earth-based, composites, and others [72]. Graphene-based nanolubricants have been studied to understand their rheological properties, heat transfer capabilities and chemical stability [73]. However, enhancement of their properties still has plenty of scope. Lubricants using nano-sized polymer particles show good friction reduction properties [74]. Nanoparticle-based lubricants have four different lubrication mechanisms [75], viz. nanoparticle rolling [76], film formation due to reactions on the surface [77], mending effect due to minimal size [78], and polishing [79].

The nanoparticles that have high thermal conductivity when suspended in oils show higher thermal conductivity than predicted by various theoretical models. The concept of nanofluids was coined by Choi and Eastman [80] and were first proposed as a way to enhance the characteristics of conventional heat transfer fluids. There is an imminent focus on preparing stable nanofluids based on oil solvents as reported in the review by Asadi et al [81]. The preparation methodologies include the application of one or two steps involving direct fabrication, sol-gel technique, chemical precipitation, mechanical stirring, direct condensation, functionalization acid process and electrical explosion of wire (single-step process). Under no-flow conditions, the suspension stability of these nanofluids can last anywhere between 2 hours to 2 weeks. Rheological studies listed in the review by Sharma et al. [82] show that the nanofluids that are reported in experiments generally demonstrate Newtonian behaviour. However, the rheological behaviour of oil-based nanofluids is an interplay between the chemistry/morphology of the nanoparticles, size of the nanoparticles, concentration, stabilising agent, temperature as well as shear rates.

While investigating the current applications of nanofluids, their uses are reported in high voltage applications to replace transformer oils or vegetable oils [83]. Mineral oils are used as

the base oils in which nanoparticles based on silver, copper, silicon oxide and titanium oxide are dispersed for these applications [83, 84]. Studies at high temperatures and high pressure are done to understand the rheology of SiO_2 nanoparticles in paraffinic mineral oil [85]. These nanofluids show an increase in viscosity as pressure increases, whereas the viscosity decreases with an increase in temperature. Refrigerants based on novel soft-matter fluids are of interest in recent times as they can be ozone-safe [86]. The fundamental thermophysical properties relevant for such fluids are yet again viscosity and thermal conductivity. A study on Al_2O_3/R141b nanofluid refrigerant shows that viscosity decreases with temperature and increases with the volume fraction of the nanoparticles [87, 88]. On the other hand, thermal conductivity increases uniformly with volume concentration at all the temperatures experimented on. Therefore, there is an optimum concentration of the nanoparticles to ensure minimal pressure drop and pumping power without losing out on the advantage of good heat transfer performance [88].

The thermal conductivity of silver/deionised water nanofluids increases with temperature and nanoparticle concentration [89]. Studies indicate the deficiency of Fourier's Law in computing the thermal conductivity of nanoparticles. It is shown that the thermal conduction happens ballistically in the case of nanotubes [90, 91]. In the following section, we will see how flow affects the thermophysical properties of the fluids. Studies have shown the effect of temperature on the viscosity of nanofluids [92]. The viscosity decreases with temperature as the interactions between nanoparticles and base fluid become weaker [93]. As the fraction of nanoparticles increases, the dynamic viscosity increases uniformly over all temperatures [94]. However, the drop in dynamic viscosity with temperature increases at a higher volume fraction of nanoparticles.

Secondary flow

Secondary flows are an important criterion when considering heat transfer fluids. The flow can influence and generate several behavioural changes in polymer solutions [95]. The shear flow leads to migration in non-homogeneous flows or leads to turbulence. It can even lead to gelation depending upon the polymer concentration. When the viscoelastic properties of constituent molecules are different, demixing can occur. Karathanassis et al. [96] used Particle Image Velocimetry to determine the secondary flow patterns and pressure loss reduction of base oils and polymer solutions used in hydraulic circuits. Onuki [97] has listed the processes where shear effects are important: a) flows where fluctuations are slow; b) flows where phase separation occurs; c) flows involving viscoelastic binary fluids with varying composition; d) flows involving colloidal suspensions; e) flows involving fluids with complex internal structure and long-range order. Recent works have reported the impact of viscoelastic micelle formation of polymers on cavitation and turbulence suppression [98, 99].

Polymer relaxation

Dilute polymer solutions are of commercial interest in micro-scale applications, given their lower viscosities compared to concentrated solutions, subsequently helping in overcoming pumping problems [100]. Conventional experimental techniques based on microfluidic shear have been found to be ineffective in measuring the relaxation times of the polymer solution in low-viscous solvents [101]. This is because of the limits of instrumentation that cannot measure relaxation times in the order of milliseconds [102, 103]. New methodologies have been proposed recently. Zilz et al. [104] have shown the use of a serpentine micro-rheometer to measure the relaxation times of polyethylene oxide solutions. Further, Del Guidice et al. [103] have demonstrated a novel μ-rheometer to measure the relaxation times of viscoelastic liquids using the particle migration in microchannel flows.

In contrast, relaxation time measurements using extensional flow have been suggested for dilute non-Newtonian solutions [105]. Cross-slot extensional flow devices have been proposed by Haward [106] to measure relaxation times via this technique. Capillary-flow-based techniques are found to measure relaxation times as low as 240 μs [107]. Capillary thinning methods are found to measure relaxation times as low as 100 μs [108]. At the same time, researchers have used high-speed imaging to detect relaxation times as fast as 80 μs in case of filament stretching of polystyrene solution [109]. Additional faster relaxation process measurements require the assistance of numerical modelling. This is where MD simulation can help in computing the relaxation times.

1.3.2   Molecular dynamics simulation

Simulation of polymer fluids

There are several advantages of MD while studying the rheological properties of complex fluids. As described by Trevelyan [110], multiple phases or molecular species are treated naturally with MD methods. The changes in interaction potential describing a multi-phase flow do not alter the equations of motion, unlike in continuum mechanics. Microstructure changes in complex fluids occur naturally. Discontinuities in flow are also taken care of naturally in the MD regime.

In recent times, the classical tube theory explaining the behaviour of entangled polymers has been subjected to scrutiny and rejection. Advanced experimental techniques such as small-angle neutron scattering (SANS) have shown that the retraction of entangled polymers after a large uniaxial deformation is completely different from the tube theory. However, the basic bead-spring model used in MD (known as the Kremer-Grest model) has been found to give

results matching that of SANS experiments. This shows the power and flexibility of MD as a tool [111].

Various models have been utilized to describe polymer interactions in different length scales and time scales of simulations. There are two fundamental models still used predominantly: a) Rouse model- that can describe the dynamics of shorter-chain polymers below entanglement length. b) Reptation model- that can describe the dynamics of larger-chain polymers above entanglement length.

Further work by Zimm [112] on the Rouse model was required to establish the critical relationship between the self-diffusion coefficient, D and number of monomers (N) as $D \propto 1/N^v$ where v is the Flory exponent. Still, the Rouse model does not take into consideration the excluded volume (a property that defines if a polymer expands or collapses due to monomer interactions). This makes its application limited to short-chain polymers. The reptation model takes into consideration the excluded volume. The relationship between D with respect to N is seen as $D \propto 1/N^3$ here. This is close to the experimentally observed relationship, viz., $D \propto 1/N^{3.4}$.

The Kremer-Grest (K-G) model that involves the assumption of monomers as beads connected with each other using springs is widely utilized in MD to study the dynamics of polymers [32]. The springs are modelled on the basis of finite extensible non-linear elastic (FENE) potential. This model is a type of united-atom model where an entire monomer is considered as a single spherical bead. However, further fine-grained MD is also done based on the availability of computational power and properties that have to be analysed. There are works where a -CH2- fragment is treated as a single bead (united-atom) instead of the entire monomer in case of the polyalkenes [113]. There are recent works where atomistic simulations are also being done, where each atom is treated as a bead [114]. In the latter case, even Coulombic interactions are treated separately in the force-field equation by giving each atom a partial charge [115].

In MD, all these models are able to come close to the experimental predictions as well as the behaviour formulated by the Rouse and reptation models. Depending upon the various properties to be evaluated and the systems that are to be handled, the nature of the independent monomers and solvents can be decided. MD simulations of the polymeric fluids are carried out using equilibrium MD, where the stimulus is equilibrium thermal fluctuations, and using non-equilibrium MD (NEMD) [116, 117], where the stimulus is provided as external stress, field or heat flux.

Polymer fluids are generally found as a solution in a solvent, or as a melt. In the case of the solution, polymers can be further treated as a dilute material if the individual polymeric chains do not interact with each other [101]. In dilute polymers, the solvents relax rapidly and hence

are considered as a stochastic background. In MD, works have been done with implicit and explicit models for solvents. Even though implicit-solvent models have been shown to work well in the evaluation of various structural and dynamic properties of the polymers qualitatively, they fail to predict the collapse of polymer chains. Hence, explicit models are suitable for such evaluations [118]. Also, if excluded volumes and hydrodynamic interactions are not accommodated properly in the common polymer models with implicit solvents, they may even show completely different trends for different shear rates than what is expected [119]. Performing simulations of single chains under shear, Datta et al. [120] identify the properties that are independent and dependent on the concentration. Based on the flexibility of the chains, it was predicted that collective disentanglements are responsible for shear-thinning.

A fundamental challenge in K-G MD is that the simulations are run using reduced units. Even though this makes the simulation process rapid, it is difficult to compare the results with actual experimental results. New works are emerging to map the results of this K-G MD to the properties of polymers in actual units [121, 122]. However, similar works in the area of polymer solutions are yet to be explored more.

Dissipative particle dynamics (DPD), another CGMD methodology based on the fluctuation-dissipation theorem has proven to model the polymer system dynamics. Espanol and Warren [33] systematically derived the relationship between the different parameters required to model the systems using the DPD algorithm. The conservative force is related to the isothermal compressibility. Flory-Huggins interaction parameter relates the repulsion parameters of two dissimilar beads [123]. DPD simulations have the same problem as K-G MD simulation studies related to the mapping of the results back to physical units. Recent works are providing insights into rigorous ways to scale the properties [124, 125]. Thus, a potential to describe a systematic modelling regime exists in this field.

Simulation of nanofluids

Atomistic MD simulations of nanoparticles in liquid solvents have been utilised to estimate the effective thermal conductivity of nanofluids in a comparative manner against the base solvents [126]. Compared to polymer solutions, more work has been done on the MD study of heat transfer capabilities of the nanofluids [127, 128]. Heat flux equation modifications are proposed to improve the results of heat transfer by [126]. Lu and Fan [129] have shown that the thermal conductivity of water and ethylene glycol can be increased by the addition of Al_2O_3 nanoparticles. The thermal conductivity is shown to increase with the volume fraction of the nanoparticles. As things stand, most of the works reported are for Argon-based model fluids and aqueous solutions [130, 131]. Works in the area of atomistic simulation of nanofluids based on mineral oil or hydrocarbon solvents are limited.

The coarse-grained MD studies dealing with nanoparticles dispersed in hydrocarbon solvents are mostly reported for application in the oil industry for the recovery of oil [132]. Polymer-grafted nanoparticles are studied in this case and the viscoelastic nature of these materials is characterised by estimating the storage and loss moduli, viscosity and shear rate response. However, there is plenty of scope in learning the heat transfer capabilities of the nanofluids using MD simulations.

1.3.3   State of the art

The research in this thesis attempts to identify the requirement of MD in addressing the limitations of experimental and numerical research related to dilute non-Newtonian liquids. The experimental measurement of normal stress differences is carried out using rotational rheometers, Capillary Breakup Extensional Rheometers (CaBER) or cone-partitioned plate (CPP) rheometers (that report an overestimation of the first normal stress difference) [133]. However, such measurements become inaccurate or impossible in low-viscosity dilute mixtures. The measurement of the relaxation times of dilute polymer solutions (of the order μs) in shear flow is challenging due to the detection limits of conventional instrumentation related to inertial effects and currently depends on microfluidics-based approaches [101]. However, as reported by Zilz et al. [102], the inconsistency of results obtained from the latter measurements is a cause of concern. A first-principles-based approach, as in the case of MD will assist in computing these properties. Concurrently, the MD studies of oil-based nanofluids are almost absent from the literature, mainly due to the limited transferability of force-field parameters that are suitable to be used in case of mixtures involving solid molecules and long-chain hydrocarbons [134]. Thus, a systematic analysis of all the available force-fields and corresponding parameters is essential for the prediction of rheological, transport and thermal properties. Moreover, the scientific research related to the thermal transport mechanisms of nanofluids is currently focussed on explaining them based on phonon density of states (DOS) [135]. At the same time, MD studies on heat transfer in polymer-additised nanofluids will be a novel contribution to the scientific community.

1.4   Research plan

The research is focussed on a bottom-up approach to characterise the different candidates of non-Newtonian liquids that can be utilised in heat transfer applications. The chemical compounds are simulated at the atomistic scale using MD to obtain the important rheological and transport properties. The properties found at this scale act both as a benchmark and as

parameters for the mesoscale many-body dissipative particle dynamics (mDPD). The mesoscale studies are aimed to act as a bridge between the macroscale experimental measurements and the atomistic scale behaviour. We use equilibrium MD and NEMD methodologies wherever appropriate to compute the different properties. The liquids that are simulated in this work are dilute polymer solutions and nanofluids based on organic solvents. We use LAMMPS as the MD simulation tool in this research. We use the Hyperion HPC cluster available at City, University of London and Fritz HPC cluster available at FAU-Erlangen to carry out the simulations for the work. A schematic of the research plan is shown in Figure 1.6.
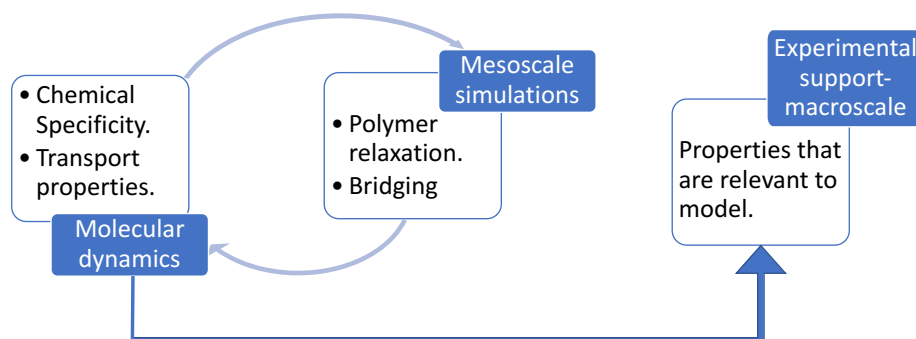
Figure 1.6: Schematic of the objectives of the research.

The atomistic scale simulations involve the compounds modelled with the constituent atoms as the fundamental interacting particles. The force-field to be used for different liquid systems is determined based on the literature survey. For example, the L-OPLS-AA force field is commonly used in case of polymer solutions given their computed thermodynamic and rheological properties are closer to experimental values. Similarly, nanoparticle fluid simulation requires compatible force-fields such as Lennard-Jones (LJ) potentials, embedded atom model (EAM) or Tersoff potential depending upon the material simulated. The open-source tools such as Moltemplate and PACKMOL are used to generate the input files required for LAMMPS simulations. We use certain in-house codes to bridge these tools. A typical schematic for the workflow used for the simulation of a polymer solution in the preliminary studies are shown in Figure 1.7.

The coarse-grained class of simulations involves a cluster of atoms grouped together as spheres, that act as the fundamental interaction particles in the simulations. The purpose of these simulations is to study the behaviour of liquids are higher length- and timescales. Certain non-Newtonian fluid behaviours can only be observed at these scales. The simulations

Solvent (S) – A long chain hydrocarbon

❖ **Free/Open-source software**

Decide on the type of the solvent (S) and polymer (P), nanoparticle (N) and concentration (c) in the solution.

Generate P using the building blocks in **MOLTEMPLATE**.

Use **OVITO** to generate the **LAMMPS** data files of N.

Generate *S* using the alkane building blocks provided by **MOLTEMPLATE.**

Generate **LAMMPS** data files of *S, P and N* using different via **MOLTEMPLATE** with concn - *c*.

Combine S, P and N simulation boxes using *read_data append* command in **LAMMPS** to create the final solution to be simulated.

Figure 1.7: Schematic of the workflow of the atomistic MD simulations.

Decide on the concentration (c) and length (L) of polymer in the solution

Python code *generatepdb.py* to develop pdb of a freely jointed polymer of *L* units

Use **PACKMOL** to generate a polymer solution simulation box of concentration *c* in pdb format

Solvents are point particles/ beads

❖ *In-house developed Python codes*
❖ **Free/Open-source software**

Load the pdb in **VMD** and generate a template of **LAMMPS** data file

Create the final **LAMMPS** data file using *bonds.py*, and *angles.py* (optional)

Model the solution using the appropriate forcefield styles in **LAMMPS** input script

Figure 1.8: Schematic of the workflow of the mDPD simulations of a polymer solution.

in the mesoscale studies are conducted in reduced units that are dimensionless. Therefore, appropriate scaling has to be done to physical units. This is a challenging process and needs to be done carefully to prevent loss of information while translating. A typical schematic for a coarse-grained molecular modelling of the polymer solutions is shown in Figure 1.8.

1.5   Thesis outline

The thesis has three chapters dedicated to the research on non-Newtonian fluids, majorly focussing on their rheological properties important for heat transfer applications. The candidates of interest in this case include various viscoelastic polymer liquids, nanofluids and viscoelastic nanoparticle suspensions.

Chapter 2 investigates the use of a commercially relevant polyalphaolefin oil (PAO-2) and a corresponding polymer solution for heat transfer applications. The various rheological, structural and transport properties are computed and the systems are compared based on these properties. The chapter concludes with the findings of how structural properties lead to the shear thinning nature of the polymer solution. Subsequently, it manages to showcase how the thermal conductivity increases with the addition of a polymer chain. However, the chapter also points out the limitations of atomistic simulation to compute the relaxation times of longer polymer chains. This calls for the development of a mesoscale modelling routine.

Chapter 3 explores the development of a systematic mesoscale modelling scheme to obtain important rheological properties of the polymer solutions. The research uses many-body dissipative particle dynamics (mDPD) simulations to reproduce the transport properties and viscoelasticity of the dilute polymer solutions. The polymer solutions under focus are olefin co-polymer (OCP) and polydodecylmethacrylate (PMA) in PAO-2 oil. The modelling routine establishes a method to bridge the atomistic simulations and coarse-grained MDPD models via Schmidt number matching. The framework captures the structural differences in OCP and PMA solutions at mesoscales, as observed in atomistic scales. The model provides a mechanism to derive the properties in SI units in order to compare them with experiments. The relaxation times as a function of temperature and shear rates are computed. Finally, a structural understanding of the viscoelasticity of the added polymer chains is provided.

Chapter 4 reports a comprehensive study on the heat transfer capabilities of the nanofluids based on the liquids of first chapter. Three different nanoparticle chemistries, viz. copper nanospheres, 2-dimensional (2D) graphene and a single-walled carbon nanotube (CNT) are dispersed in PAO-2 oil and OCP-based polymer solutions. The differences in the thermal conductivities and the mechanism of heat transfer are studied. The underlying physics for the heat conduction is explored. Consequently, the impact of the presence on nanoparticles

along with a polymer chain on heat transfer coefficients during Couette flow is reported. The chapter concludes by recommending the use of viscoelastic nanofluids for immersive-cooling applications.

Chapter 5 recounts the the major findings providing overall conclusion to the PhD research. As for any time-bound scientific study, the work here also leaves scope for future explorations. The important future research that can be carried out using the information from the present investigations is indicated in the chapter.

Chapter 6 lists all the publications that have resulted from the current research. The report has cited close to 360 important references conforming to the due diligence required for the thesis. Finally, two appendices A and B are supplemented to complete the information necessary for chapters 2 and 3.

Chapter 2

Dilute viscoelastic polymer solution

[1]

The suitability of industrially significant synthetic oils with dispersed polymeric chains that can be used as dielectric coolants with enhanced heat transfer properties in single-phase immersion cooling for electric vehicle components is evaluated via molecular dynamics simulations (MD). The fluids investigated are a synthetic solvent polyalphaolefin (PAO-2) and a solution based on PAO-2 with a single olefin co-polymer (OCP) chain dissolved. The simulation model accurately predicts the experimental thermodynamic properties of PAO-2. The effect of the polymer chain on the structural behaviour of the solution and its relation with the rheological properties is predicted and analysed at various temperatures in the range of 293 K - 373 K. It is found that polymer solution shows an average viscosity enhancement of 9.2 % and thermal conductivity enhancement of 2 % within the temperature range. These properties eventually influence the Weissenberg and Nusselt numbers that impact the heat transfer. Analysis of the hydrodynamic radius of PAO-2 molecules shows that OCP chemistry acts as a thickening agent in the solution. Addition of the polymer chain is also shown to accelerate the shear thinning process due to increase in storage and loss moduli. The terminal relaxation time of OCP decreases with temperature and shear rate. The work conclusively establishes the impact of molecular interactions of the weakly viscoelastic liquids on their macroscopic behaviour. The viscoelastic nature of the examined polymer solution can lead to vortex roll-up in constricted flows inducing heat transfer enhancement. This in turn supports its use in immersion cooling applications which is shown for the first time.

---

[1]A significant portion of this chapter is published as: B. Ravikumar, I. K. Karathanassis, T. Smith, M. Gavaises, "Dilute viscoelastic polymer solutions for dielectric heat transfer applications: A molecular dynamics study", *International Journal of Thermofluids*, 18:100333, 2023 under the terms of Creative Commons Attribution 4.0 license (CC BY 4.0). The author of this dissertation has contributed to the methodology, validation, data curation, formal analysis, investigation, writing and visualisation of the article.

2.1   Introduction

Effective thermal management of several electrical and electronic devices such as transformers, integrated circuits, electric motors and battery packs, among others constitutes a crucial aspect designating their performance [136, 137]. Novel heat convection cooling concepts are actively pursued employing heat transfer liquids with properties tailored to the application of interest rather than relying on conventional coolants such as water or air [138–141]. Specifically referring to vehicle electrification technologies, the incorporation of suitable battery thermal management systems (BTMS) can allow faster battery charge/discharge rates, lead to smooth performance characteristics of the electric motor and high speed gear-box, and facilitate in increasing the battery life-time [142, 143]. The current research on BTMS is scattered across single-phase forced convection [144] that does not provide the cooling efficiency required for heavy-duty vehicles, convective flow-boiling that requires large quantities of cooling liquid to be circulated, and pool-boiling immersed cooling technique [9] that cannot sustain beyond a few charge-discharge cycles. This is where single-phase immersion cooling through dielectric liquids can be proposed as an attractive technique to cool electric vehicle components, especially the battery pack [145], and in addition, prevent huge pumping losses and eliminate the requirement of huge heat exchangers.

Along the lines of developing novel dielectric coolant fluids, identification of rheological properties capable of enhancing the underlying heat transfer processes is expected to maximise the effectiveness of future BTMS. New-generation coolants based on oils with macromolecule additives such as polymers and nanoparticles are investigated in recent literature [146–148]. These liquids show enhanced thermal properties, but at the same time have complex rheology exhibiting characteristics of both liquids and solids as a response to forces and time, leading to simultaneous flow, deformation and elasticity [149, 150, 87]. Dilute polymer solutions based on mineral, synthetic or silicone oils belonging to the category of complex-rheology fluids are seen as promising yet unexplored candidates to serve as heat transfer liquids. Unlike nanoparticles, the polymer chains at dilute concentrations do not significantly influence the bulk thermodynamic and transport properties of the oil, nevertheless they modify its rheological behaviour in a manner that can be controlled using the polymer chemistry. The addition of long-chain polymers as viscosity modifiers (VM) in the base oil leads to the onset of flexible micelles that can form complex networks under shear [11]. This behaviour is macroscopically perceived as viscoelasticity, which can be tailored at the molecular scales to manipulate the fluid rheology in a pre-specified manner. Consequently, it helps in controlling the magnitude of vortices generated, which in turn leads to high heat transfer coefficients as explained recently by Wu et al. [151] Karathanassis et al. [96] linked the effects of the different chemistries of the polymers in dilute solutions and the vorticity-magnitudes in flows through complex hydraulic

circuits. Khan et al.[152] showed that the dispersed polymers imparting viscoelasticity can stabilise vortices, and reduce the thermal boundary layer to increase the heat transfer. Thus, a viscoelastic liquid leading to increased vorticity in wall-confined flows, while also retaining the pressure-loss penalty moderate by its shear thinning nature, would constitute an ideal heat transfer medium for immersion cooling applications.

Viscoelastic fluids can also exhibit a shear thinning nature caused by stretching, alignment and decomposition of the microstructures [153, 154]. Pimenta and Campos [155] discussed how a combination of shear thinning and viscoelasticity in case of dilute polymer solutions lead to non-Newtonian behaviour that helps in the reduction of frictional losses, improving pumping performance. At the same time, it is shown that high elasticity hinders this reduction. In essence, a simultaneous understanding of their rheological and heat transfer characteristics is needed, since dimensionless numbers such as Weissenberg number (defined by viscosity and relaxation time) and Nusselt number (defined by thermal conductivity) eventually designate fluid cooling performance [156, 157]. Parvar et al. [158] have recently reported how increasing elasticity of polymer solutions increase their Nusselt numbers and decrease the thermal boundary layer during laminar flow of these solutions.

To propose a liquid for an application where rheology and transport properties are of significance, we need to systematically characterise the relevant properties as a function of important operational parameters such as temperature. There are experimental challenges when it comes to analysing the properties related to the liquids of interest such as polymer relaxation time, normal stress differences, mixture viscosity as a function of shear, etc [101, 159, 133, 160]. To give insights into the non-Newtonian characteristics bestowed upon by the addition of polymers, the properties of the polymer solution have to be compared to that of the base solvent. In this study, we simulate a widely available synthetic oil called polyalphaolefin (PAO-2) having a kinematic viscosity of 2 cSt or 2 mm^2 s^{-1} at 373 K. The oil forms the base solvent of several lubricants. The PAOs have high viscosity index, high fluidity at lower temperatures and high oxidative/chemical stability. Such properties are beneficial for heat transfer applications [161]. In addition, lower molecular weight olefins such as PAO-2 exhibit biodegradable properties [162]. PAO-2 has a pour point of $\sim$ 200 K [163], and is liquid at room temperature. The flash point is $\sim$ 431 K [163] making it safer to use as a coolant in various electromechanical devices.

Among the polymer additives mixed in PAO-2 solvent used for industrial purposes, an ethylene-propylene co-polymer known as olefin co-polymer (OCP) is an important one [164]. The straight structural architecture and narrow molecular weight distribution of OCP make it a good thickener compared to other polymer chemistries [165]. OCP tends to behave differently based on the solvent it is dispersed in [166, 167]. Therefore, the thermophysical properties of a single OCP chain dissolved in PAO-2 solvent must be determined in order to study the extent

of its capabilities. It eliminates any impact due to the polymer concentration and resulting entanglements, revealing its intrinsic nature.

Classical molecular dynamics (MD) constitutes an ideal modelling approach to conduct an in-depth property analysis of molecularly-specific polymer solutions. There are limited number of studies available in the open literature that focus on the computation of thermophysical properties of the fluid of our interest using atomistic MD [168, 169]. In this study, we focus on how the molecular interactions impact the flow rheology. More specifically, we compare and contrast the properties of bare PAO-2 solvent and a single OCP polymer dispersed PAO-2 solution for temperatures in the range of 293 K and 373 K. The temperature range is significant to the operating conditions of electric vehicle components such as the Li-ion battery pack, electric motor and high speed gear-box [170–172]. We study the impact of the polymer chain on the molecular structural changes in the solution and see its relationship with the rheological properties. In addition to this, the thermal conductivity changes made by the polymer addition are also analysed in this investigation. The polymer solution shows improvement in shear thinning, and OCP shows flexible chain characteristics depicted by its radius of gyration in the solution. This work is the first to indicate the molecular basis for using oil-based solutions with dispersed polymeric chains for immersion-cooling applications.

2.2 Simulation details

Pure PAO-2 solvent, and the polymer solution consisting of a single OCP polymer chain in PAO-2 solvent at various temperatures and atmospheric pressure are simulated in this work. L-OPLS-AA [173, 174] force-field of the following generic form is used in this simulation to model the interactions:

$$
\begin{aligned}
V(r) = & \sum_{bonds} k_b (b - b_0)^2 \\
& + \sum_{angles} k_\theta (\theta - \theta_0)^2 \\
& + \sum_{dihedrals} \sum_{n=1}^{4} k_\phi (1 + (-1)^{n-1} \cos(n\phi)) \\
& + \sum_{vdW} 4\varepsilon_{ij} \left[\left(\frac{\sigma_{ij}}{r_{ij}} \right)^{12} - \left(\frac{\sigma_{ij}}{r_{ij}} \right)^6 \right] \\
& + \sum_{Coulomb} \frac{q_i q_j}{\varepsilon_0 r_{ij}}.
\end{aligned}
\tag{2.1}
$$

Here, the first three terms on the right-hand side compute the bonded interaction energies due to bond stretching, bending and torsions. The last two terms compute the interactions due to van der Waals and electrostatic forces. The force-field parameters such as the bonding energies, Lennard-Jones (LJ) interaction parameters to model van der Waals energies, and partial charges to model the electrostatics are tabulated in Table A1 to Table A4 in Appendix A [173, 175, 176, 174, 177]. The LJ parameters (ε_{ij} and σ_{ij}) for the interactions between dissimilar atoms are computed as the geometric mean of the LJ parameters of the individual atom types (ε_{ii} and σ_{ii}).

In this study, 9,10-dimethyloctadecane ($C_{20}H_{42}$) is used to represent PAO-2 solvent, as the compound has been predominantly found in the PAO-2 oil [178]. The pure solvent simulation box is created using 170 molecules of 9,10-dimethyloctadecane [179]. The OCP polymer chain studied here is made up of 50 mole percent of ethylene (C2) monomers and 50 mole percent propylene (C3) monomers with a molecular mass of 3016 g mol^{-1}. The polymer of this particular weight and chain size is chosen as it provides low relaxation times representative of weakly viscoelastic liquids. The chain consists of 43 molecules each of C2 and C3 monomers with the two ends of the chain terminated using hydrogen atoms. Figure 2.1 shows the schematic of the solvent and polymer chain molecular structure studied in this work. The polymer chain is added to the solvent simulation box to create a polymer solution of concentration ≈ 5.9 percent by weight. The individual molecules and the simulation box have been generated using Moltemplate software [180]. Hereafter, the pure PAO-2 solvent simulation system is termed as 'pure solvent' and the polymer solution system is termed as 'polymer solution', unless specified otherwise. The initial three-dimensional simulation box size of pure solvent is $100\times100\times100$ Å^3. The corresponding box size of polymer solution is $250\times100\times100$ Å^3. We apply periodicity in all 3 directions of the boxes to simulate bulk liquids.

Large-scale Atomic/Molecular Massively Parallel Simulator (LAMMPS) [50] is used for the MD simulation of pure solvent and polymer solution. The study here is carried out to compute properties between a temperature range of 293 K and 373 K. The properties of the systems are computed at five different temperatures at intervals of 20 K for this purpose. We use Nosé-Hoover thermostat to maintain the temperatures at various stages of the equilibrium MD. The corresponding barostat as implemented by LAMMPS is used to set the pressures. The distance cut-off for van der Waals interactions is set to 13 Å. A faster Ewald summation methodology called particle-particle-particle-mesh (PPPM) is used to compute the long-range electrostatic interactions [48]. Velocity Verlet algorithm [34] is used to integrate the equations of motion with a time-step of 1 fs.

In order to model the alkanes having more than 16 carbon molecules by OPLS-AA force field, it is recommended to switch-off the 1-4 intra-molecular non-bonded pairwise interactions
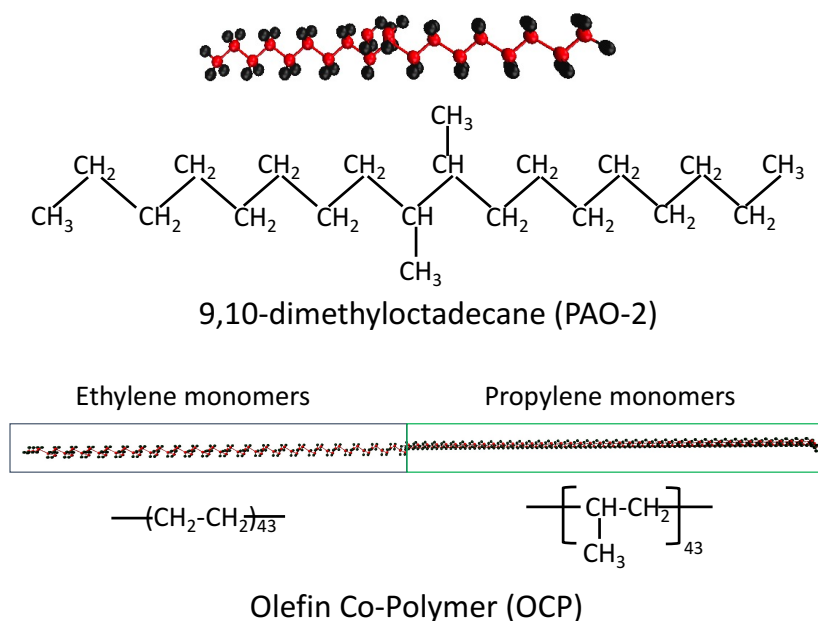
Figure 2.1: Schematics of the solvent - PAO-2 molecule and polymer chain - OCP molecule used in this simulation study.

[168, 181].That is, the weighting coefficients of the computed pairwise forces and energies between the first and fourth atom connected covalently in a molecule is 0.0. However, in our case (while using L-OPLS-AA parameters) such a modification overestimates density values of pure solvent for temperatures between 313 K and 373 K by 0.01 g cm^{-3}. To rectify it, we increase the weighting contribution of 1-4 intra-molecular non-bonded pairwise interactions for pure solvent systems to 0.5 for simulations between 313 K to 373 K. On the other hand, it is set to 0.0 at all temperatures for polymer solution to obtain appropriate thermodynamic properties.

Pure solvent and polymer solution systems remain liquids in the temperature range simulated. The equilibrium MD simulation protocol for a run at temperature, T = 293 K and pressure, p = 1 atm is as follows: The systems are initially energy-minimised using conjugate-gradient algorithm with tolerance values of 10^{-4} and 10^{-6} for energy and force calculations, respectively. Here, a larger neighbour-list skin cut-off of 6 Å is used to prevent the system from destabilisation. The energy-minimised systems further undergo a constant enthalpy (NPH) simulation for 2000 fs using a Langevin thermostat at the desired temperature. This step is used to expedite the process of equilibration [179, 182]. Following that, the system is further equilibrated under NPT conditions where Nosé-Hoover thermostat and corresponding barostat are applied to maintain temperature and pressure, respectively. The changes in stress occur isotropically. At this stage, the neighbour-list cut-off is reduced to 2 Å to speed-up computations. Once the system is equilibrated for 20 ns under NPT, the resulting configuration undergoes an annealing

process where, the simulation system is gradually run at higher temperatures of 298 K, 303 K, 308 K, 313 K and 318 K for 1 ns each under constant NVT conditions. The system is rapidly brought back to 293 K following that under NVT and run for 1 ns to complete the process of annealing. The time invariance of the radial distribution functions of atoms as shown in Figure A1 in Appendix A establishes that the system is well equilibrated after these steps. The equilibrated and annealed system is used for a production run of 40 ns under NVT. The trajectories of the atoms are stored at regular intervals to compute the properties. The reported values of properties at a typical temperature are obtained from three independent runs. The protocol followed to compute properties using non-equilibrium MD methods is discussed in the relevant sections below.

2.3 Results and discussion

The following section discusses the different computational approaches used to determine the various properties, and assesses the results. The force-field is validated initially for the pure solvent system comparing the density (ρ) values against data available in the literature. The simulated isothermal compressibility (κ_T) of pure solvent is also compared against experimental measurements to validate the thermodynamics of the system. The transport properties such as self-diffusion coefficient, zero-shear viscosity, and thermal conductivity are computed and compared in case of pure solvent and polymer solution systems. Furthermore, the shear thinning behaviour of the liquids and the underlying reasons owing to their molecular interactions are analysed. Subsequently, the relaxation times of the polymer as a function of temperature and shear rate are estimated to characterise the viscoelastic nature of the polymer solution.

2.3.1 Thermodynamic properties of pure solvent

The validation of the force-field is done by computing certain important properties and verifying its agreement with data in the available literature. In this work, PAO-2 is treated as a homogeneous compound of 9,10-dimethyloctadecane. Therefore, it is important to see how well the thermodynamic properties represent the actual PAO-2 oil.

The first property analysed is the pure solvent density (ρ_0). The densities are computed from the NPT equilibration runs for pure solvent. The average values are reported in Table 2.1 along with their standard deviations. As expected, ρ_0 of pure solvent decreases with temperature. Comparison of the values with the data in the available literature shows a good agreement.

In addition to density, isothermal compressibility (κ_T) is an important feature that needs to be computed as compressibility of liquids is related to rheology in certain extreme conditions

Table 2.1: Comparison of density (ρ_0) of pure solvent systems with experimental values (see Appendix A for further details), and simulated values [179] from literature.

Temperature (K)	Present simulation (g cm^{-3})	Experimental/Literature (g cm^{-3})
293	0.800±0.005	0.793 (Table A5)
313	0.780±0.005	0.780±0.005 [179]
333	0.764±0.005	0.766 (Table A5)
353	0.748±0.005	0.752 (Table A5)
373	0.732±0.006	0.733±0.005[179]

Table 2.2: Tait Equation parameters (B and C) and Isothermal compressibility (κ_T) of pure solvent systems at various temperatures, and comparison with experimental values. The experimental methodology is described in Appendix A.

Temperature (K)	B(MPa)	C	Simulated $\kappa_T \times 10^{11}$(Pa^{-1})	Experimental $\kappa_T \times 10^{11}$(Pa^{-1})
293	83.58	0.1538	79.42	79.55
313	114.01	0.2168	82.53	89.98
333	101.74	0.213	90.85	101.7
353	74.55	0.191	111.1	115.22
373	43.81	0.149	147.4	-

[183]. Isothermal compressibility of pure solvent in our case is found using the following simulation protocol: The atomic configurations after NPT simulation at $p = 1$ atm are subjected to a set of simulations with p varied from 10 to 1000 atm at a given temperature. The NPT simulation at every p lasts for 10 ns. Density is computed from the average of the final 5 ns run at all conditions of pressure. The data thus obtained is fitted to the modified form of Tait equation [184],

$$\rho = \frac{\rho_0}{1 - C\log_{10}(\frac{p+B}{p_0+B})}. \tag{2.2}$$

Here, ρ_0 is the density of pure solvent at $p_0 = 1$ atm (101325 Pa). The fitting constants C and B are related to κ_T as

$$\kappa_T = \frac{C}{2.302(p_0 + B)}. \tag{2.3}$$

B and C values, and comparison of κ_T with the experimental data are shown in Table 2.2. The ρ data as a function of pressure and the modified Tait equation fits are present in Appendix A (see Figure A2). Simulated κ_T values show a good match with the experimental data. The deviations observed can be attributed to the difference in the empirical model used for the computation of κ_T experimentally (see Equation A4 in Appendix A).

The computed thermodynamic properties show that use of L-OPLS-AA force-field and 9,10-dimethyloctadecane as a surrogate for PAO-2 oil are suitable to represent the systems of our interest in MD simulations. Therefore, we model polymer solution using the same force-field. Please see Table A6 in Appendix A for the thermodynamic properties of the simulated polymer solution. The other computed properties and their physical significance are described in the following sections.

2.3.2 Zero-shear viscosity

The Newtonian dynamic viscosity (η_0) is the most fundamental transport property measured to analyse the flow behaviour of the complex heat transfer liquids [185, 186]. The variation in η_0 is an indication of the translational resistance to flow [187]. It is computed in MD using the Green-Kubo method based on the fluctuation-dissipation theorem of systems in equilibrium. η_0 is computed by the integration of a decaying stress auto-correlation function [188], such that

$$\eta_0 = \frac{V}{k_B T} \int_0^\infty \left\langle \sigma_{xy}(t)\sigma_{xy}(0) \right\rangle dt. \tag{2.4}$$

Here, V is the volume of the simulation box, k_B is the Boltzmann constant and $\sigma_{xy}(t)$ is one of the off-diagonal component of the stress tensor at time t. The statistics of η_0 computation is improved by taking an average of the auto-correlation function of the three off-diagonal components of the stress-tensor. In case of oils, the values of viscosity are reported in terms of kinematic viscosity (v_0) given as

$$v_0 = \frac{\eta_0}{\rho}. \tag{2.5}$$

Figure 2.2 shows v_0 at various temperatures for pure solvent. Our simulated values are close to the reported experimental and simulation results of PAO-2 in literature [189, 179]. The viscosity values decrease with temperature, which is expected in case liquids of this nature [190, 191]. As also shown in Figure 2.2, the simulated values of polymer solution are higher than those of pure solvent at all temperatures. This implies that OCP polymer leads to viscosity enhancement when added to the PAO-2 solvent.

The relationship of viscosity of polymer solutions with temperature can be modelled using an Arrhenius-like equation

$$ln(v_0) = ln(v_{0c}) - \frac{E_a}{RT} \tag{2.6}$$

fitted to the data of v_0 vs. $1/T$. Here, v_{0c} and E_a are the fit constants. The E_a values are dependent on the nature of polymer and solvent, and polymer concentration [192, 193]. Figure A3 in Appendix A shows the Arrhenius fits to the data for pure solvent and polymer solution
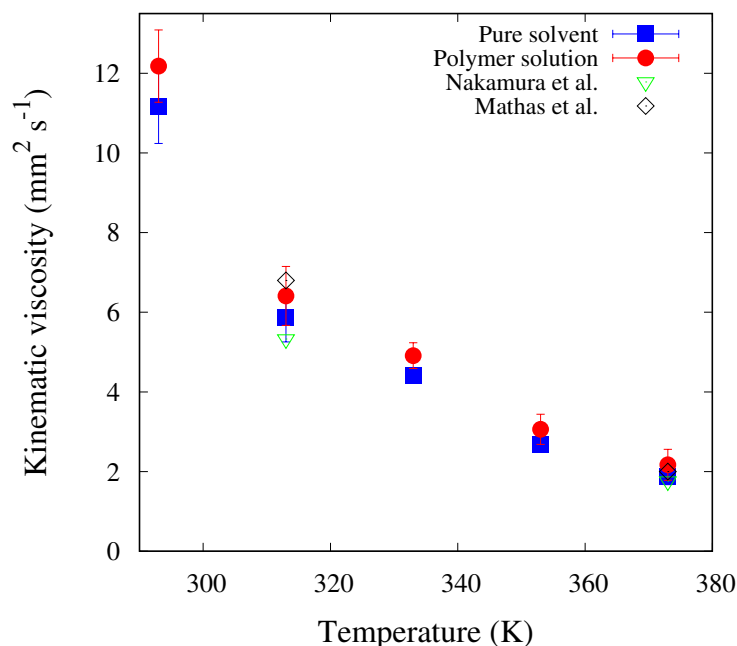
Figure 2.2: The kinematic viscosity (ν_0) of the pure solvent system and polymer solution as a function of temperature. The closed symbols represent the average of simulated values - red (Pure solvent) and blue (Polymer solution) with their standard deviations from the three independent runs. The open symbols represent the experimental [189] (green) and simulated [179] (black) data available in the literature for pure solvent system.

systems. The E_a values of the former is 21.0 ± 1.6 kJ mol^{-1} and of the latter is 20.3 ± 1.7 kJ mol^{-1}. The values show that at this concentration of OCP, the polymer does not cause a significant impact on the temperature dependence of the viscosity of the solution.

Given that the viscosity rise with addition of OCP polymer chain, we can look if the molecular transport of the different components due to thermal motion supports the observation. We compute self-diffusion coefficient in this regard.

2.3.3 Self-diffusion coefficient

The self-diffusion coefficient (D) is a measure of the translational movement of atoms and molecules due to the thermal energy of the system. In case of long-chain hydrocarbon systems, D can be computed for the constituent atoms, monomers (in case of polymers) or the centre of mass (COM) of the molecules. In our case we compute D of COM (D_{COM}). Usually, D_{COM} of a homogeneous system is inversely related to η_0. MD uses Einstein's relation [16, 194] to

compute D_{COM} such that

$$D_{COM} = \frac{1}{6} \lim_{t \to \infty} \frac{d}{dt} \left\langle [\mathbf{r}_{COM}(t) - \mathbf{r}_{COM}(0)]^2 \right\rangle \qquad (2.7)$$

where $[\mathbf{r}_{COM}(t) - \mathbf{r}_{COM}(0)]^2$ is the mean squared displacement (MSD) of the centre of mass of a molecule. The symbol $\langle \rangle$ is the ensemble average symbol. The relationship is applicable at long-time limits, where the MSD enters the linear regime. Here, the slope of MSD (computed via multiple time origins) beyond 10^5 fs from a linear function fit is used to compute D_{COM} (see Figure A4 in Appendix A). Figure 2.3a shows the variation of D_{COM} with temperature of molecules in case of pure solvent and polymer solution.

$D_{COM,PAO}$ is system-size independent as shown by the comparison of the MSD values of a larger pure solvent system consisting of 340 molecules with the one studied here (see Figure A5 in Appendix A). With increase in temperature, pure solvent shows an increase in $D_{COM,PAO}$. This behaviour is opposite to that of the Newtonian viscosity as a function of temperature. The implication is that kinetic energy gained by the molecules with increase in temperature assists in overcoming intermolecular forces of attraction (that causes resistance to motion). Coming to the polymer solution, we compute the diffusivity of PAO-2 solvent molecules and diffusivity of OCP polymer chain. The $D_{COM,OCP}$ of the polymer is considerably lower (by an order of magnitude) compared to that of the solvent molecules at all temperatures (see Figure 2.3b). This is expected in case of a large molecule such as OCP. The addition of OCP decreases the D_{COM} of PAO-2 molecules as seen in Figure 2.3a indicating that the polymer chain restricts the free motion of PAO-2 molecules. This relates to the enhancement in viscosity of the polymer solution system compared to that of the pure solvent system.

A direct impact of the polymer additive as a VM in polymer solution is observed from the analysis of the transport properties. Therefore, it is imperative to further look into the mechanism of viscosity enhancement in case of polymer solution. For that purpose, we have to probe the structural characteristics of the pure solvent and polymer solution systems as shown later in the chapter.

2.3.4 Couette flow

The primary objective of the rheological characterisation is to elucidate the non-Newtonian behaviour of the polymer solution. In order to do so, we first analyse the shear response of the pure solvent and polymer solution systems by simulating a Couette flow of the bulk liquids. We use a non-equilibrium MD (NEMD) simulation methodology to carry out the simulations, which enables the characterisation of shear thinning onset in the examined fluids.
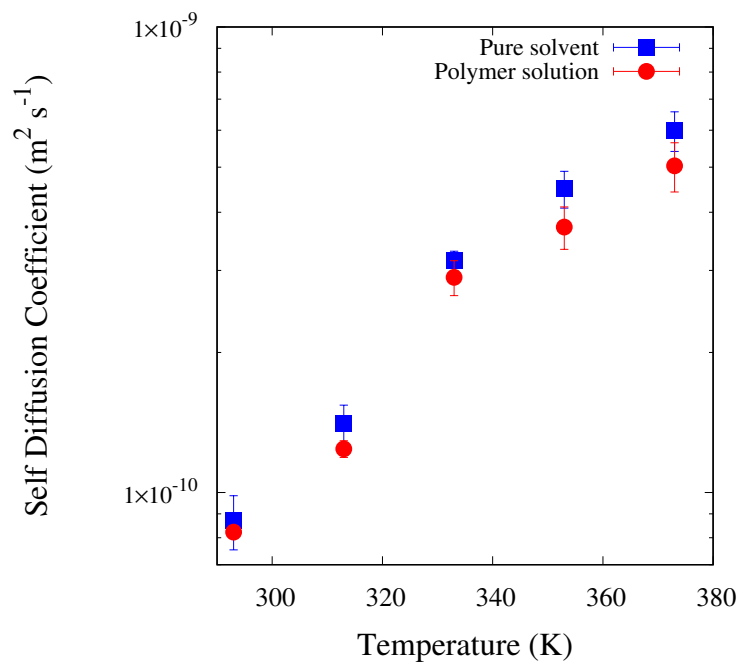
(a)
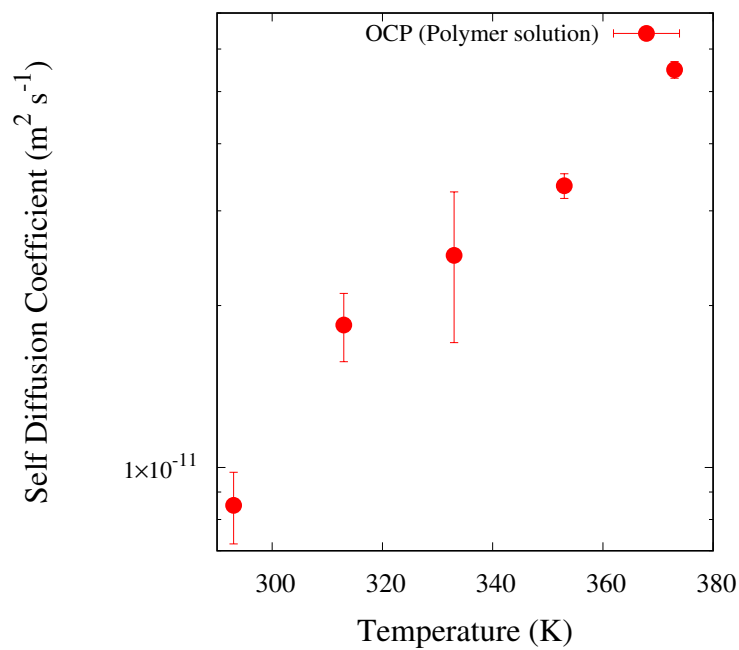
(b)

Figure 2.3: The centre of mass self diffusion coefficient of (a) PAO-2 molecules ($D_{\text{COM,PAO}}$) in the pure solvent and polymer solution systems, and (b) OCP molecule ($D_{\text{COM,OCP}}$) in the polymer solution system as a function of temperature.

The Couette flow of an MD simulation box with periodic conditions is implemented here by deforming the box in y-direction. A Lees-Edwards boundary condition is applied to ensure stability of the system [195, 196]. We use SLLOD equations of motion to solve for the trajectories of the atoms as derived by Hoover and Ladd, and Evans and Morris [51, 197]. They ensure the conservation of momentum, and account for the accurate values for dissipated energy. The extent of deformation can be defined in LAMMPS by a constant engineering shear strain rate ($\dot{\gamma}$). The resulting flux of stress (σ_{yz}) is used to compute the viscosity ($\eta(\dot{\gamma})$) as a function of the $\dot{\gamma}$ such that

$$\eta(\dot{\gamma}) = \frac{\sigma_{yz}}{\dot{\gamma}}. \tag{2.8}$$

In atomistic MD, the flow is established only at very high $\dot{\gamma}$, which is not experimentally achievable, and this constitutes as a shortcoming of MD [198]. However, we can still characterise the rheological behaviour by fitting the following Carreau-model to the data of $\eta(\dot{\gamma})$ vs $\dot{\gamma}$:

$$\eta(\dot{\gamma}) = \frac{\eta_0}{(1 + (\tau_s\dot{\gamma})^2)^m}. \tag{2.9}$$

Here, η_0 is the Newtonian viscosity that is obtained from the extrapolation of the data to $\dot{\gamma} = 0$. m is the strain-rate sensitivity coefficient. τ_s is the time constant referring to the shear rate where the shear thinning begins. $\dot{\gamma}$ values between the range of 10^8 s^{-1} and 10^{11} s^{-1} are applied to the simulation box. The model has been shown to fit the response of viscosity as a function of shear rate quite well in case of long chain hydrocarbons in the MD literature [181, 169].

Figure 2.4a shows the viscosity vs shear rate data and the corresponding Carreau-model fits at 313 K and 373 K. As seen, the simulated data has large error bars at lower shear rates and their magnitudes decrease at higher shear rates. It can be clearly discerned that η_0 of polymer solution is greater than that of pure solvent at both the temperatures. The comparison of η_0 computed by equilibrium MD from Equation 2.4 and by NEMD from Equation 2.9 in Table A7 in Appendix A shows fairly good agreement at all temperatures.

A polymer additive that increases the viscosity of a solvent can either be a thickening agent or a viscosity index improver (VII). OCP can be classified as the former if the increase in viscosity is independent of temperature, whereas it is classified as the latter if it increases viscosity only at higher temperatures. A method to identify if a polymer really acts as a VII or simply as a thickening agent is to compute the Q factor [181]. It is computed as

$$Q_{\text{VI}} = \frac{\eta_{sp,373K}}{\eta_{sp,313K}}, \tag{2.10}$$
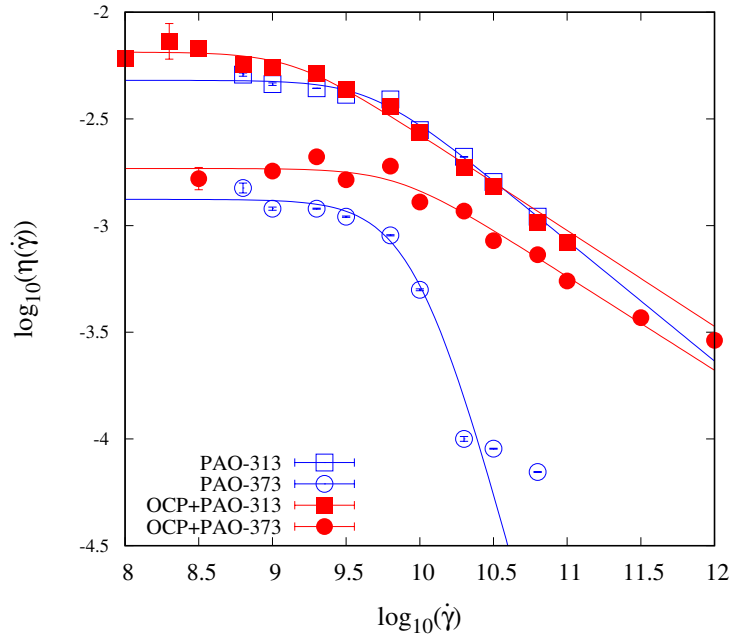
(a)
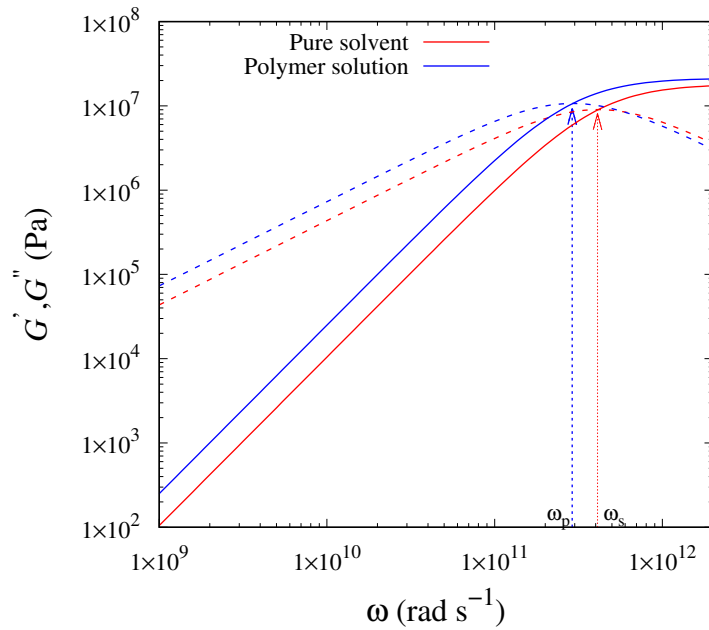
(b)

Figure 2.4: (a) Viscosity ($\eta(\dot{\gamma})$) as a function of shear rate ($\dot{\gamma}$) at two different temperatures (313 K and 373 K) in pure solvent and polymer solution systems. The symbols with the error bars show the simulated dynamic viscosity values, $\eta(\dot{\gamma})$ at different shear rates, $\dot{\gamma}$ in the logarithmic scale. The lines depict the Carreau-model fittings. (b) The storage modulus, G' (solid) and the loss modulus, G'' (dashed) as functions of ω at a temperature of 313 K with the arrows indicating the cross-over ω values for pure solvent (ω_s) and polymer solution (ω_p).

41

where $\eta_{sp,373K}$ and $\eta_{sp,313K}$ are the specific viscosities at 373 K and 313 K, respectively, calculated as

$$\eta_{sp} = \frac{\eta_{solution} - \eta_{solvent}}{\eta_{solvent}}. \tag{2.11}$$

$Q_{VI} \leq 1$ for a substance that acts more as a thickening agent and $Q_{VI} \gg 1$ for an additive that acts more as a VII.

Table 2.3 shows the parameters of the Carreau-model for pure solvent and polymer solution systems. The fitted curves (as shown in Figure 2.4a) have R-squared values greater than 0.95. The Q factor computed from the η_0 values is 0.86. This is indicative of the uniform thickening nature of the OCP polymer chain when added to PAO-2 solvent. It confirms the observations derived from experimental investigation of OCP of higher molecular weights and different compositions [166]. The study here substantiates that it is the intrinsic nature of OCP chain to act as a thickening agent in an olefin-based oil, independent of the composition or dispersity of the polymer.

Table 2.3: Parameters of Carreau-model (η_0, τ_s, m) at various temperatures.

Pure solvent			
Temperature (K)	η_0 (Pa s)	τ_s (ns)	m
293	0.009	0.62	0.30
313	0.0048	0.31	0.28
333	0.0033	0.22	0.31
353	0.0021	0.20	0.24
373	0.0013	0.10	1.32
Polymer solution			
Temperature (K)	η_0 (Pa s)	τ_s (ns)	m
293	0.0130	0.95	0.26
313	0.0065	0.73	0.22
333	0.0039	0.34	0.23
353	0.0025	0.21	0.22
373	0.0017	0.14	0.22

While comparing the τ_s values in Table 2.3 for pure solvent as a function of temperature, we see that they decrease with temperature. In case of polymer solution, τ_s decreases with temperature as well. However, the τ_s values are higher in case of the polymer solution compared to that of pure solvent. This indicates that addition of OCP enhances the shear thinning behaviour of the simulated polymer solution. The viscoelastic nature of the polymer chain contributing to this phenomenon can be verified by comparing the storage ($G^{'}$) and loss moduli ($G^{''}$) of the two different liquids. In order to compute the two moduli, the integrand

function in Equation 2.4

$$G(t) = \frac{V}{k_B T} \left\langle \sigma_{xy}(t) \sigma_{xy}(0) \right\rangle \tag{2.12}$$

is fit with an exponential function

$$G(t) = G_0 e^{-\left(\frac{t}{\tau_f}\right)} \tag{2.13}$$

with a single Maxwell mode, as implemented generally in case of macroscopic models of polymer chains such as finite extensible non-linear elastic polymer (FENE-P) model [199]. The τ_f value represents relaxation time of the fluid, and G_0 represents the ordinary elastic shear modulus. From the Fourier transformation of the above equation, the storage and loss moduli can be further obtained from the following relationships:

$$G'(\omega) = G_0 \frac{\omega^2 \tau_f^2}{1 + \omega^2 \tau_f^2} \text{ and } G''(\omega) = G_0 \frac{\omega \tau_f}{1 + \omega^2 \tau_f^2}. \tag{2.14}$$

The correlation data in Equation 2.12 is smoothened by following the process recommended in literature before applying Equation 2.13 to the data [200] (see Figure A6 in Appendix A). Figure 2.4b shows G' and G'' as functions of ω at 313 K. As observed, the addition of polymer leads to an increase in the values of $G'(\omega)$ and $G''(\omega)$. This indicates that polymer solution has higher elasticity and viscosity, respectively than the pure solvent. The inverse of the ω where the crossing of $G'(\omega)$ and $G''(\omega)$ happens, provides the fluid relaxation time. As expected, ω of the polymer solution (ω_p) is lower than that of the pure solvent (ω_s). In other words, the relaxation time increases with the addition of the polymer chain in the solvent. This enhances the vortex roll-up and subsequent thermal behaviour of the polymer solution compared to that of the solvent.

It is natural for long-chain hydrocarbon solvents to showcase shear thinning at very high shear rates simulated in MD even though the shear rates at which macroscopic flow is observed, i.e., between the range of 10^1 - 10^6 s^{-1}, portray them as Newtonian. The reasons for the shear thinning nature of oil and long-chain hydrocarbons are described in the literature [201–203]. Given this scenario, the shear thinning of polymer solution triggered at lower shear rates than that for solvent emerges from the impact of polymer on the molecular interactions [204]. Therefore, the consistent enhancement of viscosity and the shear thinning behaviour at all temperatures observed with the addition of OCP requires further understanding in terms of the structural changes at the molecular level.

2.3.5 Structural characteristics

In the general polymer theory [205, 206], the reason for increasing viscosity as a function of temperature of a polymeric fluid is attributed to increasing hydrodynamic radius of the polymer chain. As temperature increases, the polymer chains expand which in turn improves the viscosity of the polymer fluids. A measure of the hydrodynamic radius is given by the radius of gyration (R_g) computed by the equation

$$R_g = \sqrt{\frac{1}{M} \sum_{i=1}^{n} m_i (\mathbf{r}_i - \mathbf{r}_{\text{com}})^2} \qquad (2.15)$$

where M is the mass of a molecule, m_i is the mass and $\mathbf{r}_i$ is the position vector of an atom i of a molecule consisting of n atoms. The computed values of R_g of the OCP polymer are shown in Figure 2.5a. The large error bars at every temperature depict the relative ease with which the shape of polymer chain changes. The mean values of R_g of OCP do not depict a significant monotonic increase as a function of temperature. This is in line with the findings in literature that exhibit that polymer chains composed of aliphatic monomers do not show an increase in R_g with temperature when dissolved in aliphatic solvents [166]. Therefore, polymer coil expansion cannot be considered as the reason for viscosity improvement with temperatures for all the chemistries.

Another important factor that can be probed as the reason for viscosity improvement is the impact of temperature on the solvent molecules configuration in polymer solution. Here, we compare and contrast the hydrodynamic radii of PAO-2 molecules in pure solvent and polymer solution systems. Figure 2.5b shows the R_g of PAO-2 molecules in the two different liquids. The data clearly presents that there is a significant jump in the R_g of PAO-2 molecules in polymer solution from the R_g of the same in pure solvent. However, the mean values are constant as a function of temperature. It implies that the impact of thickening of the solvent due to the presence of OCP polymer is uniform throughout the temperature range. The relationship of this behaviour with dissolved OCP chemistry has been sparsely studied. Few reasons suggested in existing literature are lack of long side chains to improve the solubility in olefins at higher temperatures [207], and absence of oxygen atoms in OCP chain that can change its conformations significantly at different temperatures [208, 168]. Even though not dealt in the present study, it is important to further probe on the causes for why OCP remains a weak VII in solvents such as PAO-2.

As discussed in the previous section, the shear thinning observed in case of these liquids with deformation can be attributed to their molecular configurations. The configurational changes contributing to this phenomenon is an interplay of chain stretching, tumbling, and molecular
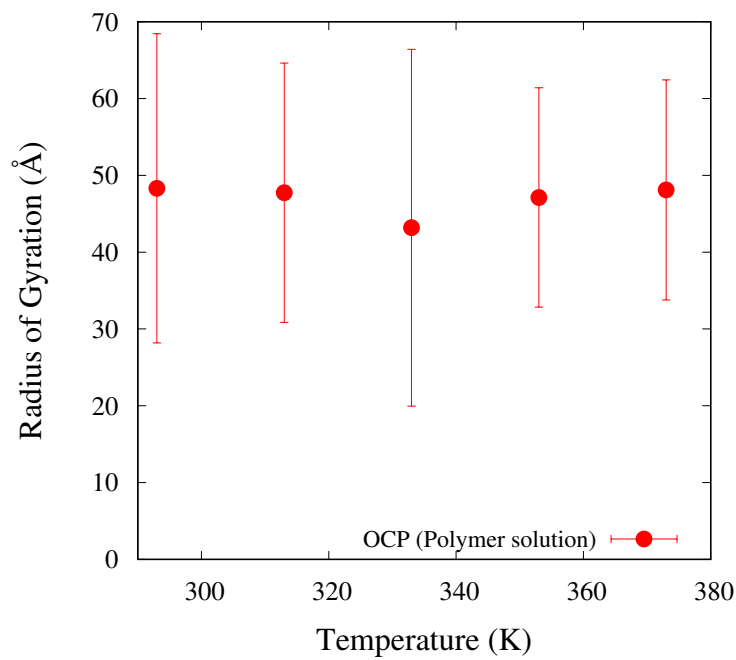
(a)
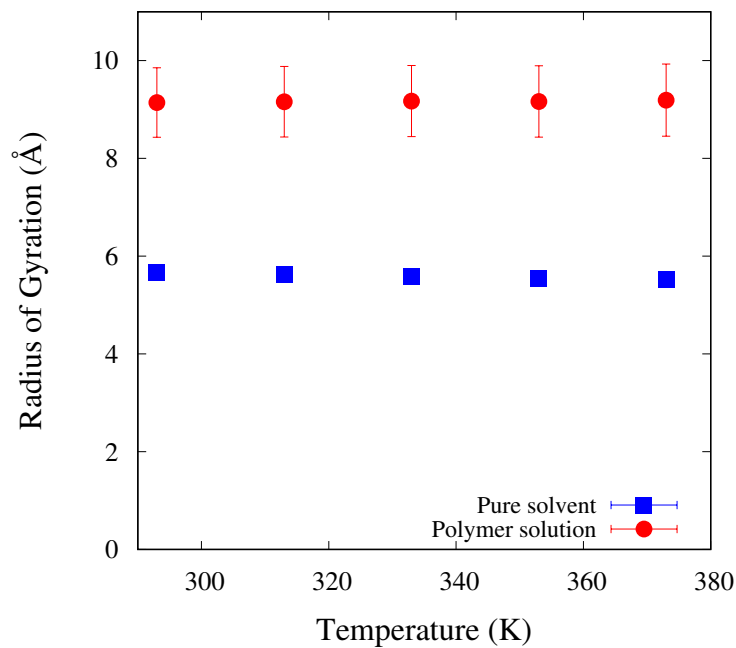
(b)

Figure 2.5: The radius of gyration (R_g) of (a) OCP molecule in the polymer solution, and (b) PAO-2 molecules in the pure solvent and polymer solution as a function of temperature. The error bars show the standard deviation computed from the R_g values obtained at every 2 ps in the three independent runs.

45

alignment [209–211, 201]. Firstly, to analyse the impact of stretching, the computation of the end-to-end distances (R_e) of the solvent molecules and the polymer chain is done. In our case, we use the position vectors of the carbon atoms at the terminal ends of the PAO-2 and OCP for the purpose of the computation of R_e of molecules. The end-to-end distance as a function of shear rate shows the significance of polymer stretching on the shear thinning behaviour (see Figure A7 in Appendix A). R_e of OCP increases from 22 Å at zero shear rate to 25 Å at the highest shear rate simulated, implying stretching. At the same time, R_e of PAO-2 molecules remains constant as a function of $\dot{\gamma}$ indicating that a maximum stretch has already been attained by the solvent molecules at zero shear rate.

A method to assess the alignment of the molecules as a response to the shear has been discussed by Datta et al. [120] in coarse-grained simulations. It involves the computation of the ratio of the y-component of squared end-to-end distance (R_{ey}) of the molecules to the total squared end-to-end distance such that

$$S_{\text{alignment}} = \frac{\langle R_{ey}^2 \rangle}{\langle R_e^2 \rangle}. \tag{2.16}$$

This ratio provides the fraction of molecular stretching aligned in the direction of the shear (y-direction). We apply the same methodology in this work. $S_{\text{alignment}}$ should be ideally 1/3 in the absence of any shear as the alignment of PAO-2 molecules should be independent of the direction.
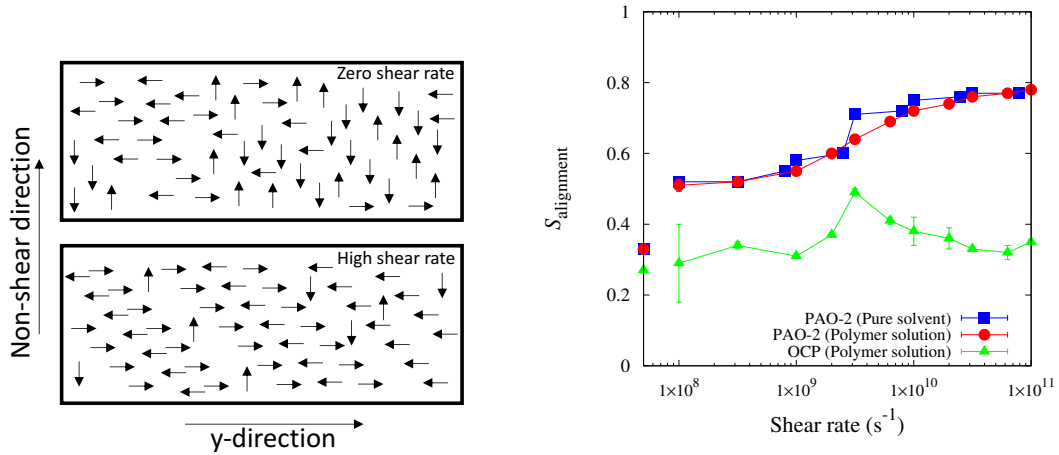
Figure 2.6: (Left) The schematic of molecular alignment in the absence and presence of shear. (Right) $S_{\text{alignment}}$ of PAO-2 and OCP molecules in pure solvent and polymer solution as a function of shear rate at 313 K. The data points on the y-axis show the values of $S_{\text{alignment}}$ at zero shear rate.

Figure 2.6 shows the variation of $S_{alignment}$ of solvent molecules as a function of $\dot{\gamma}$ at 313 K. The value of $S_{alignment}$ at $\dot{\gamma} = 0$ is shown on the y-axis and as expected, it is ≈ 0.33. The value of $S_{alignment}$ increases with increasing shear rate, indicating the alignment of the molecules in the direction of the applied shear and reaching an upper plateau of ≈ 0.79. This makes the liquids susceptible to shear thinning by lowering the fraction of molecules stretching in non-shear directions that create obstacles to shear flow. Consequently, they end with a lower Newtonian viscosity at very high shear rates. While assessing the $S_{alignment}$ of OCP polymer as a function of shear rate in Figure 2.6, we observe a rise in the values to 0.49 in the shear rate range where shear thinning is seen and subsequent drop back to 0.35 once the viscosities reach lower Newtonian plateau. This shows the additional role of alignment of polymer chain stretching on the shear thinning of polymer solution. It is also important to analyse the tumbling effects of OCP chain on the shear thinning observed. However, this is out of the scope of the current study.

We observed here how the addition of the OCP polymer chain influences the viscosity of the resultant polymer solution, and how molecular stretching and alignment influence the shear thinning behaviour of the liquids. We need to further characterise the viscoelastic effects of the polymer chain in the polymer solution systems by computing the polymer relaxation time.

2.3.6 Terminal relaxation time

Under specific circumstances, the viscoelastic behaviour has been linked to the vortex stabilisation and their lifetime [152, 151]. The relaxation time provides a fundamental way to quantify the non-Newtonian viscoelastic behaviour of the liquids. It provides a measure of the time scale during which elastic stresses of polymer coil relax [212]. In case of a single chain of polymer, the longest relaxation time is attributed to the relaxation of the entire chain [213]. It is also called the terminal relaxation time (τ_{term}) of the polymer chain. Here, τ_{term} is computed as a function of temperature (using equilibrium MD), and shear rate (using NEMD).

The polymer chain showed that R_g does not vary significantly as a function of temperature. Therefore, it is important to see the extent of the polymer chain relaxation at different temperatures. For this, we use the end-to-end vector autocorrelation given as

$$C(t) = \frac{\langle \mathbf{R}(t) \cdot \mathbf{R}(0) \rangle}{\langle \mathbf{R}(0) \cdot \mathbf{R}(0) \rangle} \tag{2.17}$$

where, $\mathbf{R}(t)$ is the end-to-end vector $(\mathbf{r}_1 - \mathbf{r}_l)$ of the OCP polymer chain having l monomers. The position vectors of the carbon atoms at the terminal ends of the chain are stored every 10 ps during the simulation run for the purpose of computation. We fit the $C(t)$ using a sum of

three exponential functions as in

$$C(t) = \sum_{i=1}^{3} \alpha_i e^{-\frac{t}{\beta_i}} \tag{2.18}$$

such that the integration of the function gives the terminal relaxation time

$$\tau_{term} = \int_0^\infty C(t)dt. \tag{2.19}$$

A sample of the $C(t)$ and the fit as described by Equation 2.18 is shown in Figure A8 in Appendix A.
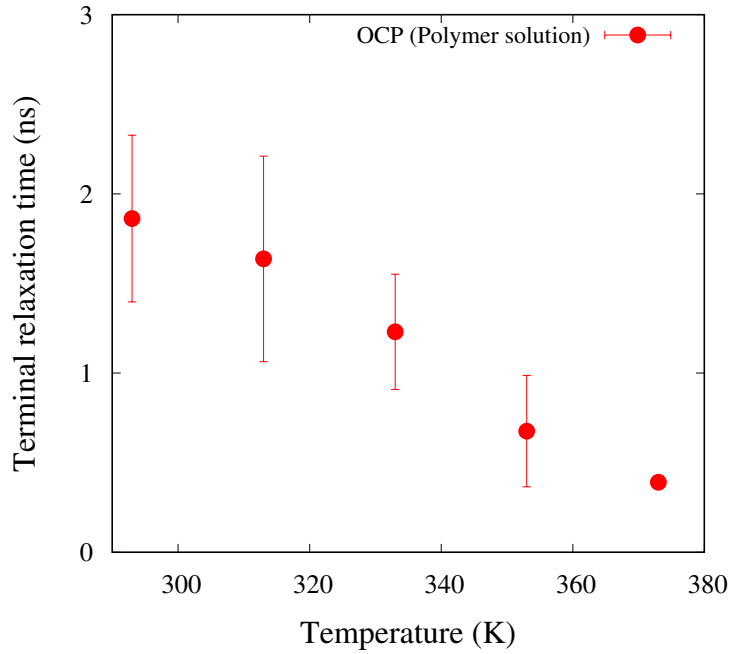
Figure 2.7: The terminal relaxation time (τ_{term}) of OCP in the polymer solution as a function of temperature.

The τ_{term} values of OCP polymer as a function of temperature is shown in Figure 2.7. The obtained values are in the order of nanoseconds. Even though relaxation times of this order of magnitude are plausible for such dilute polymers, it is not possible to compute them using the existing experimental apparatuses [102, 103]. The values clearly show that the terminal relaxation time of the polymer chain decreases with temperature.

Understanding the response of the polymer chain relaxation as a function of shear rate is also vital to prescribe the complex fluid. Here, we compute τ_{term} as a function of $\dot{\gamma}$ by implementing Couette flow as explained earlier. The τ_{term} for the same range of $\dot{\gamma}$ values (10^8

s^{-1} and 10^{11} s^{-1}) are found. The position vectors of the terminal carbon atoms are used for the computation of τ_{term} here as well.

Figure 2.8 shows the values of τ_{term} as a function of $\dot{\gamma}$ at temperatures of 313 K and 373 K for polymer solution. The data is obtained as the average from three independent runs and the error bars show the standard deviation of the results from the three runs. The values at both the temperatures show huge error bars but a downward trend as a function of $\dot{\gamma}$. This implies that, as the shear forces on the polymer solution increase, the polymer tends to achieve an equilibrium configuration faster. Higher the relaxation time, stronger the elastic nature of the polymer chain. The changes in relaxation times as a function of both temperature and shear rate imply that the magnitude of vortices will vary with the operating conditions of the cooling liquids. Since the elastic instabilities facilitate the manifestation of vortical motion, the operating temperature and shear rates must be kept lower in magnitudes. Even though the relaxation time can be increased by polymer concentration, it can negatively influence the pumping losses.
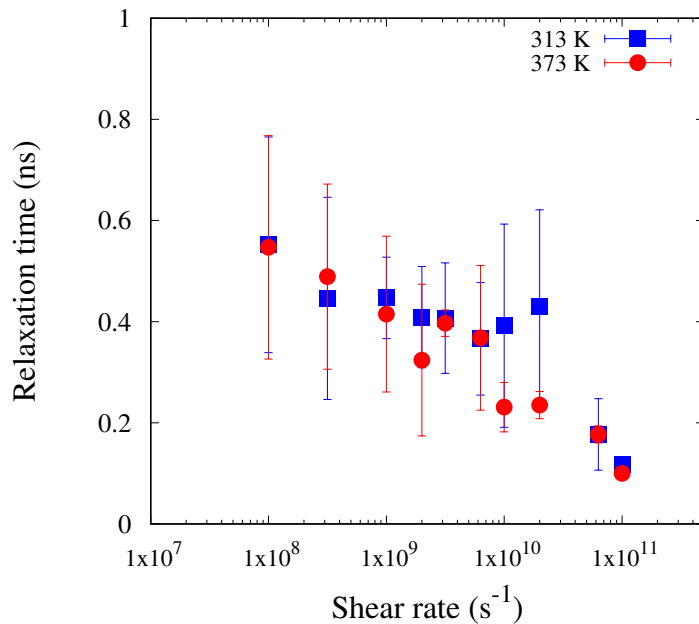
Figure 2.8: The terminal relaxation time (τ_{term}) of OCP in the polymer solution as a function of shear rate at two different temperatures (313 K and 373 K).

2.3.7   Thermal conductivity

Having understood the rheological behaviour of the pure solvent and polymer solution systems, it is important to further know the thermal transfer properties. For a fluid oriented towards heat

transfer applications, thermal conductivity (k) is a vital property to be computed. This metric provides a measure of the ability of a fluid to conduct heat given a temperature gradient across it. It is also necessary for the computation of the Nusselt number of novel liquids characterising the ratio of heat transfer via flow convection and conduction [214]. The conduction of heat is due to the microscopic behaviour of the material, making MD a useful tool to calculate it [215].

A methodology prescribed by Müller-Plathe [52] is considered as a reliable way to compute k in case of our systems. The formulation is based on the following relationship as given by Fourier's Law:

$$q = k\frac{dT}{dx} \tag{2.20}$$

where, q is the heat flux across the fluid and $\frac{dT}{dx} = \nabla T$ is the corresponding temperature gradient. Therefore, by implementing a temperature gradient which is linear across the simulation box, the consequent heat flux generated can be utilised to compute k. Müller-Plathe [52] proposed a way to implement the ∇T by routinely exchanging the translational velocities of the atoms in the simulation box. This ensures conservation of momentum as well. Over a long time period, the continuous exchange of the momentum leads to the development of a ∇T across the simulation box. This computational scheme is also referred as reverse-NEMD technique.

In our work, we consider the well-equilibrated and annealed systems from the equilibrium MD runs described in the section 'Simulation Details' as the initial configuration for the computation of k at the five different temperatures between 293 K and 373 K. For the sake of simplicity, we describe the procedure followed in case of the systems of pure PAO-2 solvent. The equilibrated and annealed pure solvent systems are further equilibrated for 1 ns under constant NVT conditions. The Nosé-Hoover thermostat is removed at this stage following which the heat flux as described by Müller-Plathe is implemented. The system is run for 2 ns under this condition where the centre of the box acts as the heat source and the box faces act as heat sinks. The entire box is divided into 20 layers along the z-direction and the momentum exchanges are applied at a frequency of every 200 time-steps across these layers (see Figure 2.9). The temperature gradient is monitored at every 1000 time-steps. After 2 ns, the exchanges generate a linear ∇T, whereafter the production run is carried out for 10 ns. The reported values of k for a typical run are an average of the final 5 ns of the production run. The values converge well within an accuracy of 10^{-5} W m^{-1} K^{-1} after the first 2 ns of production runs. An identical procedure is followed in case of polymer solution system as well. The computed k as a function of temperature is shown in Figure 2.9 for typical production runs for pure solvent at different temperatures.

Thermal conductivity of pure solvent decreases with temperature. This is in line with the behaviour of long-chain hydrocarbons in these conditions [216]. The drop in the thermal
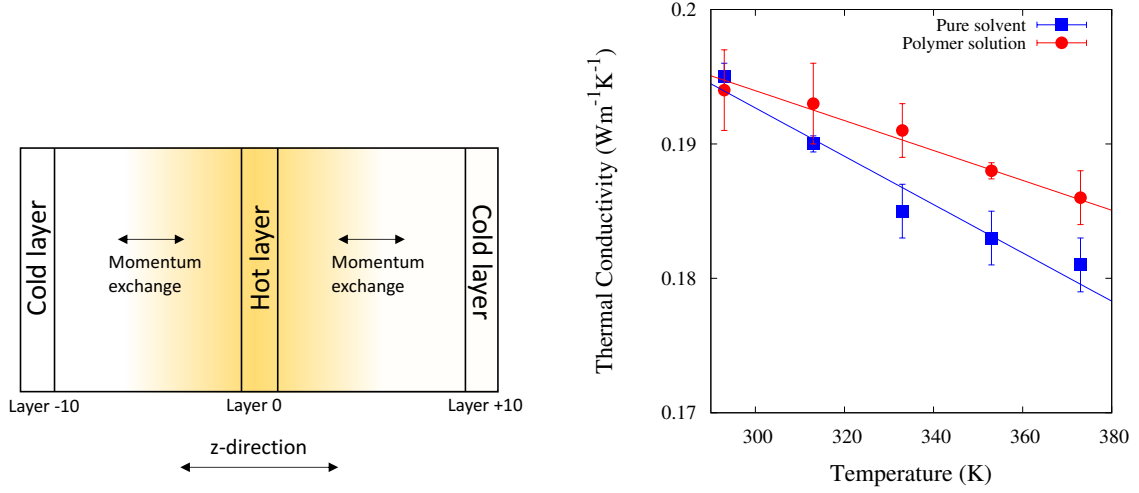
Figure 2.9: (Left) The schematic of reverse-NEMD applied in case of the present simulation study. (Right) The thermal conductivity (k) of the pure solvent and polymer solution as a function of temperature. The closed symbols show the simulated data and the lines show the linear function fits as described in Equation 2.21.

conductivity with increasing temperature is a consequence of the enhanced thermal motion of the atoms in the system [217]. This motion expands the liquid (signified by the decreasing density in Table 2.1) increasing the distance of immediate neighbours to transfer kinetic energy. The large error bars (standard deviation) in the computation are also observed in the experimental measurements of k of long chain hydrocarbons in liquid state as well [218]. The simulated data here is comparatively higher than the experimental data (0.137-0.132 W m^{-1} K^{-1}) reported elsewhere [219]. The data can be fitted using a linear function

$$k = k_0 - \left(\frac{\partial k}{\partial T}\right)_p T \tag{2.21}$$

where, k_0 is the thermal conductivity at absolute zero and $\left(\frac{\partial k}{\partial T}\right)_p$ is the temperature coefficient at the atmospheric pressure, $p = 1$ atm. The temperature coefficient for the pure solvent system from the fit in Equation 2.21 is $(1.8 \pm 0.03) \times 10^{-4}$ W m^{-1} K^{-2}.

Figure 2.9 also shows the variation of thermal conductivity in polymer solution as a function of temperature. The data shows that thermal conductivity of the solution is greater than that of the solvent at the various temperatures. The larger error bar at 293 K could be attributed to the insufficient time given for the system to evolve at very low temperatures and demands more sampling. Along with the enhancement in thermal conductivity at different temperatures compared to that of the solvent, fitting the data using Equation 2.21 also shows a lower

Table 2.4: Mean values of k$_{polymer}$ of polymer solution at various temperatures.

Temperature (K)	k$_{polymer}$ (W m^{-1} K^{-1})
293	-0.001
313	0.003
333	0.007
353	0.005
373	0.004

temperature coefficient, $\left(\dfrac{\partial k}{\partial T}\right)_{\mathrm{p}} = (1.1 \pm 0.01) \times 10^{-4}$ W m^{-1} K^{-2} in case of the solution. This means that the reduction in thermal conductivity of the solution as a function of increasing temperature is slower in case of the polymer solution compared to that of the pure solvent.

Curtiss and Byron Bird [220] proposed the theory that in case of dilute polymer solutions, the thermal conductivity is an additive function. In other words,

$$k_{solution} = k_{solvent} + k_{polymer} \tag{2.22}$$

where k$_{solvent}$ and k$_{polymer}$ are the thermal conductivities of the solvent and polymer, respectively. This theory is predicted for Fraenkel and Hookean dumbbell model of chain polymers. From Equation 2.22, we can obtain k$_{polymer}$ at different temperatures whose values are given in Table 2.4. Thermal conductivity enhancement in dilute polymer solutions is attributed to an increase in the contribution of the kinetic motion of the intra-molecular energy and the work done against the intra-molecular forces [221]. Also, k$_{polymer}$ is proportional to the chain stiffness. The contribution of k$_{polymer}$ Table 2.4 shows there are significant factors, in addition to chain stiffness helping in the thermal conductivity enhancement at different temperatures. Recent studies show the impact of monomer sequencing on the thermal conductivity of block polymers [222]. However, further studies are required to understand the effect of this in case of polymer solutions providing motivation for future works.

2.3.8 Advantages and limitations

The polymer addition leading to a weak non-Newtonian behaviour demonstrated in the past investigations of similar liquids [96] can have a measurable influence on vortex roll-up tendency in inertial flows. The MD study here is able to provide structural reasons for those observations that are difficult to be determined by experimental procedures. It establishes how the polymer addition to a synthetic oil changes the hydrodynamic radii of the solvent molecules. The impact of OCP as a thickening agent decreases with temperature as shown by the computation of Q_{VI}. The shear thinning effect is enhanced by the addition of polymer chain, that is correlated

to the molecular alignment in the solution as a function of shear rates. The chain flexibility is prominent in case of OCP as determined by its hydrodynamic radius in the solution at all temperatures. Liquids having similar shear thinning indices (0.4-0.7), obtained by the comparison of m from the Carreau-model fit with Power law fit for a Herschel-Bulkley fluid, can provide Nusselt numbers between 40-60 for Reynolds number = 100 in case of immersion cooling which is better than what is observed for Newtonian fluids such as water [223]. At the same time, it is a limitation of the atomistic MD study to determine the actual composition of the polymer chain in the solution that may have optimal heat transfer properties. Moreover, computation of relaxation times of larger molecular weight polymer chains is also difficult in case of atomistic MD. This is where mesoscale modelling can help, and the models can be parametrised using the thermodynamic properties, viscosity and thermal conductivity obtained from atomistic MD, making this work significant.

2.4 Conclusions

The addition of an OCP polymer chain in PAO-2 solvent enhances the rheological properties of the resulting solution in the relevant temperature range. It improves the viscosity of polymer solution by increasing the hydrodynamic radii of the solvent molecules, effectively acting as a thickener to the base oil. Subsequently, the role of molecular stretching and alignment in the shear thinning behaviour of the liquids has been observed. The shear responses of the solvent and the polymer solution show that the latter starts shear thinning at a lower shear rate than the former. The better shear thinning nature of the dilute polymer solution emerging from their structural properties can contribute to the evolution of coherent vortices, supporting their use in direct heat transfer applications. Simultaneously, the thermal conductivity of the solution is higher, and the decline in their values with rise in temperature is slower, compared to that of the base oil. This further justifies the use of mixtures made of OCP in PAO-2 as coolants. Even though the work signifies a viable direction in coolant research, the factors such as polymer composition needs to be determined based on the competing factors of thickening effect and shear thinning abilities. Such an analysis requires appropriate mesoscale studies that are part of our future works.

The analysis of the viscoelasticity of the polymer solution by the computation of the terminal relaxation time shows faster relaxation of the OCP chain with increasing temperature and shear rates. The storage and loss moduli of OCP polymer solution are higher than those of the pure solvent. The elastic nature of the OCP polymer increases the elastic instabilities of the polymer solution triggering coherent vortex formation. This in turn enhances the heat transfer process. Molecular dynamics guided design of dilute polymer mixtures that exhibit a

clear viscoelastic nature can help in optimising the rheological behaviour of the liquid media suitable for effective thermal management in confined spaces related to immersion cooling.

2.5   Critical review

This section contains a brief commentary of the literature post the publication of the article corresponding to this chapter.

Concurrent research on the computation methodology of the shear viscosity of polyalpha-olefins using MD by Mercier et al. [224] may provide a novel understanding of the polymer mixture rheology that is not discussed in this chapter. At the same time, a recent study of viscosity modifiers by Khajeh et al. [225] such as OCP and PMA using Brownian dynamics and Lattice Boltzmann techniques targets to establish the relationship between structural behaviour and flow hydrodynamics. The investigation explains the impact of non-dipole nature of OCP polymer chain to the bulk flow of the liquid solutions composed of it. Contrary to the oil studied in this chapter, natural ester and mineral oils are being probed for the dielectric immersion cooling of battery modules. However, that may require further investigation in terms of optimal operating conditions and suitable additives as carried out by Liu et al. [226]. Such optimisation studies to improve the thermal performance are observed for both static and forced convection of such coolants in BTMS via numerical and experimental methods [227].

Chapter 3

Multi-scale modelling

[1] A framework predicting the rheological (storage and loss moduli, first normal stress coefficient, and relaxation time) and transport (viscosity, diffusivity) properties of non-Newtonian dilute polymer solutions at mesoscales (e.g. $\sim$ns to μs) from the atomistic-scale molecular behaviour is presented. More specifically, the rheological behaviour differences of OCP and PMA polymer solutions in PAO-2 oil are simulated using both atomistic molecular dynamics (MD) and many-body dissipative particle dynamics (mDPD) within a temperature range of 313-373 K. The simulation methodology described is able to distinguish itself from the standard DPD model by accurately reproducing the shear-thinning with high sensitivity, as seen in the atomistic MD simulations at high shear rates (e.g. $10^8 - 10^{13}$ s^{-1}). It is shown that the model is well-suited to compute properties such as first normal stress differences and relaxation times that are difficult to estimate at atomistic scales due to the low signal-to-noise ratio. Moreover, the Schmidt numbers ($> 10^3$) are predicted with high accuracy when compared with the values from atomistic-scale simulations. The proposed model is able to predict relaxation times of dilute polymer mixtures that are difficult to be obtained using state-of-the-art rheometers. Finally, it is found that the terminal relaxation time of PMA polymer chain does not vary monotonically as a function of temperature, unlike in the case of OCP; this is significant for describing viscoelastic behaviour at macroscales where satisfactory constitutive equations are not available.

---

[1]A significant portion of this chapter is published as: B. Ravikumar, I. K. Karathanassis, T. Smith, M. Gavaises, "Multi-scale modelling of dilute viscoelastic liquids: Atomistic to mesoscale mapping of polymer solutions", *Polymer*, 285:126360, 2023 under the terms of Creative Commons Attribution 4.0 license (CC BY 4.0). The author of this dissertation has contributed to the methodology, validation, data curation, formal analysis, investigation, writing and visualisation of the article.

3.1 Introduction

Dilute viscoelastic liquids are expected to be used in applications such as direct cooling in electronic and automotive industries, and soft electronics manufacturing, among many other industrial and biomedical processes. These liquids are valued owing to their viscoelastic nature, dielectric nature and thermal stability [159, 143, 137, 228]. New combinations of polymers and solvents are required to design novel viscoelastic dilute polymer solutions [229, 230]. In this work, we focus our investigation to the dilute polymer solutions relevant to heat transfer applications. Given the technical challenges associated with experimental methods in the dilute polymer regime [102, 231], and the requirement of satisfactory constitutive equations to model such liquids in continuum scale simulations, an alternative approach for modelling such liquids is required [232].

The fluid chemistry influences its thermodynamic (e.g. density), morphological and transport (e.g., diffusion coefficient) properties, and those can be modelled via atomistic molecular dynamics simulations (MD). United-atom models are utilised to understand the Rouse to reptation cross-over behaviour of short-chain concentrated polymer solutions, their steady-state shear and elongational flow behaviour [233–236]. Still, macroscopic properties such as deformation response, storage and loss moduli, and relaxation times of many such liquids are challenging to be obtained using a full-atomistic MD or united-atom MD, given the expensive computational schemes for long-chain polymer solutions and low signal-to-noise ratio [237, 238]. Therefore, a mesoscale modelling routine is required to bridge the gap between the microscale behaviour and macroscopic observations [239].

An extensive body of work over the past three decades in the relevant literature is dedicated to mesoscale modelling via the Lagrangian mechanics [240–246]. Polymer melts and their entanglement characteristics are studied along with their relaxation modes using Kremer-Grest models [32, 247]. Concurrently, the widely applied methodology is dissipative molecular dynamics (DPD) developed by Groot and Warren [123]. DPD uses a Langevin form of equation where the repulsive, dissipative and random forces lead to the description of the system of interest. Several works in the field have concentrated on predicting rheological and interfacial properties of aqueous solutions with dispersed macromolecules [248, 249, 242]. As a response to anomalies in behaviour under anisotropic forces, vapour-liquid coexistence, and to assimilate heat transfer characteristics, DPD models have been modified to develop many-body DPD (mDPD) [250, 251], energy-conserving DPD (eDPD) [252] and so on. However, a modelling scheme to reproduce viscoelastic behaviour among a wide range of liquids is still being developed.

The standard DPD model is shown to provide misleading results for viscosity (e.g. shear thickening) in the case of non-equilibrium DPD simulations of simple fluids with spherical

particles [253]. This is in addition to the fact that conventional DPD underestimates Schmidt numbers by three orders of magnitude [251]. Several suggestions extending from Lees-Edwards boundary condition modifications to thermostat modifications have been prescribed in the literature to overcome this [254–258]. The motivation for schemes to improve the prediction of non-Newtonian behaviour is seen even recently. For example, Zhao et al.[259] tried to use Gaussian process regression (GPR) based active learning to connect bulk rheology to microstructure dynamics as a way to reproduce experimental shear-thinning of viscoelastic liquids. Recent efforts are engaged in parametrising the mDPD models to reproduce non-Newtonian behaviour in fluids. Zhao et al. [260] showcased the computation of surface tension and first normal stress difference of polymer solutions. Jamali et al. [261] proposed a methodology to relate the compressibility of the fluid with the Flory-Huggins theory to take into consideration the mixing effects of different components to generalise the modelling approach. At the same time, a modelling strategy to consistently map all the relevant properties into real units with accurate scaling is vital, and there is a scope for a consistent approach to be introduced [257, 124]. Moreover, the chemical structure of the organic molecules which influences the order of magnitude of Schmidt numbers needs to be included in the scaling-up process as well.

The investigation here demonstrates the simulation of polyalphaolefin (PAO-2) oil and polymer solutions of two different polymer chains, namely, olefin co-polymer (OCP) and polydodecylemethacrylate (PMA) in PAO-2. The specified oil and polymer compounds are extensively used in industrial applications such as lubrication, and are proposed as candidates for cooling technologies [161, 162, 165, 262, 263]. The radius of gyration of OCP and PMA polymer chains varies differently in PAO-2 as a function of temperature [168, 166]. These structural differences lead to differences in their rheological behaviour, as shown in the literature [96]. The mapping of the chemistries of the different polymer chains in the oil appropriately to mesoscale shows the ability of the simulation methodology to be a tool for simulating any such liquids. The study models realistic Schmidt numbers ($> 10^3$) in mesoscale as seen for such liquids in experiments [264]. The Schmidt number matching is essential to capture the correct hydrodynamic interactions of the liquid [265]. The polymer chains are distinguished by inducting an angular cosine potential into the mDPD model, whose parameters vary with the chemistry and temperature to qualitatively model the radius of gyration. The simulated mesoscale polymer solution is able to behave as described by Zimm's model [112] and is able to show diluteness.

The simulation carried out here is able to showcase the variation in mildly viscoelastic non-Newtonian liquids with shear via non-equilibrium mDPD. Moreover, the zero shear viscosity obtained via non-equilibrium mDPD agrees with equilibrium mDPD computations, validating

the process. Additionally, properties such as first normal stress coefficient, storage and loss moduli, and relaxation times which influence fluid behaviour in continuum scales are computed. Therefore, the detailed description of the methodology provides a novel tool that can be extended to the simulation of any non-Newtonian polymer liquids with minimal tuning of the scaling units and mDPD model parametrisation.

3.2 Design of simulation

3.2.1 Solvent modelling

The simulation is designed in such a manner so as to map the important system parameters such as the characteristic length, mass and time for the temperature range of interest from atomistic MD to mDPD. Here, the solvent PAO-2 being investigated is an oil that has high Schmidt numbers (Sc) of the order of $10^3 - 10^4$. The goal is to find the appropriate mDPD parameter-set such that they reproduce Sc (as computed by Equation 3.13). This ensures that the relative motion of the particles due to momentum transport and mass transport manifest in the same manner at the larger length- and time-scales. At the same time, it must be ensured that the Sc is derived at the same thermodynamic conditions such as temperature and pressure (consistent with unit mapping) as obtained at the atomistic scale simulations. The fundamentals of the mDPD modelling are described in Appendix B. To provide maximum control on the modelling of the polymer solutions of interest, the work involves the tuning of five parameters, namely ρ, A_{ij}, B_{ij}, γ_{ij} and r_D (see Equations B1 to B7).

A simulation framework is shown in Figure 3.1 for the mDPD simulation at temperature, $T^* = 313$ K and pressure, $p^* = 1$ atm with '*' from here on indicating quantities whose values are in real units. PAO-2 molecule has a molecular weight (M_w^*) of 282 g mol^{-1}. By considering the density of PAO-2 at the temperature of 313 K obtained from atomistic MD ($\rho^* = 780$ kg m^{-3}), we compute the molecular volume as 600.34 Å^3. The simulation procedure starts with a number density, $\rho > 6$ and local density-dependent conservative force cut-off, $r_d = 0.75$ and a timestep, $dt = 0.01$. The reduced density range is in agreement with the description in the literature [125, 260]. The equation of state for an mDPD fluid has been approximated as follows:

$$p = \rho k_B T + \alpha A_{ii}\rho^2 + 2\alpha B_{ii}r_d^4(\rho^3 - c\rho^2 + d) \tag{3.1}$$

where $\alpha = 0.101$, c = 4.16 and d = 19 for an organic fluid of the nature of PAO-2 [251, 125]. This simplifies the problem of mDPD model parametrisation to two parameters, namely A_{ii} and B_{ii}. To find their exact solutions, another equation is required. By differentiating the Equation 3.1, we can relate the reduced units isothermal compressibility, κ to these parameters

Table 3.1: The properties of the PAO-2 system in reduced units (mDPD units) and corresponding values in physical units at 313 K. (Note: N_a is the Avogadro number)

Property	mDPD units	Real units
Density (ρ)	7.9	$\rho^* = \dfrac{\rho N_m M_w^*}{N_a r_C^{*3}} = 780 \text{ kg m}^{-3}$
m_b	1.0	$m_b^* = \dfrac{N_m M_w^*}{N_a} = 4.683 \times 10^{-25} \text{ kg}$
r_C	1.0	$r_C^* = \left(\dfrac{\rho m_b^*}{\rho^*}\right)^{\frac{1}{3}} = 16.8 \text{ Å}$
Energy, E ($k_B T$)	1.0	$E^* = k_B^* T^* = 4.319 \times 10^{-21} \text{ J}$
dt	0.01	$dt^* = 0.01 r_C^* \left(\dfrac{m_b^*}{E^*}\right)^{\frac{1}{2}} = 0.17 \text{ ps}$
Pressure (p)	0.111	$p^* = \dfrac{p E^*}{r_C^{*3}} = 1 \text{ atm}$

such that

$$\frac{1}{k_B T}\left(\frac{\partial p}{\partial \rho}\right)_T = \kappa^{-1} = 1 + \frac{2\alpha A_{ii}\rho}{k_B T} + \frac{2\alpha B_{ii} r_4^d}{k_B T}(3\rho^2 - 2c\rho). \tag{3.2}$$

The isothermal compressibility of the solvent from the atomistic MD (κ^*) is used in this equation, calculated from the relation

$$\kappa^{-1} = \frac{M_w^* N_m}{R T^* \rho^* \kappa^*}. \tag{3.3}$$

Here, $N_m = 1$ is the number of molecules of PAO-2 solvent being represented by a single mDPD bead and R is the universal gas constant. The κ^* values agree with the experimental results available in the literature [263].

The initial values of ρ and r_d are used to solve the above equations to obtain A_{ii} and B_{ii}. The solvent system with these A_{ii} and B_{ii} is simulated. Since Equation 3.1 is an approximated equation of state, the value of B_{ii} is optimised such that the virial pressure simulated oscillates around the pressure as computed in Table 3.1. The mDPD scaling units for the rest of the temperatures are provided in Appendix B from Table B9 to B11. Following this, simulations are carried out for maximum stable values of dissipative force parameters at this dt, $\gamma_{max} = 18.0$ and $r_{D,max} = 2.0$. If the $Sc_{mDPD} < Sc_{atomistic}$, ρ is increased and the above steps are repeated. If $Sc_{mDPD} > Sc_{atomistic}$, γ_{ij} and r_D are optimised till $Sc_{mDPD} = Sc_{atomistic}$. Figure 3.2 shows the typical size difference between the simulation boxes described in this study, with the mesoscale box ensuring a larger ensemble-averaging of properties.
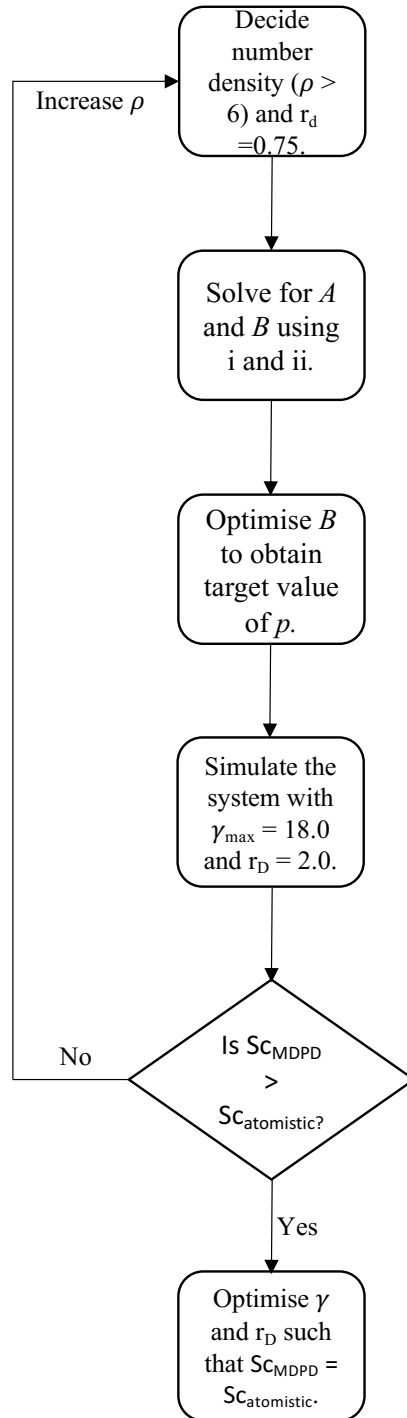
i) $\quad p = \rho k_B T + \alpha A \rho^2 + 2\alpha B r_d^4 (\rho^3 - c\rho^2 + d)$

ii) $\quad \dfrac{1}{k_B T} \left(\dfrac{\partial p}{\partial \rho} \right)_T = \kappa^{-1} = 1 + \dfrac{2\alpha A \rho}{k_B T} + \dfrac{2\alpha B r_4^d}{k_B T}(3\rho^2 - 2c\rho)$

60

Figure 3.1: Schematic of the modelling workflow of the solvent for mDPD simulations.
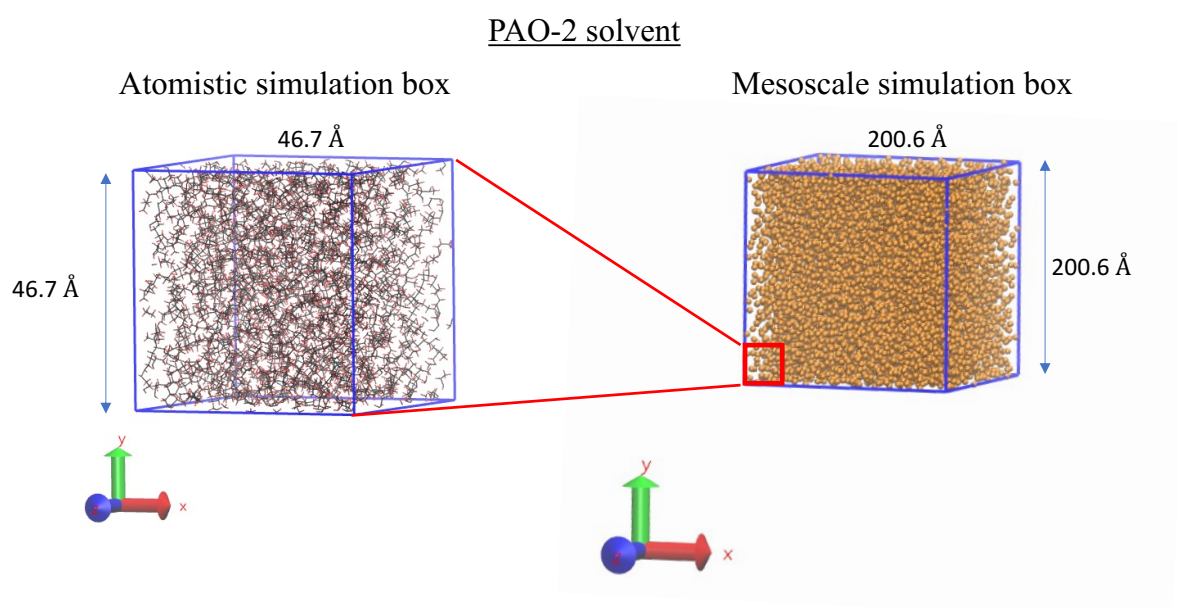
Figure 3.2: Representative simulation boxes of PAO-2 solvent in the atomistic scale consisting of 170 molecules and in the mesoscale consisting of 10980 molecules at 313 K.

3.2.2 Polymer modelling

Two different polymer chemistries are simulated in this work, namely an olefin copolymer (OCP) composed of ethylene and propylene monomers, and poly dodecylmethacrylate (PMA) that has a branched structure at the atomistic scale with a carboxylate function group. In the case of OCP, the monomer consists of short alkene molecules that make it chemically similar to the PAO-2 solvent molecules. Therefore, in mDPD simulation, the solvent-polymer bead interactions can be treated as similar to that of solvent-solvent bead interactions. In other words, $A_{ij} = A_{ii}$ and $B_{ij} = B_{ii}$. This leads to the treatment of PAO-2 oil as a theta solvent in case of the OCP polymer in the mDPD simulations. In a theta solvent, the repulsive and attractive interactions between the monomer beads of a polymer chain are balanced [266]. The bonded interactions of the polymer chain are derived from FENE potential, and angle stiffness is provided by a cosine force-field (see Equations B8 to B11). The parameters for the simulation of OCP solution are shown in Table 3.2. Since OCP is composed of two types of monomers, i.e., ethylene and propylene, the differentiation of those has been reflected in the use of $k_{angle,1}$ and $k_{angle,2}$, respectively. After obtaining the initial values from Everaers et al. [121], the final values of the two parameters are optimised so as to agree with the radius of gyration (R_g) values computed from the atomistic scale MD.

On the other hand, PMA has a different monomer structure and therefore, the polymer-solvent bead interactions must consider the mixing effects. In mesoscale simulations, such effects are modelled by considering the Flory-Huggins theory [267]. Under this theory, the magnitude of the attractive interaction parameters in the conservative force in Equation B2 are computed as

$$|A_{ij}| = |A_{ii}| + \frac{\chi_{ij} k_B T}{2\alpha(\rho_A + \rho_B)} \tag{3.4}$$

where χ_{ij} is called the Flory-Huggins interaction parameter that is defined as

$$\chi_{ij} = \frac{V}{k_B T}\left(\delta_i - \delta_j\right)^2 \tag{3.5}$$

where V is the volume of the simulation box. Here, δ_i is computed using the cohesive energy density (CED) of a species i from their non-bonded energies obtained from the relationship

$$\delta_i = \text{CED}^{\frac{1}{2}} = \left(\frac{\sum_{i=1}^{k} E_{nb}^{iso} - \langle E_{nb}^{k} \rangle}{k}\right)^{\frac{1}{2}}. \tag{3.6}$$

Table 3.2: Various parameters of mDPD simulations at 313 K in reduced units (mDPD units).

Parameters	OCP solution	PMA solution
A_{ii}	-108.0	-108.0
A_{ij}	-108.0	-108.1
B_{ii}	43.5	43.5
B_{ij}	43.5	43.5
γ_{ij}	18.0	18.0
r_D	1.84	1.84
k_f	30.0	30.0
r_0	1.5	1.5
$k_{angle,1}$	2.15	-
$k_{angle,2}$	0.70	-
k_{angle}	-	0.86

Here, $\left\langle E_{nb}^k \right\rangle$ is the ensemble average of the non-bonded energies of k molecules of species i and $\sum_{i=1}^{k} E_{nb}^{iso}$ is the sum of non-bonded energies of k individual molecules in an isolated simulation box of species i. From the atomistic scale simulations, the total pairwise interaction energies using a simulation box of pure PAO-2 or PMA are used to compute $\left\langle E_{nb}^k \right\rangle$. Similarly, the E_{nb}^{iso} is computed using the total pairwise interaction energies in the same simulation box retaining a single molecule of PAO-2 or PMA. The parameters obtained are shown in Table 3.2 for the mDPD simulation of the PMA polymer solution at 313 K. A similar exercise in case of OCP polymer chain shows that $\delta_i = \delta_j$, confirming the hypothesis to treat the OCP polymer solution as a theta solution. The parameters for the rest of the temperatures are shown in Appendix B (see Tables B6 to B8). At the same time, the modelling of the polymer chain used in the study is complete only with the correct parameters of angle stiffness, k_{angle}. It is tuned to reproduce the variation of R_g as a function of temperature.

3.2.3 Simulation details

The time-integration of the mDPD equations is done using a modified velocity Verlet algorithm using the λ parameter of 0.5 [123]. A typical periodic simulation box consists of 10989 solvent beads. The ρ equal to 7.9 obtained at 313 K is used for the modelling and simulation of the mDPD system at other temperatures. Polymer chains of different lengths between 11 to 77 beads are simulated. The upper limit of the chain length simulated here ensures that the radius of gyration is less than or equal to half of the simulation box length ≈ 11.94 mDPD units, thereby preventing any artefacts. The computation of equilibrium properties and rheological analysis of polymer solutions have been reported for a single OCP or PMA chain of a length of 11 beads representing a molar mass of 3102 g mol^{-1} and a concentration of ~ 1000 ppm (0.1%)

by weight. Additionally, an OCP polymer solution corresponding to a similar concentration in atomistic simulation of 5.9% by weight (= 203 polymer chains) is also simulated for the sake of validation.

The reported results are from five independent simulations of 10^7 timesteps or 1.7 μs in real units (see Table 3.1). The non-equilibrium simulation is carried out by box deformation with equations of motion expressed in SLLOD form [197], making it conceptually equivalent to Lees-Edwards periodic boundary conditions [268]. The simulated solvent systems are compared to the results obtained from the simulations of original DPD model using parameters described by Groot and Warren [123] at $\rho = 3$ and $\rho = 7.9$. The former ρ value is used in the original DPD model, whereas the latter is used to compare with the mesoscale simulations carried out in this study.

The atomistic MD simulation details including the force-field parameters (Table B1 to B5, and Figure B1) are provided in Appendix B. In brief, the simulations are done using a box consisting of 170 PAO-2 solvent molecules in which a single polymer chain is dispersed. The simulation uses OPLS-AA force field to account for the polymer and solvent interactions. The mesoscale and atomistic simulations are done using the LAMMPS software with source-code modified in-house to implement the mDPD modelling scheme.

3.3 Results and discussion

The atomistic scale modelling of the viscoelastic liquids shows unique behaviour for each polymer solution when computing the radius of gyration as a function of temperature. The mDPD models aim to reproduce these fundamental features such that they can be used to derive different rheological properties at higher scales. In this respect, we initially validate the mDPD model to represent the diluteness of the polymer solution, following which the hydrodynamic radii variation with respect to the temperatures is compared between atomistic and mDPD simulations. It is followed by the computation of equilibrium properties showing the Schmidt number comparison at various temperatures. The analysis is concluded with the computation of the rheological properties of the two different polymer solutions to showcase the similarities and differences in their viscoelastic nature.

3.3.1 Validation of diluteness of polymer solution

If a model is expected to replicate a dilute polymer solution, it has to generally agree with Zimm's polymer theory [112]. In essence, it establishes that the polymer chains in the solution do not interact with each other leading to entanglements. In turn, the morphology and rheology

exhibited by the polymer chains are functions of their chain lengths. For example, the theory states that in a dilute solution with a theta solvent,

$$
\begin{aligned}
\mathrm{R}_g &\propto (N-1)^\nu \\
D_{poly} &\propto N^{-\nu}
\end{aligned}
\tag{3.7}
$$

where R_g is the radius of gyration of the polymer chain (as computed by Equation 3.11), D_{poly} is the self-diffusion coefficient of the polymer chain in the solution, N is the number of monomer beads and ν is the so called Flory exponent ≈ 0.53. The methodologies to compute the two quantities are described in later sections. In this work, the OCP polymer in PAO-2 acts as a theta solution. As shown in Figure 3.3, R_g increases as a function of $N-1$ and D_{poly} decreases as a function of N. The green curves show equations as per Zimm's model in Equation 3.7. The data points fit well with the curve indicating the dilute state of the polymer solution. Additionally, the computation of the mean-squared displacement of the central monomer of the polymer chain ($g_1(t)$)[269] has the following power-law sequence as a function of time

$$
g_1(t) \propto \begin{cases} t^1, t < \tau_0 \\ t^{0.67}, \tau_0 \leqslant t < \tau_Z \\ t^1, t \geqslant \tau_Z. \end{cases}
\tag{3.8}
$$

Figure 3.3c shows the three distinct temporal regimes of $g_1(t)$ for the different polymer chain lengths, agreeing with the Zimm's theory [270]. The obtained values of τ_Z for different chain lengths agree with the relationship $\tau_Z \propto N^{3\nu}$. However, increasing N beyond 33 leads to deviation from the Zimm relationships of D_{poly} and τ_Z, indicating the role of the local stiffness of the chain in sustaining the intermediate regime longer than expected, as described by Hinczewski et al. [271].

In addition to Zimm's relationship, the primary characteristic to verify if a mesoscale fluid acts as a dilute mixture is to establish the ability of solvent molecules to provide effective hydrodynamic interactions to screen the different monomer beads of the polymer [272]. To verify if the model reported here is able to provide the required hydrodynamic screening, the computation of the variable

$$
h^* = \sqrt{\frac{3}{\pi}} \frac{\mathrm{r}_H}{b}
\tag{3.9}
$$

(a)

(b)

(c)

(d)
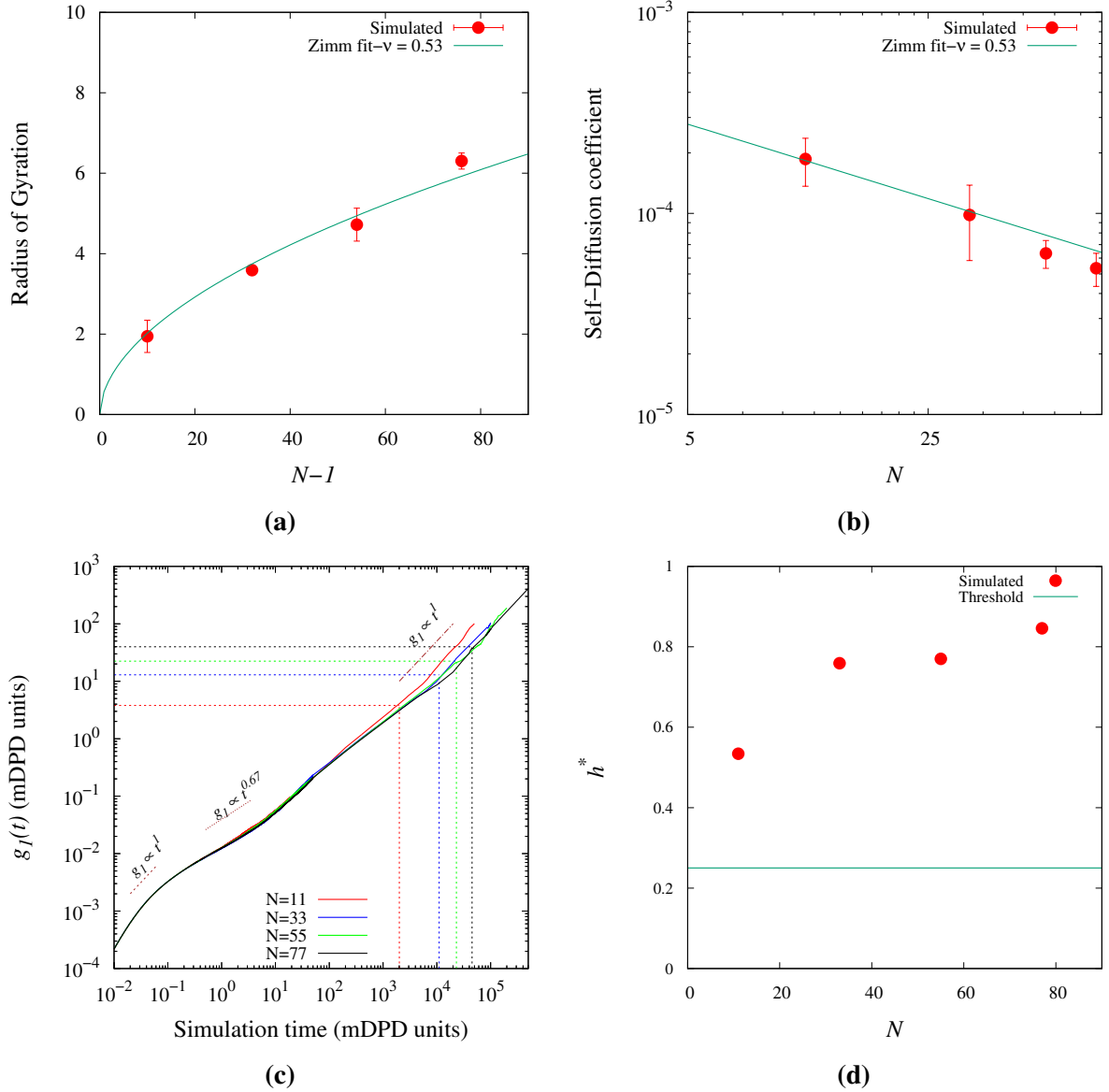
Figure 3.3: (a) Radius of gyration of OCP polymer chain as a function of chain length, $N-1$ at $T = 313$ K. (b) The self-diffusion coefficient of the OCP polymer chain as a function of chain length, N at $T = 313$ K. (c) $g_1(t)$ as a function of time showcasing different regimes for different chain lengths. Here, the horizontal dashed lines show the value of R_g^2 and the vertical dashed lines show the corresponding values of τ_Z for different values of N. (d) h^* as a function of chain length, N at a temperature, $T = 313$ K.

is done, where b is the average bond length of the polymer chain and r_H is the hydrodynamic radius of the polymer bead computed from the Stoke-Einstein relationship

$$r_H = \frac{k_B T}{6\pi\eta_{solution}D_{monomer}}.$$ (3.10)

Here, $D_{monomer}$ is the self-diffusion coefficient of the polymer bead [273]. As mentioned in the literature, the value of h^* should be $>= 0.25$ to consider the simulated system as a dilute solution. From Figure 3.3d, it is seen that h^* value is above 0.25 at all simulated conditions for the model with the values increasing from 0.53 to 1.017 with increase in the OCP polymer chain length at 313 K.

3.3.2   Structural characteristics

The basic structural characteristic of a polymer chain in a solution is its hydrodynamic radius defined as

$$R_g = \sqrt{\frac{1}{M}\sum_{i=1}^{n}m_i(\mathbf{r}_i - \mathbf{r}_{\text{com}})^2}$$ (3.11)

where M is the mass of a molecule, m_i is the mass and $\mathbf{r}_i$ is the position vector of an atom/bead i of a molecule consisting of n atoms/beads, and $\mathbf{r}_{\text{com}}$ is the centre of mass of a molecule. Therefore, we require the polymer behaviour at mesoscale to match the one shown at atomistic scale MD as a function of temperature.

As observed in Figure 3.4, the radius of gyration of OCP in PAO-2 does not vary as a function of temperature at atomistic scale. The comparison of the end-to-end chain length distribution of OCP (see Figure B4) shows a similar mean value in both the scales, even though the distribution is broader in the mesoscale. This can be attributed to the longer runtime in the mesoscale ensuring the chain relaxation to be complete. On the other hand, the R_g of PMA polymer chain in PAO-2 increases as a function of temperature. The viscosity index and shear response of the solutions have been demonstrated to be influenced by the variation of R_g as a function of temperature [274, 275]. The PMA polymer chain is reported to be a better viscosity index improver (VII) than OCP in olefin oils because of how its R_g increases as a function of temperature. Hence, the mDPD model here is expected to reproduce the same trend as in the case of the atomistic MD.

The behaviour of the atomistic MD is replicated in the mDPD model by tuning the angle stiffness energy, k_{angle} at every temperature. k_{angle} limits the movements of the bonded string of beads. As OCP chain is shown to have a constant R_g with temperature, the k_{angle} is given the same values at all temperatures of the mDPD model. The values of R_g oscillate around a mean of 1.90 in mDPD units with an increase in temperature. On the other hand, as the PMA chain

(a)

(b)
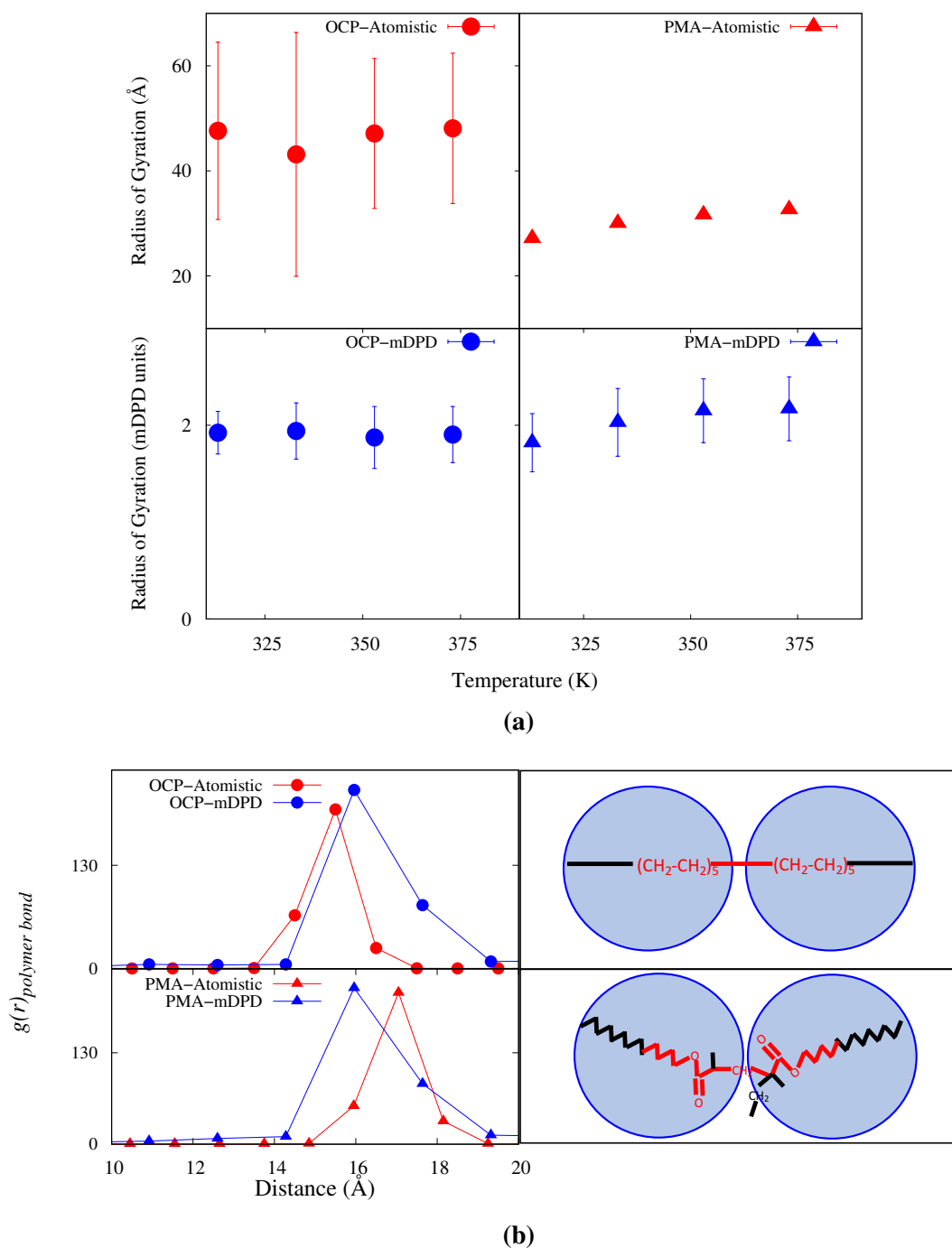
Figure 3.4: (a) Radius of gyration as a function of temperature, *T* for OCP and PMA solutions in atomistic and mDPD simulations. (b) Intramolecular bond distribution of OCP and PMA polymer chains at 313 K in the atomistic and mDPD simulations. The schematic here compares the equivalent bonded distance of the beads in mesoscale with that in atomistic scale.

increases its R_g values with temperature, the k_{angle} values are tuned to reproduce the behaviour (see Figure B5 in Appendix B). For that, the R_g value of mDPD simulation at 313 K is treated as the benchmark, and the k_{angle} is increased at every temperature such that the ratio of R_g at the simulated temperature and 313 K is the same for atomistic MD and mDPD. As shown in Figure 3.4a, this procedure is shown to increase the R_g as a function of different temperatures of the mDPD simulation of PMA polymer in PAO-2 with the mean values increasing from 1.83 at 313 K to 2.17 at 373 K.

While ensuring the R_g mapping, the intramolecular bond distribution of the polymer chain is verified by computing the pair distribution function

$$g(r)_{polymer\,bond} = \frac{n(r)}{4\pi\rho_{bead}\,r^2 dr}.$$

(3.12)

For comparison, the bond distribution in the atomistic scale is computed from the sum of all the distances between the bonded atoms of the same monomeric mass as the mDPD bead (see Figure 3.4b). The distances between the OCP monomer beads are close to 16 Å with the difference of the peaks in the two scales being approximately equal to 1 Å. Similarly, PMA monomer beads are found at a similar distance, with the mDPD scale having beads closer than the equivalent bonded distance between atoms at the atomistic scale. Further comparison of the dihedral distribution function [276] of the polymer chains in both the scales is shown in Figure B6 in Appendix B. It shows that the specific peaks of the distribution plateaus with increase in coarse-graining. The decrease in specificity of the peaks of intramolecular features in the implemented modelling scheme has been attributed to the insufficient accounting of entropy in recent literature [277, 278]. An attempt to match these structural distributions for smaller segments of alkanes is done by Reith et al [279]. The radial distribution function ($g(r)_{solvent-polymer}$) between solvent and polymer beads is shown in Figure B7. The impact of the structural differences of $g(r)_{solvent-polymer}$ in atomistic and mesoscale modelling on the dynamics is looked into in a later section.

3.3.3 Equilibrium properties

The motion of particles in a fluid occurs simultaneously due to the momentum transport as well as molecular diffusive motion due to thermal fluctuations. Schmidt number that compares the two kinds of motion is computed as

$$Sc = \frac{\text{Momentum diffusivity}}{\text{Mass diffusivity}} = \frac{\nu}{D}$$

(3.13)

where ν is the kinematic viscosity and D is the self-diffusion coefficient. Here, the momentum diffusivity (ν) values at zero shear rate are calculated from the dynamic viscosity (η_0) computed via the Green-Kubo formulation [188]. At the same time, the mass diffusivity (D) values are computed via Einstein's relation [16]. In accordance with this modelling approach, the Schmidt number has to match at both the atomistic and mesoscale levels. Sc values in the atomistic scale MD match well with with experiments reported in the literature [263].
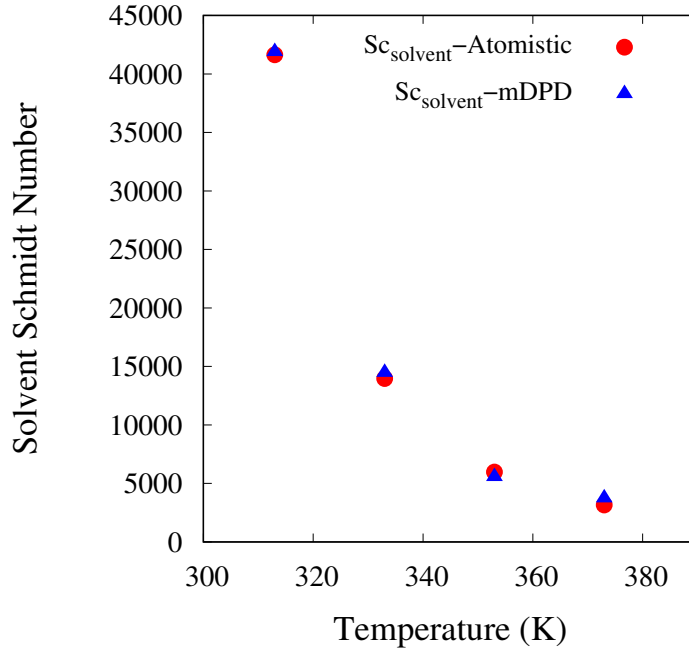
Figure 3.5: Schmidt number of solvent, $Sc_{solvent}$ as a function of temperature, T.

Figure 3.5 shows the comparison of the PAO-2 solvent Schmidt numbers ($Sc_{solvent}$) in atomistic and mDPD simulations at different temperatures under equilibrium conditions. The $Sc_{solvent}$ value decreases as a function of temperature. As seen, the $Sc_{solvent} \approx 40000$ at 313 K, before it undergoes a drastic reduction in magnitude with increasing temperature leading to a value ≈ 3000 at 373 K. After carrying out the mDPD modelling following the steps described in Section IV A, the Sc values in the mesoscale simulation agree with that of the atomistic MD at all temperatures, thereby validating the solvent physics.

The relative motion of the OCP polymer chain with respect to the solvent motion is measured by the computation of

$$Sc_{poly} = \frac{\eta_{0,solution} - \eta_{0,solvent}}{\rho D_{poly}}. \tag{3.14}$$

Here, Sc_{poly} is the Schmidt number of the polymer chain with $\eta_{solution}$ and $\eta_{0,solvent}$ representing dynamic viscosity of polymer solution and pure solvent at zero shear rate, respectively. Figure 3.6 shows the Sc_{poly} as a function of temperature. As seen in Figure 3.6a, Sc_{poly} values for atomistic MD are higher than the Sc_{poly} values obtained in the case of mDPD. Sc_{poly} decreases from 30000 at 313 K to 5100 at 373 K in the atomistic MD, whereas it decreases from 26800 to 867 for the same temperature range in mDPD simulation. In order to verify the veracity of the model, mDPD simulation at the exact polymer concentration of 5.9% by weight as in the case of atomistic MD simulation is carried out. Consequently, Figure 3.6b shows that Sc_{poly} values are in good agreement expressing unit consistency of polymer concentrations in atomistic and mesoscale models.
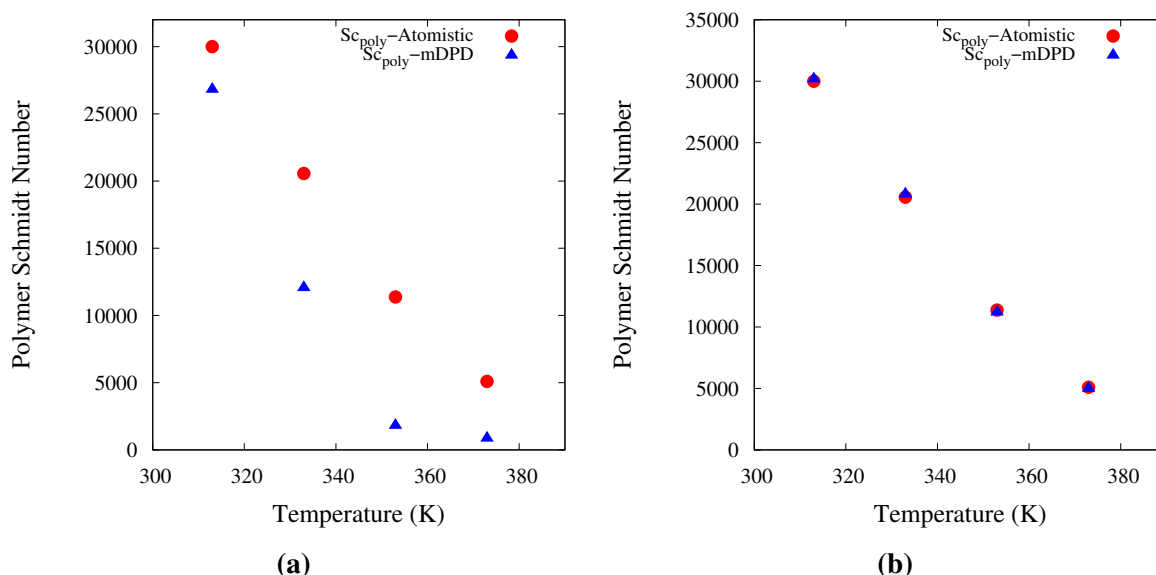
Figure 3.6: Comparison of OCP polymer Schmidt number (Sc_{poly}) as a function of temperature: (a) Different concentrations simulated in atomistic MD (5.9% by weight) and mDPD (0.001% by weight). (b) Same concentration simulated in atomistic MD and mDPD (5.9% by weight).

3.3.4 Rheology

For a model in the Lagrangian framework to be used for compounds with flow properties different from Newtonian fluids, the rheological behaviour must be reproduced in scales relevant to continuum mechanics. For different polymer chemistries, the dilute solutions have different rheological behaviour at the atomistic scale with respect to the changes in viscosity as a function of shear rate (i.e., shear-thinning) at different temperatures. However, it is essential to see if the shear-thinning behaviour itself is replicated while using the mesoscale models as

well or not. Moreover, having an accurate mesoscale model helps in deriving properties that are not possible to be computed at the atomistic scale due to low signal-to-noise ratio and slow dynamics.

The solvent and the two different polymer solutions undergo a Couette flow simulation. The flow is simulated by deforming the periodic box in the y-direction and the velocity gradient is computed in the z-direction of the simulation box. The $\eta(\dot{\gamma})$ as a function of shear rate ($\dot{\gamma}$) is computed from the relationship

$$\eta(\dot{\gamma}) = -\frac{\sigma_{yz}}{\dot{\gamma}} \tag{3.15}$$

where σ_{yz} is the off-diagonal component of the stress-tensor. In the atomistic scale, it is clearly seen that the solvent and polymer solution shear-thins at very high shear rates (refer to Figure 3.7). A distinct behaviour with respect to shear-thinning is observed in case of OCP and PMA in their respective solutions at different temperatures by fitting a Carreau-model of the form

$$\eta(\dot{\gamma}) = \frac{\eta_0}{(1+(\tau_s\dot{\gamma})^2)^m}, \tag{3.16}$$

where η_0 is the Newtonian viscosity that is obtained from the extrapolation of the data to $\dot{\gamma} = 0$, τ_s indicates the time constant related to shear-thinning and m is the strain-rate sensitivity coefficient.

The PMA solution starts shear-thinning at a lower shear rate ($\tau_s = 2.07$ ns) than the OCP solution ($\tau_s = 0.73$ ns) at 313 K. Similarly, at a higher temperature of 373 K, the shear-thinning behaviour is observed at lower shear rates for PMA ($\tau_s = 0.80$ ns) than what is observed in case of the pure solvent ($\tau_s = 0.10$ ns) and OCP polymer solution ($\tau_s = 0.14$ ns). At the same time, the mechanism of shear-thinning enhancement in case of PMA and OCP solution is different. While the OCP polymer chain leads to an increase in the hydrodynamic radius of PAO-2 on average, the presence of PMA does not impact the overall radius of PAO-2 molecules (see Figure B2 in Appendix B). The enhanced shear-thinning by PMA can be attributed to ease of shear-direction alignment of branched PMA polymer compared to the linear OCP polymer.

It is essential to reproduce the shear-thinning behaviour at such high shear rates for these mildly viscoelastic liquids via mesoscale model while proposing a universal methodology that can be extended to strongly viscoelastic medium as well. An oligomer solvent itself, such as the one used in this work, can show shear-thinning better than solvents such as water. This is attributed to the chains aligning in the direction of deformation [263]. Figure 3.8 shows the dynamic viscosity (η) of the PAO-2 solvent and DPD solvent as a function of shear rate ($0.001 \leq \dot{\gamma} \leq 1.0$ in mDPD units). The DPD solvents show no viscosity variation with the imposed shear rate and follow more of a Newtonian character within the range, as observed in literature [280]. This is attributed to the inherent nature of the DPD equations
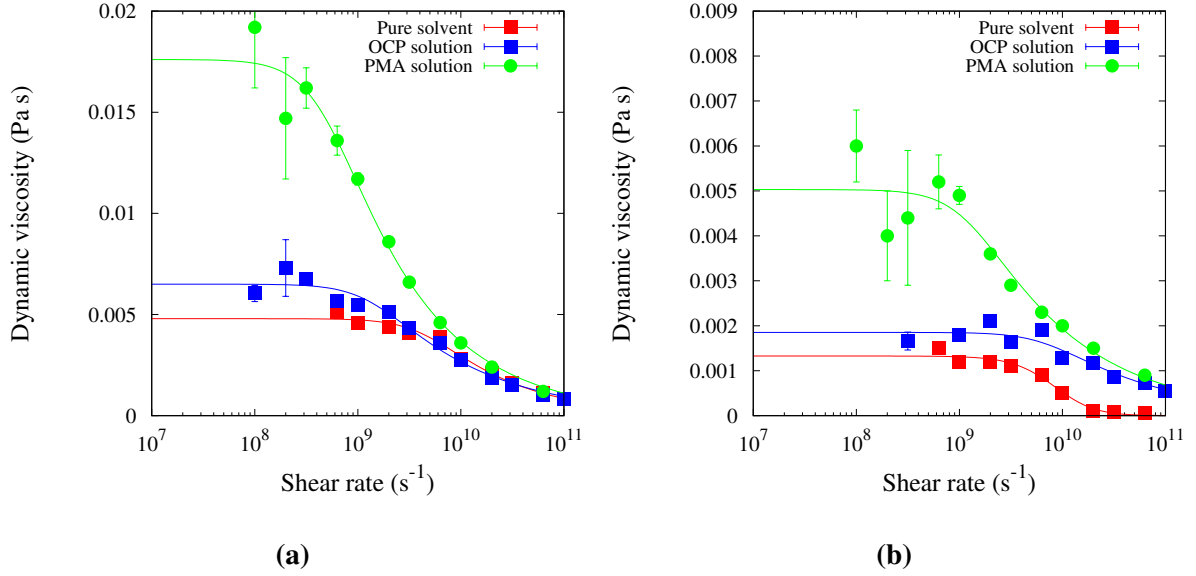
Figure 3.7: Viscosity ($\eta(\dot{\gamma})$) as a function of shear rate ($\dot{\gamma}$) at (a) 313 K and (b) 373 K for pure solvent and polymer solution systems simulated via atomistic MD. The symbols with the error bars show the simulated dynamic viscosity values, $\eta(\dot{\gamma})$ at different shear rates, $\dot{\gamma}$. The lines depict the Carreau-model fittings.

that cannot capture a significant dependence of η with $\dot{\gamma}$ [281]. However, the PAO-2 solvent in this work is able to reproduce the shear-thinning behaviour as seen in the atomistic scale. Oils or hydrocarbons can shear-thin at shear rates well below those solvents represented by conventional DPD. Additionally, the model clearly shows that with NEMD, the zero-shear viscosity obtained by the Carreau-model agrees with the zero-shear viscosity obtained via the Green-Kubo methodology in equilibrium simulations of PAO-2. This underlines the consistency of the modelling technique described in this study.

Figure 3.9 shows the viscosity as a function of shear rate for the PAO-2 solvent and the two polymer solutions of OCP and PMA polymer chains. With the addition of the polymer chain, the resultant polymer solutions of OCP and PMA are shown to have a higher viscosity than that of the solvent at lower shear rates. For the concentration of OCP and PMA polymers simulated in mesoscale, they are not adding any more favourable shear-thinning than that as seen in case of the PAO-2 solvent.

Even though shear-thinning at simulated shear rates depicts the mild non-Newtonian behaviour, the characteristic that is essential to prove that a liquid is viscoelastic is the first normal stress coefficient (ψ_1) computed as

$$\psi_1 = -\frac{\sigma_{yy} - \sigma_{zz}}{\dot{\gamma}^2}. \tag{3.17}$$

73
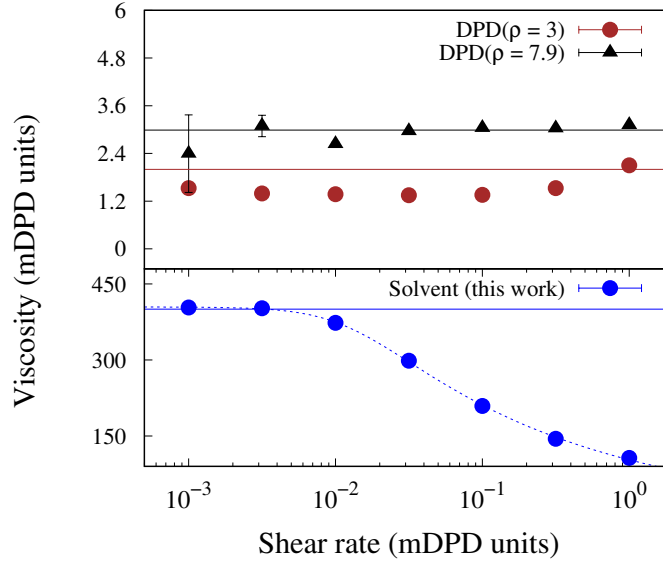
Figure 3.8: Shear viscosity, η as a function of shear rate, $\dot{\gamma}$ for solvent molecules computed in the mesoscale simulations. The horizontal lines show the zero-shear viscosity computed using Green-Kubo method under equilibrium conditions and the dashed line shows the Carreau-model fit.

Here, σ_{yy} is the diagonal component of stress tensor in the direction of flow and σ_{zz} is the component of stress tensor in the direction of the velocity gradient in the Couette flow being examined. For a dilute viscoelastic liquid, the value of ψ_1 has been demonstrated to be greater than zero [98]. It is reported that the greater the magnitude of ψ_1, the greater the fluid tendency to augment instabilities leading to vortex roll-up. In the continuum-scale simulations, the prominent viscoelastic models such as Oldroyd-3-constant and second-order-fluid models show the relationship between the magnitude of ψ_1 and the magnitude of vortical motion [282, 283]. Thus, the influence of fluid rheology on flow and heat-transfer applications becomes evident.

Figure 3.10 shows ψ_1 as a function of shear rate in case of a DPD solvent, the simulated PAO-2 solvent and the polymer solutions. As observed, the DPD solvent has physically insignificant values of $\psi_1 < \approx 0$ at all values of shear rate [284]. Similarly, the simulated PAO-2 solvent shows a Newtonian behaviour at low shear rate. With a higher shear rate, the ψ_1 obtains positive values for the simulated solvent. However, with the addition of a polymer chain, ψ_1 is positive at all shear rates simulated. It confirms the viscoelastic nature achieved with the addition of polymer chains in the solvent [285].
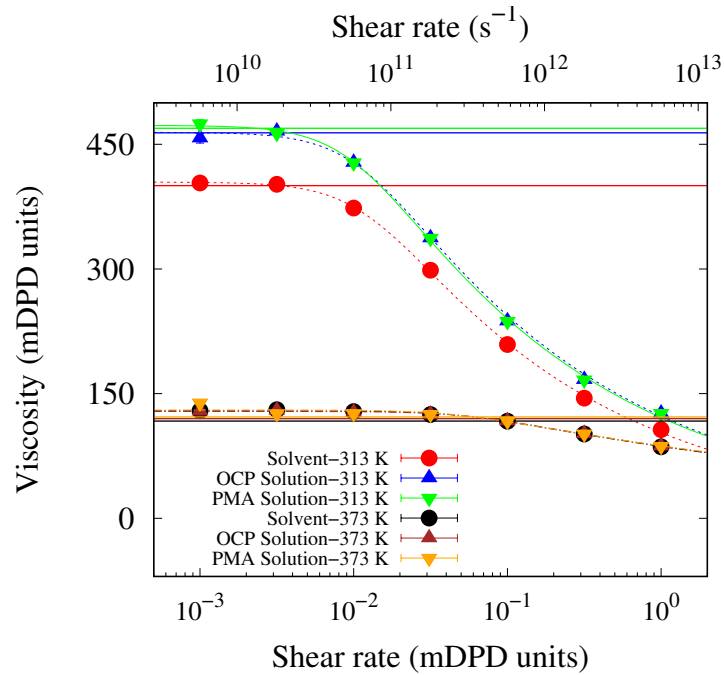
Figure 3.9: Shear viscosity, η as a function of shear rate, $\dot{\gamma}$ at 313 K and 373 K in the mesoscale simulations. The horizontal lines show the zero-shear viscosity computed using Green-Kubo method under equilibrium conditions. The dashed and dash-dotted lines show the Carreau-model fit.
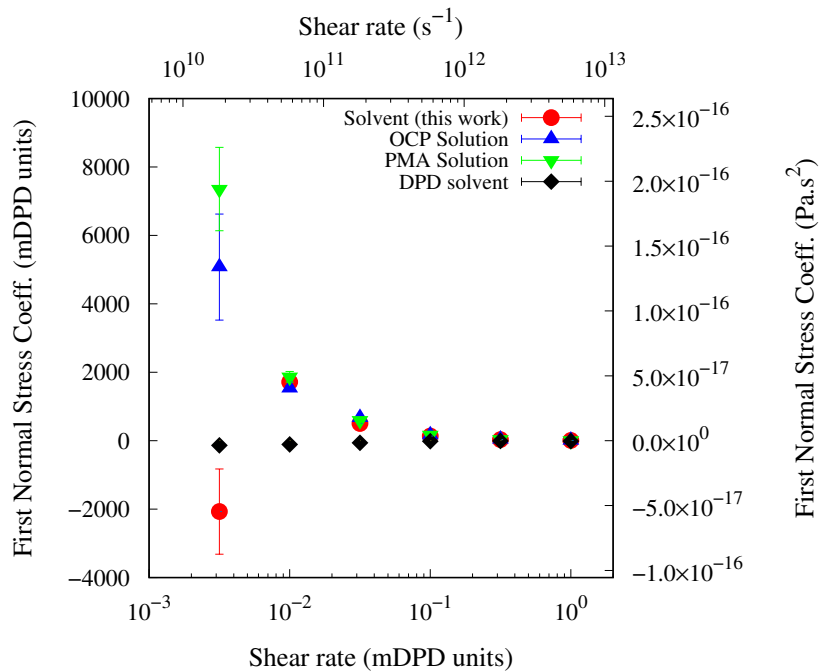
Figure 3.10: First normal stress coefficient, ψ_1 as a function of shear rate, $\dot{\gamma}$ at 313 K computed by mesoscale simulations. DPD solvent has $\rho = 7.9$ (mDPD units).

(a)

(b)
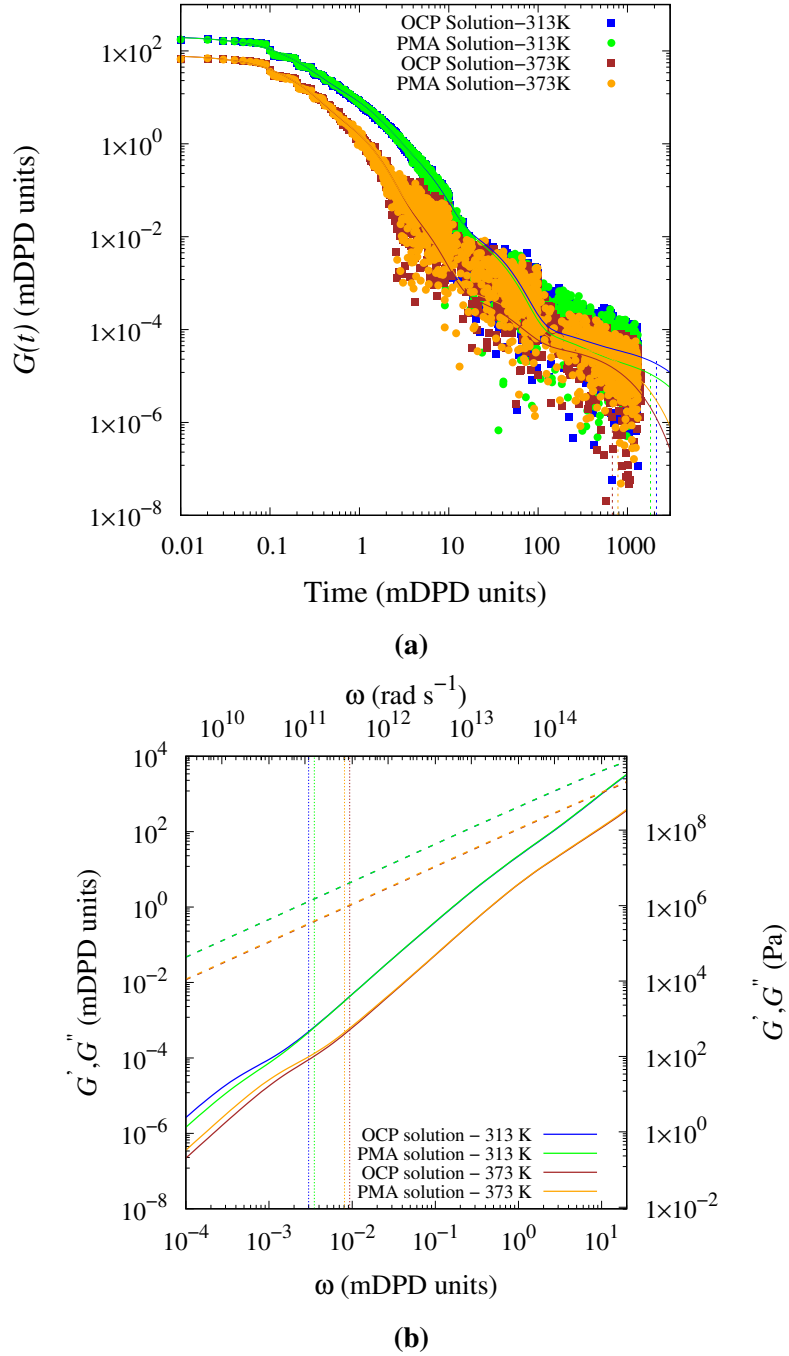
Figure 3.11: (a) $G(t)$ as a function of time at a temperature of 313 K computed by mesoscale simulations for OCP and PMA polymer solutions. The vertical dashed lines correspond to the values of longest relaxation time, τ_Z from Equation 19. (b) The storage modulus, G' (solid) and the loss modulus, G'' (dashed) as a function of radial frequency, ω . The lines for OCP and PMA solutions are seen overlapping for the entire ω range at a particular temperature. The vertical dotted lines correspond to the values of $\frac{2\pi}{\tau_Z}$.

76

The individual contribution of the viscous and elastic components towards the viscoelasticity can be obtained with the computation of storage (G') and loss moduli (G'') from

$$G(t) = \frac{V}{k_B T} \left\langle \sigma_{xy}(t)\sigma_{xy}(0) \right\rangle, \tag{3.18}$$

which is fitted with with a sum of exponential functions

$$G(t) = \sum_{i=1}^{M} G_i e^{-\left(\frac{t}{\tau_i}\right)}. \tag{3.19}$$

with M relaxation modes. Figure 3.11a shows the $G(t)$ values smoothened by doing a running average between 0.9t and 1.1t, as described by Sen et al. [200], and the corresponding fits for OCP and PMA polymer solutions at 313 K and 373 K. The long scattered tail of $G(t)$ ($t >$ 1000 mDPD units) emerging due to numerical precision issues at small magnitudes in the long time regime [286] is further smoothened by taking a weighted average [287]. G' and G'' are subsequently estimated from the Fourier transformation of the Equation 3.19 such that

$$G'(\omega) = \sum_{i=1}^{M} G_i \frac{\omega^2 \tau_i^2}{1 + \omega^2 \tau_i^2} \tag{3.20}$$

and

$$G''(\omega) = \sum_{i=1}^{M} G_i \frac{\omega \tau_i}{1 + \omega^2 \tau_i^2}. \tag{3.21}$$

Figure 3.11b shows G' and G'' of the different polymer solutions as functions of the frequency ω at the two different temperatures. As observed, G' and G'' values decrease with increase in temperature. In other words, the elasticity and viscosity decrease with temperature. The ω values at which the slope of G' and G'' change increase with temperature. This is clearly demonstrated by computing

$$\eta^*(\omega) = \frac{(G'(\omega)^2 + G''(\omega)^2)^{\frac{1}{2}}}{\omega} \tag{3.22}$$

as depicted in Figure B8 in Appendix B. The data shows consistency with the results from Green-Kubo formulation for η_0. At the same time, the value of $\eta^*(\omega)$ decreases at a higher ω with increase in temperature.

The final aspect to verify for the present modelling approach is about how the relaxation time provided by the mDPD model behaves as a function of temperature. In the atomistic MD simulation, the longest relaxation time, i.e., terminal relaxation time is computed using the

formula

$$\tau_{term} = \int_0^\infty C(t)dt \qquad (3.23)$$

where

$$C(t) = \frac{\langle \mathbf{R}(t) \cdot \mathbf{R}(0) \rangle}{\langle \mathbf{R}(0) \cdot \mathbf{R}(0) \rangle} \qquad (3.24)$$

with $\mathbf{R}(t)$ depicting the end-to-end vector ($\mathbf{r}_1 - \mathbf{r}_l$) of the polymer chain having l monomers [269]. As shown in Figure B3 in Appendix B, the τ_{term} values of OCP polymer chain decrease with increasing temperature. However, τ_{term} values of PMA could not be computed due to the extremely slow decay of $C(t)$ at the atomistic scale and hence, they are not reported. The computation of the relaxation time using the same procedure is performed for the case of the mDPD simulations (see Figure B9 in Appendix B) and the results are shown in Figure 3.12a. The comparison of the longest relaxation time, τ_Z obtained from Equation 3.19 is performed against τ_{term} in Table B12. The values of τ_Z are showcased to be in the range of $0.3\tau_{term}$ to $0.4\tau_{term}$ depending on the temperature and the nature of the polymer. In literature, these variations are attributed to the fact that $C(t)$ decays very slowly compared to $G(t)$, given the requirement of true decorrelation in space for $C(t)$ to reach zero [200]. Furthermore, in Figure 3.12a, the relaxation time decreases in case of OCP polymer chain from 92.7 ns to 29.9 ns as a function of temperature. However, the relaxation time of PMA shows a different trend wherein the values decrease from 74.9 ns to 28.6 ns in the temperature range of 313 K - 353 K after which they increase to 40.4 ns at 373 K. This is a possible trend since the expansion of PMA chain with increasing temperature compensates for the additional thermal energy at 373 K, leading to slower dynamics in the solution. The veracity of the claim is supported by the argument that relaxation time is proportional to the physical quantity $\dfrac{[\eta] \times \eta_s}{T}$ according to the Zimm model [101]. Here, $[\eta]$ is the intrinsic viscosity of the polymer chain, η_s is the solvent viscosity and T is the temperature. The same proportionality can be simplified in this case as follows:

$$\tau_{term} \propto Sc_{poly}D_{poly} \cdot Sc_{solvent}D_{solvent}. \qquad (3.25)$$

Figure 3.12b shows that the product in the right-hand side of Equation 3.25 decreases with increasing temperature in case of OCP. However, for PMA, the value increases beyond 353 K for the modelling strategy implemented here. This in turn could lead to the explanation of how OCP in PAO solvent acts merely as a thickener whereas PMA in the same solvent acts as a viscosity index improver (VII) [164, 168].

Figure 3.13a shows the terminal relaxation time values as a function of shear rate. The values in the reduced mDPD units, and the corresponding values in the real units using the scaling parameters in Table 3.1 are depicted in the figure. In case of the OCP polymer chain,
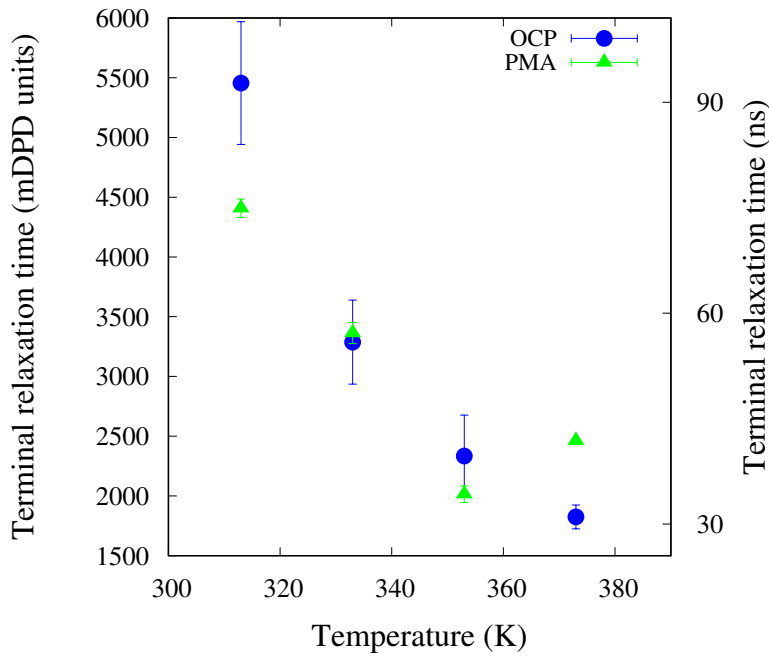
(a)
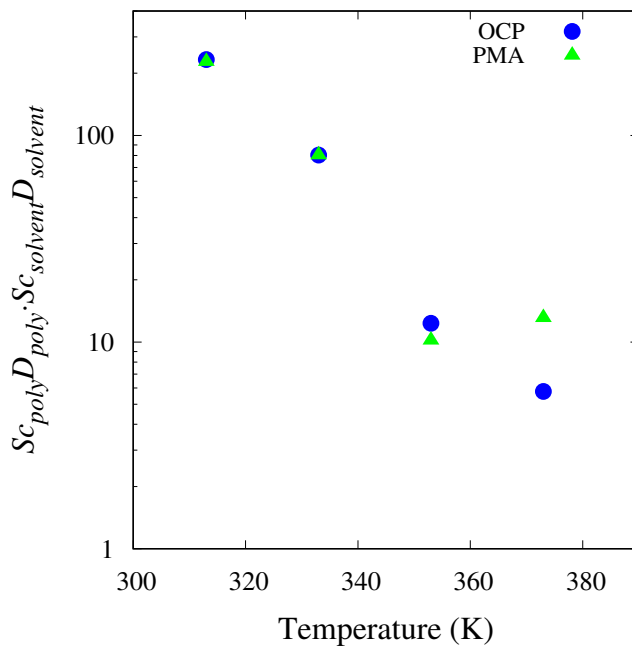
(b)

Figure 3.12: (a) Terminal relaxation time, τ_{term} as a function of temperature, T at zero shear rate for OCP and PMA solutions. (b) $Sc_{poly}D_{poly} \cdot Sc_{solvent}D_{solvent}$ as a function of temperature (refer to Equation 3.25).
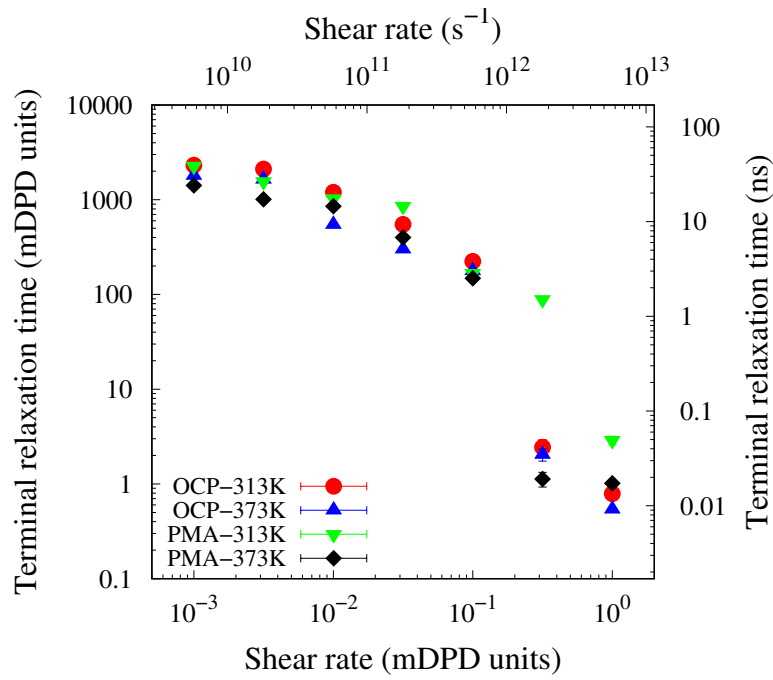
(a)
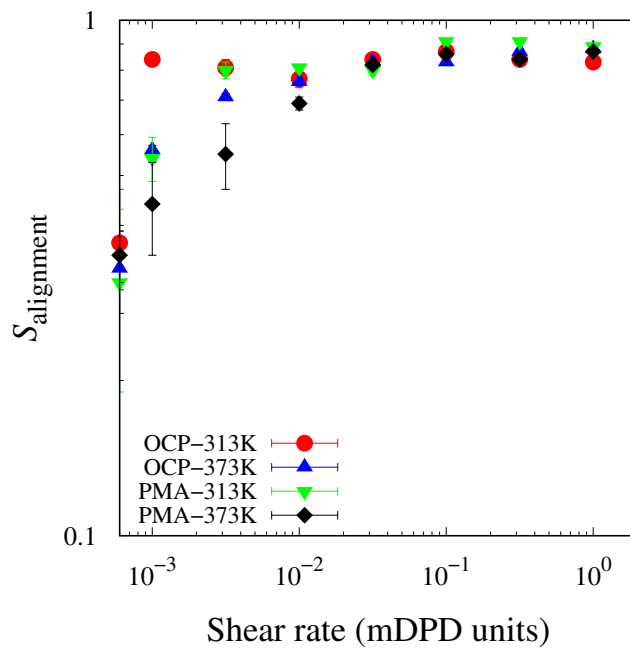
(b)

Figure 3.13: (a) Terminal relaxation time, τ_{term} as a function of shear rate, $\dot{\gamma}$ at 313 K. (b) $S_{\text{alignment}}$ of polymer chains as a function of shear rate at 313 K. The data on the y-axis shows the $S_{\text{alignment}}$ values at zero shear rate.

the τ_{term} decreases with an increase in the shear rate at both 313 K and 373 K. Additionally, it is observed that beyond $\dot{\gamma} = 0.1$, the τ_{term} values drop significantly at both the temperature values. At the same time, PMA polymer chain also shows a decrease in τ_{term} as a function of shear rate. The reduction in τ_{term} values as a function of shear rate is evident from the Zimm model relationship as described above. However, the structural reason is explored in this work. By computing the ratio of the y-component of squared end-to-end distance (R_{ey}) of the polymer chains to the total squared end-to-end distance (R_e) such that

$$S_{\text{alignment}} = \frac{\langle R_{ey}^2 \rangle}{\langle R_e^2 \rangle}, \tag{3.26}$$

i.e., the fraction of molecular stretching aligned in the direction of the shear (y-direction) is observed. As shown in Figure 3.13b, the $S_{\text{alignment}} \approx 0.33$ at zero shear rate. As the shear rate increases, the polymer chains become aligned in the direction of shear as depicted by $S_{\text{alignment}}$ values increasing from 0.45 to 0.9. This in turn leads to the drop in viscosity of the polymer and consequently, the relaxation time as well.

3.3.5 Features of the model and limitations
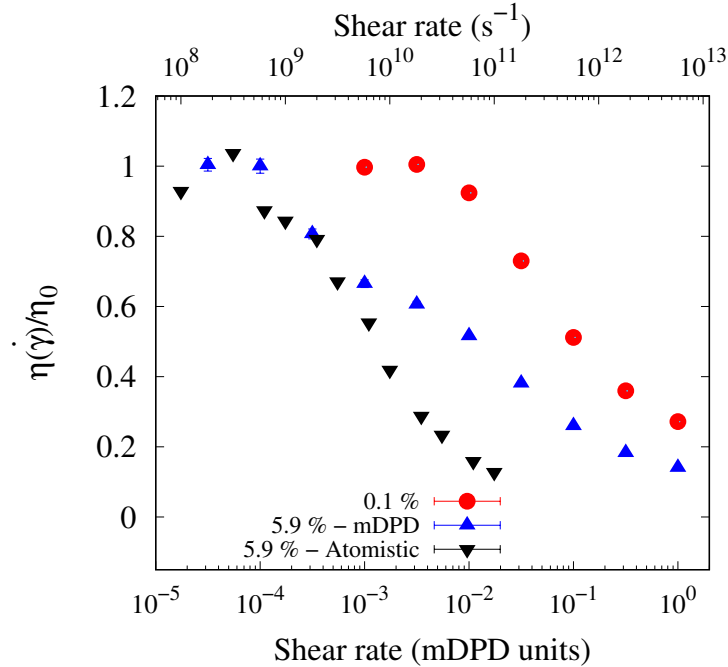
Figure 3.14: The ratio of shear viscosity, $\eta(\dot{\gamma})/\eta_0$ as a function of shear rate, $\dot{\gamma}$ at 313 K for OCP polymer solution with polymer concentrations of 0.1 % and 5.9% by weight.

Simultaneous implementation of the SLLOD thermostat and the mDPD thermostat is functioning appropriately. The consistency in the zero-shear viscosity results computed via equilibrium and non-equilibrium simulations acts as proof of it. The mesoscale model of the liquids of interest is essentially that of a droplet having a diameter of 0.02 μm. The simulation results reported here are intended to reproduce the major features such as molecular structure and rheology, as seen in atomistic simulation studies using a mesoscale model. Properties such as viscosity, relaxation time and first normal stress coefficient are reported for a shear rate range in real units in order to be compared with the atomistic-scale MD. The consistency of the results in the range, as seen in both scales, indicates their mild viscoelasticity. Increasing the polymeric concentration makes the non-Newtonian behaviour more pronounced, as shown in Figure 3.14, with the shear-thinning of 5.9% by weight polymer solution starting at a lower shear rate than the 0.1% polymer solution, an observation that is consistent in the real units as well. At the same time, it needs to be pointed out that the mesoscale model here shows a slower rate of shear thinning than the atomistic scale model. The effect could emerge from the increase in structural ordering of the beads in mesoscale compared with the atomistic scale (see Figure B7 in Appendix B). So it will be vital to improve the model to account for these variations by optimising the excluded volume further. Additionally, the model has reported only the results of solutions simulated treating PAO-2 as a theta or good solvent. The response of the model while considering PAO-2 as a poor solvent, as in the case of natural hydrophilic polymer solutions (e.g. proteins) is not investigated, as it is out of scope of the current study. Therefore, the model will require further studies to expand it for universal applications.

3.4 Conclusions

The responses of terminal relaxation time, viscosity and first normal stress difference as a function of shear rates are vital to determine the distinct aspects of a fluid's non-Newtonian behaviour. To predict those, a framework for non-Newtonian dilute polymer solutions at mesoscale has been developed, capturing the structural differences of OCP and PMA polymers in PAO-2 solvent. The order of magnitude differences in storage and loss moduli between fluids simulated by both mDPD and DPD simulations establish the high sensitivity of the model to identify viscoelastic behaviour. It is achieved by a combination of density-dependent conservative force parameters, and systematically-derived dissipative force cut-off and angle stiffness energies. As a result, the reported relationships between the mDPD (reduced) units and real (SI) units make the model accessible for direct comparison with results from macroscopic experiments of industrially important viscoelastic liquids. By the application of the developed methodology, distinct aspects of the behaviour of the different solutions at mesoscales are

demonstrated, such as the relationship of terminal relaxation time with respect to temperature. Furthermore, the model is able to predict the viscoelasticity introduced with the addition of polymer chains, even at a small concentration of 0.1% by weight, as shown by the computation of the first normal stress coefficient, and storage and loss moduli.

3.5 Critical review

This section contains a brief commentary on the literature post the publication of the article corresponding to this chapter.

The extent of multicomponent coarse-grained simulation improvement is observed in prescribing careful parametrisation of interactions between DPD beads in the literature. The recent work by Curk [288] aims to reproduce the hydrodynamic interactions by controlling the friction coefficient of the dissipative force and the solute-solvent coupling parameters, such as the interaction strength and cut-off. Furthermore, the structural behaviour important for biological macromolecules is investigated by careful construction of mesoscale models derived from intermediate coarse-grained models by Wang and Hernandez [289]. Such developments still require further investigation of the rheological behaviour of polymer solutions. The morphological contributions of polymer chains of different shapes such as bottlebrushes in dilute solutions are studied by Mukkamala and Hore [290] and demonstrate variations in the Zimm scaling relationships. The work further delves into the differences between the radius of gyration and hydrodynamic radius scaling. Thus, there is scope related to further understanding of the rheological behaviour of dilute solutions of macromolecules.

Chapter 4

Viscoelastic nanofluids

[1] A comparative assessment of the thermal properties and heat transfer coefficients achieved by viscoelastic nanofluids suitable for immersion cooling is presented, with the candidate samples exhibiting distinct differences based on the nanoparticle chemistry and shape. Molecular dynamics simulations of different nanoparticles such as copper nanosphere, 2D pristine graphene and single-walled carbon nanotube (CNT) dispersed in PAO-2 of concentrations of approximately equal to 2.6% by weight are performed in the present investigation. While carbon-based nanoparticles increase the specific heat capacity of the nanofluids, the copper-based nanofluids show a decrease in the corresponding values. Moreover, the heat conduction in copper-based nanofluids is dependent on the higher degree of phonon density of states (DOS) matching between the copper and solvent atoms, whereas the high intrinsic thermal conductivity of graphene and CNT compensates for the lower degree of DOS matching. The addition of an OCP polymer chain to impart viscoelasticity in the nanofluids exhibits a heat transfer coefficient enhancement of more than 80% during Couette flow as a result of chain expansion, indicating their suitability for immersive-cooling applications.

4.1   Introduction

The forthcoming regulations in Europe and the US for the phase-out of hydrofluorocarbons coolants (HFCs) used in a wide range of cooling systems, and the necessity for replacement with environmentally friendly fluids with low global-warming potential (GWP) renders the implementation of numerical methodologies for the design of novel coolants timely [291,

---

[1]A significant portion of this chapter is submitted for publication as: B. Ravikumar, I. K. Karathanassis, T. Smith, M. Gavaises, "Atomistic exploration of viscoelastic nanofluids as heat transfer liquids for immersive-cooling applications". The author of this dissertation has contributed to the conceptualisation, methodology, validation, data curation, formal analysis, investigation, writing and visualisation of the article.

292]. In addition, there are stringent mandates in place for decarbonisation of passenger cars and, eventually heavy-duty vehicles, earth-moving machines and aircrafts, which among other significant limitations (such as efficient energy storage, battery weight, safety, limited availability of carbon-free fuels and cost) have to overcome the excess heat generated in electrified powertrains during power-demanding operations with which conventional cooling solutions employing air or water cannot cope [293, 294]. One of the primary areas of interest for engineered cooling fluids is electric vehicle battery thermal management systems (EV BTMS). The existing methodologies of indirect cooling techniques in the BTMS involve a combination of air-cooling and liquid-cooling heat-sink devices and phase change materials [171]. Such systems consist of several energy-consuming components such as pumps, motors, compressors and chillers to maintain the operating temperatures favourable for the safety and long-life of lithium-ion battery modules [295]. Therefore, an advanced mechanism to improve the efficiency of cooling by reducing parasitic power consumption and thermal contact resistances is essential for a sustainable EV roll-out. One such mechanism being proposed is immersive-cooling technique that can reduce the footprint of the BTMS in a passenger vehicles [296], and increase the heat transfer coefficients achieved by five orders of magnitude compared to indirect air-cooling [145].

Given that immersive-cooling involves battery modules directly submerged in the liquid coolants, the options with respect to the involved working media are limited to dielectric fluids such as different types of silicone and mineral oils. However, ensuring minimal frictional losses and higher efficiency of thermal transport are essential characteristics required for immersive-cooling. Therefore, additives are required to assist the oil-based solvents to achieve these targets. The typical additives that are researched for enhancing the rheological properties of oils are polymer chains and surfactants. Experimental studies report the stabilisation of vortices and reduction of thermal boundary layers due to the viscoelastic nature of the polymer chains [151, 96, 152]. Concurrently, a recent focus on the use of nanoparticles to enhance the thermal properties [297] of common cooling liquids motivate the present investigation.

Post the definition of nanofluids by Choi and Eastman [298], the vast majority of works on thermofluids deal with aqueous nanofluids consisting of metal, metal oxide, or carbon allotrope nanoparticles [299–303]. The exposure towards oil-based nanofluids is focussed on enhancing the thermal and rheological properties of lubricants and engine oil [304–306] and the latest experimental research pursue their identification. Cai et al. [307] reported how the Nusselt number increases by 40% when pristine graphene is dissolved in heavy duty diesel engine oil. The measurements of Aberoumand and Jafarimoghaddam [308] showed that 1% weight fraction of copper nanoparticles in engine oil enhances the thermal conductivity by 49%. However, the mechanism of heat transfer is specific to the chemical structure of the fluids as suggested by

the studies of Jin et al. [135] and Alosious et al.[309] Hong et al. [310] showed experimentally that higher thermal conductivity of the elements of nanoparticles does not always improve thermal properties of the nanofluids. The empirical models to compute effective thermal conductivity of solid-liquid suspensions such as Maxwell model [311], Hamilton-Crosser model [312], Davis model [313], Lu-Lin [314] model, Yu and Choi model [315], and Jang and Choi model [316] based on conventional continuum theories are limited to specific systems. Thus, a detailed atomistic exploration is necessary to prescribe the optimal additives necessary to enhance the heat transfer capabilities of different nanofluids. In this research, the stress is on dilute viscoelastic nanofluids that are formed by the addition polymers and nanoparticles in a base solvent. A thorough study to understand the impact of the combination of polymer and nanoparticle additives in an oil solvent is still lacking in the open literature.

Molecular dynamics (MD) simulation is utilised here to compute the thermophysical properties of the nanofluids and provide insights on the mechanism of heat transfer. As the nanofluids are dependent on the chemistry of the nanoparticles and their behaviour in the liquid mixture, the study here considers three different types of nanoparticles, namely copper (Cu) nanosphere representing metallic nanoparticles, 2-dimensional (2D) pristine graphene, and single-walled carbon nanotube (CNT). These different classes of nanoparticles are shown to be industrially relevant for lubrication as well as heat transfer applications [317, 318]. The base oil solvent is chosen as polyalphaolefin (PAO-2) with a kinematic viscosity of approximately 2 cSt at 373 K and to impart viscoelastic nature to the nanofluids, an olefin copolymer (OCP) is dispersed in the different fluids. The elasticity imparted with the addition of polymer chains is recently demonstrated to decrease the thermal boundary layer and improve the Nusselt numbers in laminar flows [158]. Additionally, the polymer chains can stabilise the secondary-flow motion, in turn leading to boundary layer disruption [152]. PAO-2 emerges as an essential solvent for several lubricants due to its high fluidity at lower temperatures and high chemical stability necessary for heat transfer applications [161]. On the other hand, the linear architecture and narrow molecular weight distribution makes OCP a useful additive for industrial applications [162, 164].

Nanofluids of concentrations of approximately 2.6 % by weight are simulated in the temperature range of 313 K and 373 K. The force-field model selection of the different molecules is done after a preliminary investigation of the different structural and transport properties. Heat transfer properties such as specific heat capacity and thermal conductivity are reported for the different nanofluids, following which the mechanism of heat transfer is analysed. The casings of batteries in the packs used in EVs are made by steel, aluminium or plastic [319]. The heat transfer fluids are essentially in contact with these casings during immersion cooling. Therefore, the heat transfer coefficient of the nanofluids flowing through a nanochannel formed

by solid iron (Fe) layers and the role of viscoelasticity in the enhancement of the thermal dissipation of nanofluids is discussed. To the authors' knowledge, the present work constitutes the first investigation in the open literature leveraging MD simulations to estimate the thermal properties of complex-rheology fluids where nanoparticles are also dispersed and provides an understanding of the optimised design of such systems.

4.2 Modelling and simulation

4.2.1 Simulation methodology

Equilibrium MD simulations are initially performed on bulk fluids to verify the modelling approach, and compute the pertinent thermophysical properties. The pure PAO-2 solvent (S1) simulation box is created using 340 molecules of 9,10-dimethyloctadecane [179]. The OCP polymer chain studied here is made up of 50 mole percent of ethylene (C2) monomers and 50 mole percent propylene (C3) monomers with a molecular mass of 3016 g mol^{-1} (Fluid P1) in agreement with the approach followed in Chapter 2. The chain consists of 43 molecules each of C2 and C3 monomers with the two ends of the chain terminated using hydrogen atoms. A copper nanosphere of a diameter of 1 nm is dispersed in the solvent as well as the polymer solution to create Cu nanofluids (Fluids CU1 and CU2). Graphene nanofluids (GR1 and GR2) contain four 2D graphene molecules of long diagonal length 1.2 nm. Similarly, CNT nanofluids (CN1 and CN2) are generated by adding a CNT of length of 1.5 nm, diameter of 0.985 nm and chiral index of (4,10). The selection of these number of molecules correspond to nanoparticle concentrations of $\approx$ 2.6 wt%, which is relevant to heat transfer fluids, as higher concentrations lead to excessive viscosity increase with relevant consequences on pumping losses. The polymer fluids represent a weakly viscoelastic liquid given the chain size and weight of the polymer used. At room temperature, the intrinsic thermal conductivity of copper nanoparticles is reported to be of the order of 400 W m^{-1} K^{-1}, while that of 2D graphene and CNT range up to 5000 W m^{-1} K^{-1} and 6600 W m^{-1} K^{-1}, respectively [320, 321]. Table 4.1 shows the concentration of the additives in the different simulated nanofluids.

Periodic boundary conditions (PBC) are applied in all 3 directions. A Nosé-Hoover thermostat is implemented to maintain the temperatures at equilibration and production runs of the equilibrium MD between 313-373 K. The corresponding Parinello-Rahman barostat as implemented by LAMMPS (NPT) is used to set the pressure at 1 atm during the equilibration phase. The distance cut-off for van der Waals interactions is set to 13 Å. A faster Ewald summation methodology called particle-particle-particle-mesh (PPPM) is used to compute the

long-range electrostatic interactions. The velocity Verlet algorithm is used to integrate the equations of motion with a time-step of 1 fs.

Table 4.1: Concentration (by weight %) of additives in the different nanofluids.

Fluid	Name	Additive concentration	
		Polymer	Nanoparticle
PAO-2	S1	-	-
PAO-2 + 1 OCP	P1	3.04	-
PAO-2 + 1 Cu	CU1	-	2.77
PAO-2 + 1 Cu + 1 OCP	CU2	2.97	2.69
PAO-2 + 4 Graphene	GR1	-	2.63
PAO-2 + 4 Graphene + 1 OCP	GR2	2.97	2.55
PAO-2 + 1 CNT	CN1	-	2.54
PAO-2 + 1 CNT + 1 OCP	CN2	2.97	2.46

1-4 intra-molecular non-bonded pairwise interactions are given a weight of 0.5 for solvent-based fluid simulations, whereas it is switched-off in case of the simulations of polymer-based fluid simulations. Energy minimisation and equilibration under NPT is carried out for 20 ns after which a production run of 40 ns under NVT ensemble is performed. The system after the 40 ns run is utilised for rNEMD simulations to compute the thermal conductivity. In rNEMD simulations, a linear temperature gradient along the z-direction is implemented, as described by Müller-Plathe [52]. The subsequent heat flux is utilised to measure the thermal conductivity values. The reported results of the different properties are averages of three independent simulations with the corresponding standard deviations shown in the appropriate figures.

For simulating the heat transfer during Couette flow between a channel of Fe plates, a simulation box is used which has PBC in x- and y-directions (see Figure 4.1). The boundary in the z-direction is fixed (non-periodic) and the heat transfer liquids are placed between the layers of Fe atoms. The PPPM method is modified here by using the slab option in LAMMPS with a volume factor of 3.0 to obtain accurate electrostatics in the absence of periodicity in z-direction [322]. The outermost 6 layers of Fe on both ends of z-direction have the interactions switched off and a wall repulsion force is used to represent an adiabatic system. The systems are energy minimised to avoid any unphysical configurations. The systems are equilibrated at 313 K using NVT for 4 ns before the innermost two layers of Fe are maintained at 373 K (top layer) and 313 K (bottom layer), respectively using a Langevin thermostat [323]. The top layer at 373 K is moved in the y-direction at $v_{y,max} = 0.1$ Å ps^{-1} and the bottom Fe layer at 313 K is kept stationary by switching off the velocities in both y and z-directions. The simulation set-up generates a Couette flow nanochannel with a heat flux from the top Fe layer to the bottom Fe layer via the liquids.
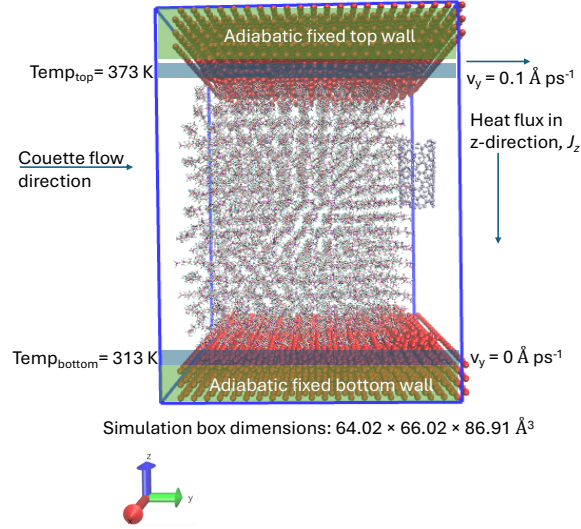
Figure 4.1: Simulation box of nanofluid CN1 after the energy minimisation step. Atoms in red at the top and bottom represent Fe atoms.

4.2.2 Simulation details

A vast array of models and corresponding parameters are available in the literature for the nanoparticles being considered in this research [126, 324, 325, 134, 326, 327, 135, 26, 27, 328–331]. Therefore, a fundamental investigation of the suitability of these models and parameters needs to be performed for the simulated heterogeneous nanofluids. The selection process is accomplished by analysing the stability of the nanoparticles visually in the nanofluids, structural radial distribution function, as well as trends of density and viscosity as a function of temperature.

Multi-body embedded atom model (EAM) potential of the following functional form

$$V_{EAM} = \sum_i E_i(\rho_{h,i}) + \frac{1}{2} \sum_i \sum_{j \neq i} \Phi_{ij}(R_{ij}) \tag{4.1}$$

is used to model the interactions between Cu atoms of the nanoparticles, as they are reported to exhibit atomic cohesion and accurate phonon spectra essential to compute structural and thermal properties for our study. Here, $E_i(\rho_{h,i})$ is the energy to embed atom i into the background host electron density, $\rho_{h,i}$ and $\Phi_{ij}(R_{ij})$ is the core-core pair repulsion between atoms i and j separated by the distance R_{ij}. Foiles et al. [325] has provided a tabulated set of EAM potential parameters for Cu atoms, which are used in the present study.

To describe the graphene and CNT intra-molecular nanoparticle interactions, a bond-order potential formulated by Tersoff of the following basic analytical form

$$V_{Tersoff} = \sum_{i>j} f_c(r_{ij})(V_R(r_{ij}) - b_{ij}V_A(r_{ij}))$$ (4.2)

is predominantly utilised [332]. Here, $V_R(r_{ij})$ and $V_A(r_{ij})$ represent the competing repulsive and attractive bond potentials with $f_c(r_{ij})$ acting as cut-off term ensuring that only nearest-neighbour interactions are accounted for. The bond-order between atoms i and j in Equation 4.2 is given by b_{ij}. Among the different first-principles-based parametrisations available in the literature for Tersoff potentials of carbon, the optimised parameters prescribed by Erhart and Albe [327] possess good transferability while handling hybrid potentials as the ones in this study.

At the same time, it is essential to select the optimal LJ parameters that work well with the selected solid-state potentials in the chemical mixtures simulated. Therefore, the LJ parameters for van der Waals interactions between the nanoparticles and the solvent/polymer are selected after a preliminary investigation of parameters available in the literature [126, 134, 135, 328, 329, 331]. The parameters of PAO-2 and OCP are obtained from the L-OPLS-AA force-field [173, 174]. The LJ parameters and the partial charges of the different atoms are tabulated in Table 4.2 and Table 4.3, respectively. The ε_{ij} values of interactions between the carbon atom of 2D graphene and CNT with the rest of the atoms are determined by further optimising the values by Girifalco et al. [333] until the thermal conductivity value reach a saturation point, as demonstrated by Luo and Lloyd [326].

The different nanofluid mixtures are shown in Figure 4.2. The selected final parameters show Cu nanoparticles remain intact and atoms do not disintegrate(see Figure 4.2a and see Figure 4.2d). The 2D graphene molecules showcase aggregation at the concentrations simulated (see Figure 4.2b and Figure 4.2e), which is in line with its experimental findings [335, 336]. The CNT nanoparticle retains the cylindrical shape with limited shape changes (see Figure 4.2c and Figure 4.2f). The density of the copper, graphene and CNT nanofluids showcase higher values compared to the solvent at all the temperatures exhibiting a linear decrease as a function of temperature (refer to Figure 4.3). Among the nanofluids simulated, CU2 shows the highest density at different temperatures (e.g., 0.805 g cm^{-3} at 313 K) reflecting the mass and concentration of the copper and OCP additives in the nanofluids.

The pairwise radial distribution function (RDF), $g_{o,p}(r)$ is computed using the equation

$$g_{o,p}(r) = \frac{n(r)}{4\pi\rho_{n,p}r^2\delta r}$$ (4.3)

Table 4.2: Lennard Jones (LJ) parameters of the atoms present in the simulations.

Atom types (i-j)	ε_{ij} (kcal mol^{-1})	σ_{ij} (Å)
C_{CH_3}-C_{CH_3} [173]	0.066	3.5
C_{CH_2}-C_{CH_2} [173]	0.066	3.5
C_{CH}-C_{CH} [173]	0.066	3.5
H_{CH_3}-H_{CH_3} [173]	0.030	2.5
H_{CH_2}-H_{CH_2} [173]	0.026	2.5
H_{CH}-H_{CH} [173]	0.030	2.5
C_{CH_3}-C_{CH_2} [173]	0.066	3.5
C_{CH_3}-C_{CH} [173]	0.066	3.5
C_{CH_2}-C_{CH} [173]	0.066	3.5
C_{CH_3}-H_{CH_3}, C_{CH_3}-H_{CH} [173]	0.0445	2.958
C_{CH_2}-H_{CH_3}, C_{CH_2}-H_{CH} [173]	0.0445	2.958
C_{CH}-H_{CH_3}, C_{CH}-H_{CH} [173]	0.0445	2.958
H_{CH_2}-C_{CH_3}, H_{CH_2}-C_{CH_2}, H_{CH_2}-C_{CH} [173]	0.0414	2.958
Cu-C_{CH_3},Cu-C_{CH_2},Cu-C_{CH} [126]	0.7893	2.919
Cu-H_{CH_3},Cu-H_{CH} [126]	0.3725	2.419
Cu-H_{CH_2} [126]	0.3468	2.419
$C_{graphene}$-C_{CH_3},$C_{graphene}$-C_{CH_2},$C_{graphene}$-C_{CH} [326]	0.396	3.5
$C_{graphene}$-H_{CH_3},$C_{graphene}$-H_{CH} [326]	0.267	3.0
$C_{graphene}$-H_{CH_2} [326]	0.2484	3.0
C_{CNT}-C_{CH_3},C_{CNT}-C_{CH_2},C_{CNT}-C_{CH} [326]	0.396	3.5
C_{CNT}-H_{CH_3},C_{CNT}-H_{CH} [326]	0.267	3.0
C_{CNT}-H_{CH_2} [326]	0.2484	3.0
Fe-C_{CH_3},Fe-C_{CH_2},Fe-C_{CH} [334]	0.6293	2.904
Fe-H_{CH_3},Fe-H_{CH} [334]	0.4242	2.404
Fe-H_{CH_2} [334]	0.3949	2.404
Fe-Fe [334]	6.00	2.307
Fe-Cu [328]	0.0025	3.203
Fe-$C_{graphene}$ [331]	0.9916	2.221
Fe-C_{CNT} [331]	0.9916	2.221

Table 4.3: Partial charges of the atoms present in the simulations.

Atom type	q_i (e$^-$)
C$_{CH_3}$ [174]	-0.222
C$_{CH_2}$ [174]	-0.148
C$_{CH}$ [173]	-0.060
H$_{CH_3}$ [174]	0.074
H$_{CH_2}$ [174]	0.074
H$_{CH}$ [173]	0.060
Cu	0.000
Fe	0.000
C$_{graphene}$	0.000
C$_{CNT}$	0.000
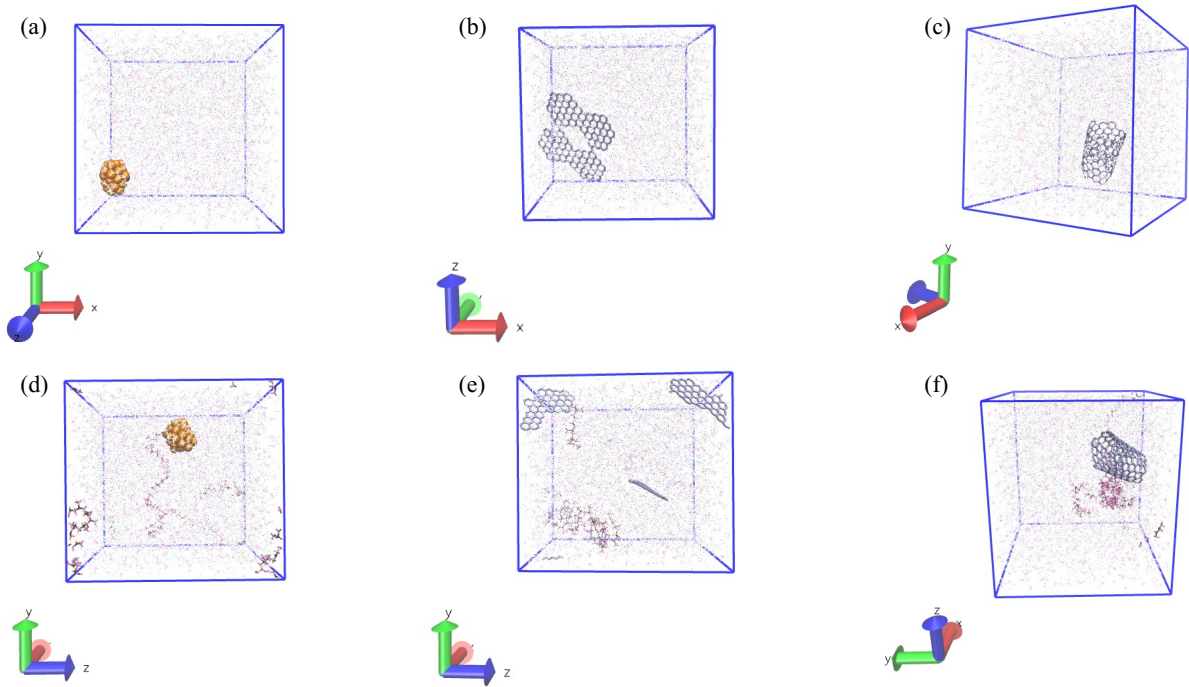
Figure 4.2: Simulation box of nanofluids (a) CU1, (b) GR1 , (c) CN1, (d) CU2, (e) GR2, (f) CN2 at the end of the NPT equilibration run at 313 K. The orange coloured atoms represent Cu in (a) and (d). The purple coloured atoms represent 2D graphene in (b) and (e), and CNT in (c) and (f). The pink atoms represent OCP polymer chain in (d), (e) and (f). The translucent atoms represent PAO-2 solvent in all the simulation boxes.
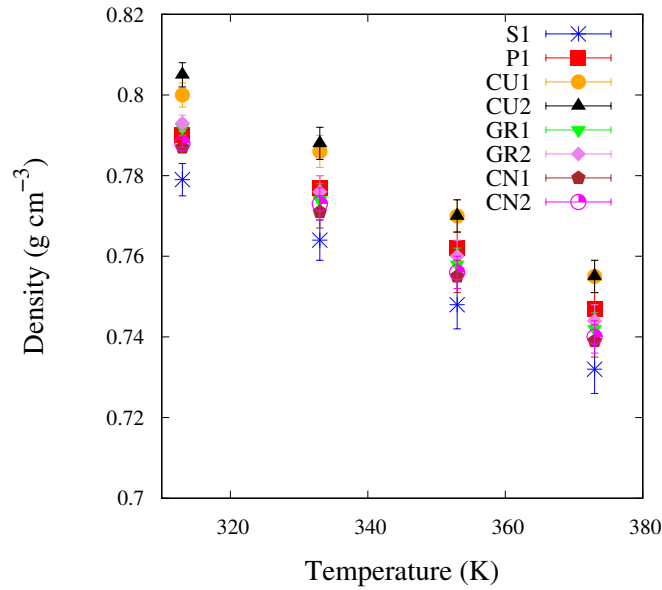
Figure 4.3: Density of the simulated fluids as a function of temperature.

where $n(r)$ is the number of p atoms, with a number density $\rho_{n,p}$ in the simulation box, present in a spherical shell of thickness δr from the central atom o. Figure 4.4 shows the RDF of the carbon atom of the solvent and nanoparticles. $g_{C_{solvent},Cu}(r)$ shows an initial peak at 3.35 Å and $g_{H_{solvent},Cu}(r)$ shows the peak at 2.35 Å. This is comparable with the study by Zhang et al. [337] where the distance between Cu and C shows the initial peak at 3.35 Å. Similarly, the $g_{C_{solvent},C_{graphene}}(r)$ and $g_{C_{solvent},C_{CNT}}(r)$ indicate two short peaks between 3 Å and 4 Å, and between 4 Å and 4.5 Å. Kuziel et al. [338] show similar RDF peaks at these distances between the hydrophobic 2D graphene surface and the carbon atom of oil. This provides us evidence of the models' ability to demonstrate appropriate dissolution of the nanoparticles in the nanofluids.
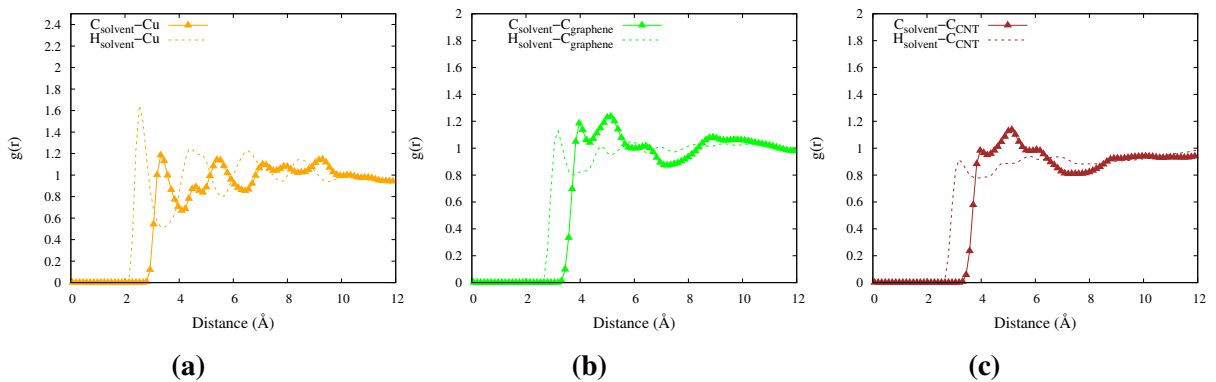
Figure 4.4: Radial distribution functions, (a) $g_{C_{solvent},Cu}(r)$ in CU1, (b) $g_{C_{solvent},C_{graphene}}(r)$ in GR1 and (c) $g_{C_{solvent},C_{CNT}}(r)$ in CN1 at 313 K.

The Green-Kubo method based on the fluctuation-dissipation theorem of systems in equilibrium is used to find the zero-shear dynamic viscosity (η_0). It is computed by the integration of a decaying stress auto-correlation function, such that

$$\eta_0 = \frac{V}{k_B T} \int_0^\infty \left\langle \sigma_{xy}(t)\sigma_{xy}(0) \right\rangle dt. \tag{4.4}$$

Here, V is the volume of the simulation box, k_B is the Boltzmann constant and $\sigma_{xy}(t)$ is one of the off-diagonal components of the stress tensor at time t. The statistics of η_0 computation are improved by taking an average of the auto-correlation function of the three off-diagonal components of the stress tensor. Figure 4.5 depicts the η_0 values of the different fluids simulated at various temperatures between 313 K and 373 K. Nanoparticles increase the viscosity of the resultant nanofluids, with further addition of OCP polymer raising the η_0 values at all the temperatures.
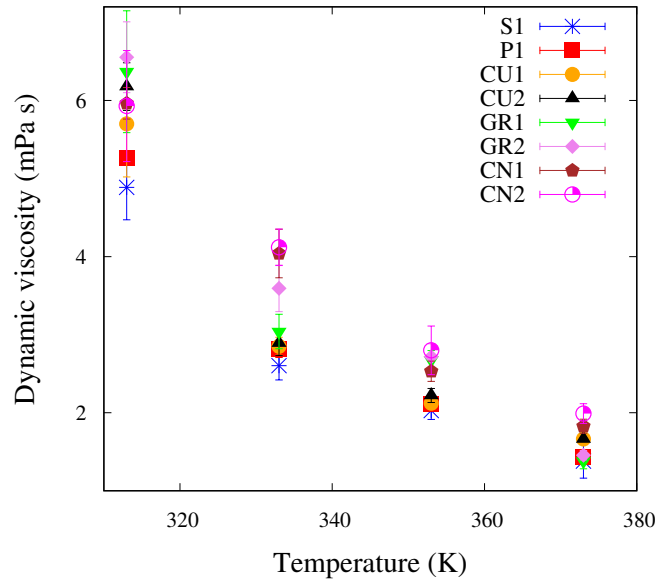
Figure 4.5: Zero-shear dynamic viscosity of the simulated fluids as a function of temperature.

The results presented here demonstrate that the models are suitable for the investigations in the research. Thus, the systems are further simulated to compute the thermal properties of the different fluids.

4.3 Results and discussion

4.3.1 Thermal properties

The specific heat capacity (C_p) of a liquid is computed in an MD simulation using the simplified equation

$$C_p = \frac{\langle E_{total}^2 \rangle - \langle E_{total} \rangle^2}{M_s R T^2}, \tag{4.5}$$

where E_{total} is the total energy of the simulation box, M_s is the total mass of the simulation box and R is the universal gas constant [339, 340].

Figure 4.6a shows the values of C_p as a function of temperature for the different liquids. C_p of PAO-2 increases from 6194 J kg^{-1}K^{-1} at 313 K to 6400 J kg^{-1}K^{-1} at 373 K. The values are higher than the experimental C_p values by a minimum of 2.6 times, and the deviations are addressed as a limitation of OPLS-AA force-fields due to the high energy of classical harmonic bond oscillator vibrations [341]. For the same temperature range, the experimental C_p values range between 2260 J kg^{-1}K^{-1} at 311 K to 2455 J kg^{-1}K^{-1} at 368 K [342]. However, the main objective of the study is to examine the influence of polymers and nanoparticles on the thermal properties of the suspensions rather than the absolute property values. Moreover, the prediction of thermal conductivity trends as reported later with the different additives are in line with the various experimental results and theoretical models.

As observed, the addition of the OCP polymer chain decreases the C_p values at all temperatures. A similar observation is made when Cu nanospheres are added to both the solvent and the OCP polymer solution. However, GR1 and CN1 nanofluids indicate a higher C_p values than the base solvent. This is reflected in the independent experimental studies of Cai et al. [307] and Singh et al. [343] of 2D carbon-based nanoparticles dispersed in oils. On the other hand, the addition of OCP in 2D graphene and CNT polymer solutions leads to a competing effect of the C_p-enhancing nanoparticles and C_p-diminishing polymer chain. This leads to the C_p values of GR2 and CN2 nanofluids being lower than those of the solvent at all the temperatures simulated. The specific heat capacity of solids such as the nanoparticles in the simulated systems is considered as the sum of the electronic and phonon contributions. For all practical purposes, i.e., temperatures above 10 K, the C_p of the nanoparticle is predominantly due to the phonon contribution [344]. The contrasting impact due to copper and carbon-based nanoparticles on the C_p values of the simulated nanofluids may emerge from the differences in their respective phonon dispersion curves. Having understood the capabilities of the different nanofluids in thermal storage, it is important to estimate their thermal transport properties.

For a fluid oriented towards heat transfer applications, thermal conductivity (k) is a vital property to be computed. This metric provides a measure of the ability of a fluid to conduct
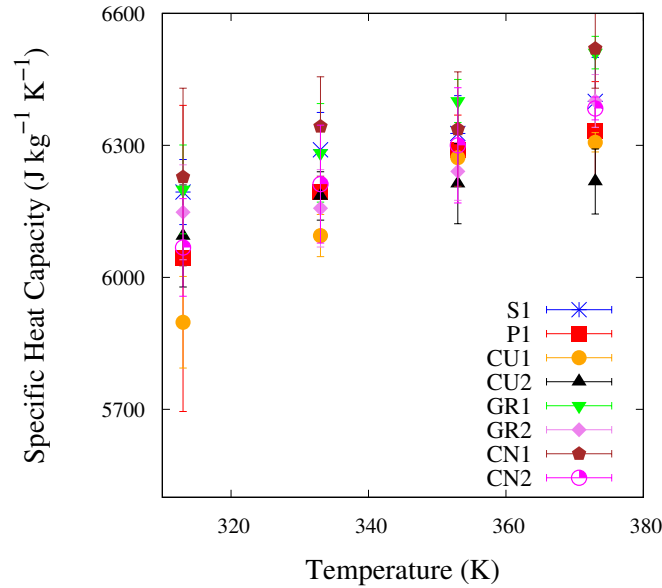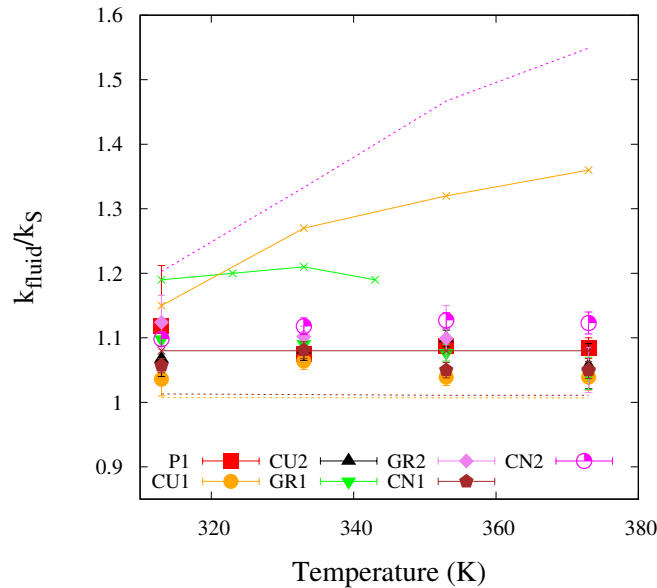
Figure 4.6: (a) Specific heat capacity (C_p) of the simulated fluids as a function of temperature.(b) $\dfrac{k_{fluid}}{k_S}$ of the simulated fluids with additives as a function of temperature. Simulated results are shown by markers with standard deviations. The dashed lines in (b) represent the values estimated by the different theoretical models for the nanofluids of respective volume fractions, such as by Maxwell (orange) [311], Hamilton-Crosser (brown) [312] and Pakdaman et al. (magenta) [345]. The solid lines in (b) represent the experimental results of 1 wt% oil-based copper nanofluid (orange) [308], 3 wt% oil-based graphene nanofluid (green) [307], and 1wt% PAO-2-based MWCNT nanofluid (brown) [346].

Table 4.4: Mean thermal conductivity, k (W m^{-1} K^{-1}) of the simulated fluids as a function of temperature. The corresponding experimental values available in literature [339] are provided inside the parentheses.

Fluid	313 K	333 K	353 K	373 K
S1	0.193 (0.141)	0.186(0.138)	0.181 (0.135)	0.179 (0.132)
P1	0.216	0.200	0.197	0.194
CU1	0.200	0.198	0.188	0.186
CU2	0.206	0.201	0.199	0.189
GR1	0.212	0.203	0.195	0.185
GR2	0.217	0.205	0.199	0.188
CN1	0.204 (0.153*)	0.201 (0.149*)	0.190 (0.146*)	0.188 (0.143*)
CN2	0.212	0.208	0.204	0.201
* MWCNT/PAO-2	nanofluid of	1 wt%	concentration.	

heat given a temperature gradient across it. It is also necessary for the computation of the Nusselt number of novel liquids characterising the ratio of heat transfer via flow convection and conduction.[214] The conduction of heat is due to the microscopic behaviour of the material, constituting MD as a useful tool to compute it [215]. Müller-Plathe [52] methodology is used to compute thermal conductivity, k of the heat transfer fluids simulated. The formulation is based on the following relationship as given by Fourier's law:

$$q = k\nabla T \tag{4.6}$$

where, q is the heat flux across the fluid and ∇T is the corresponding temperature gradient. Müller-Plathe methodology implements the ∇T by routinely exchanging the translational velocities of the atoms in the simulation box conserving momentum. Over a long time period, the continuous exchange of momentum leads to the development of a linear ∇T across the simulation box. The computed k values of the different fluids and the corresponding available experimental data are compared in Table 4.4.

To compare how the different additive-mixed fluids perform against the base solvent, the ratio $\frac{k_{fluid}}{k_S}$ is computed. Figure 4.6b depicts the $\frac{k_{fluid}}{k_S}$ values of the different heat transfer fluids as a function of temperature. OCP and the different nanoparticles lead to an increase in the thermal conductivity of the resultant fluids. The average thermal conductivity of fluid P1 shows an increase of 12% compared to that of the solvent S1 at 313 K, whereas CU1 shows an increase of 4%. GR1 and CN1 exhibit increases of 10% and 6%, respectively at 313K. The addition of OCP polymer chain increases the overall thermal conductivity of the nanofluids even though the appreciation is different for the different nanofluids. While CU2 shows a further enhancement of k by 3% than that of CU1, the ratios for GR2 and CN2 increase by an

additional 1.6% compared to GR1 and CN1, respectively. Most importantly, the addition of OCP in CNT-based nanofluids increases $\dfrac{k_{fluid}}{k_S}$ as temperature increases from 313 K to 373K.

Figure 4.6b compares the results of the different simulated nanofluids to theoretical models and available oil-based nanofluid experimental results. As observed, the traditional solid suspension models by Maxwell [311] and Hamilton-Crosser [312] using the same volume fractions (0.0019-0.0025) as that of the simulated fluids predict lower $\dfrac{k_{fluid}}{k_S}$ ratios. While the Maxwell model is suitable for spherical particles, the Hamilton-Crosser model is used to find the $\dfrac{k_{fluid}}{k_S}$ values of nanofluids of cylindrical nanoparticles. On the other hand, the empirical model described by Pakdaman et al.,[345] which is specific for multi-walled CNT (MWCNT), shows higher $\dfrac{k_{fluid}}{k_S}$ values than those of simulated nanofluids. The experimental values of a 3 wt% oil-based graphene nanofluid and 1 wt% oil-based copper nanofluid are higher than those of the simulated nanofluids, while 1 wt% PAO-2-based MWCNT nanofluid shows values closer to the simulations [307, 308, 346]. The discrepancies between the experimental ratio and the simulated ratio can be attributed to the large size distribution of nanoparticles (diameter $\geq$ 40 nm), the actual chemistry of the oil ($\rho \geq 0.85$ g cm^{-3} and $\eta \geq 130$ mPa s), and the stabilising additives (e.g. lipophilic polymers) used to synthesise the experimental nanofluids.

The differences in the way solid nanoparticles conduct heat in oil could shed light on why the heat transfer properties are different for the different solid-liquid mixtures of nanofluids. In order to quantify the mechanism of heat transfer of the additives in the nanofluids, the phonon density of states (DOS) is computed. The vibrational DOS of a particular atom is computed using the Fourier transform of the velocity autocorrelation function as follows:

$$\text{DOS} = \int \frac{\langle v(t_0) \cdot v(t_0 + t) \rangle}{\langle v(t_0) \cdot v(t_0) \rangle} e^{-2\pi i \omega t} dt. \tag{4.7}$$

Figure 4.7 shows the DOS of the different atoms in the solvent S1, and the nanofluids CU1, GR1 and CN1. As observed in Figure 4.7 the frequencies of carbon are prominent in the lower frequencies between 0 to 40 THz whereas those of hydrogen are present in the high frequency region of 80 to 100 THz. In the case of CU1, the copper nanoparticles show DOS frequencies between 0 to 20 THz. In the cases of GR1 and CN1, the multiple peak frequencies generally coincide with the DOS of carbon atoms of the oil solvent. Here, it is to be mentioned that while copper demonstrates a single major peak, the carbon-based nanoparticles showcase multiple peaks at distinct frequencies. This could lead to the occupation of more phonon states in the case of 2D graphene and CNT, which in turn raises the specific heat capacity of the GR1 and CN1 nanofluids as seen in Figure 4.6a [347]. However, a more accurate understanding of the
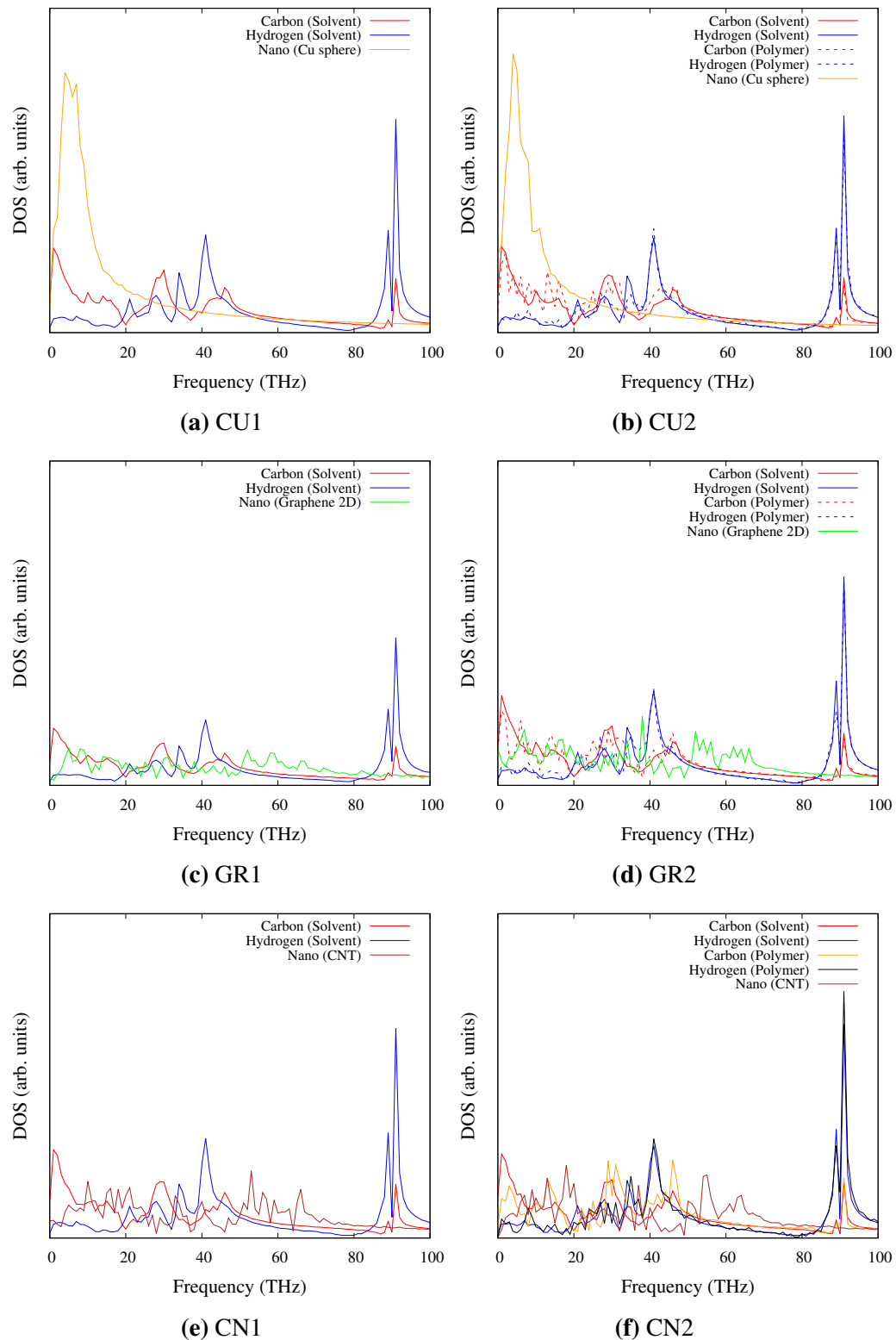
Figure 4.7: The phonon vibrational density of states (DOS) of the different nanofluids at 313 K.
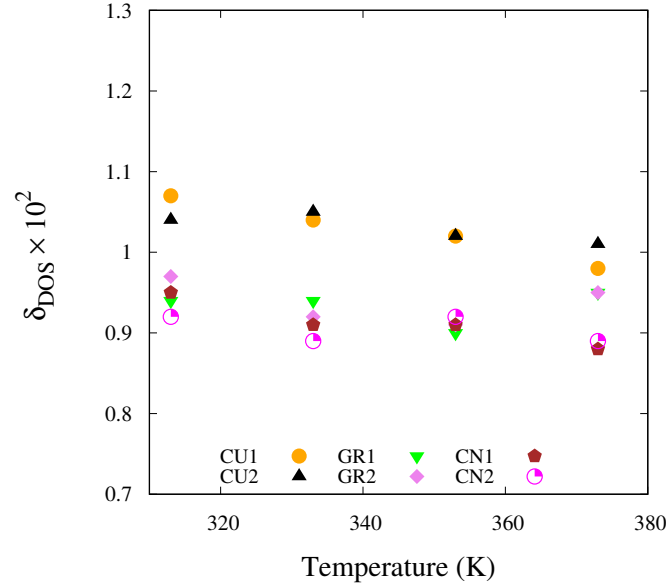
Figure 4.8: δ_{DOS} of the simulated nanofluids as a function of temperature.

phonon dispersion curves requires quantum mechanical studies that are out of scope of the current investigation.

Meanwhile, the matching degree of DOS [348, 349] is obtained using

$$\delta_{DOS} = \frac{\int_0^\infty DOS_{nano}(f)DOS_C(f)DOS_H(f)df}{\int_0^\infty DOS_{nano}(f)df \int_0^\infty DOS_C(f)df \int_0^\infty DOS_H(f)df} \tag{4.8}$$

where $DOS_{nano}(f)$ represents the density of state of nanoparticle, $DOS_C(f)$ represents the DOS of carbon atoms, and $DOS_H(f)$ represents the DOS of hydrogen atoms of the solvent and the polymer molecules. Figure 4.8 depicts the δ_{DOS} values of the different nanofluids. It is evident that CU1 and CU2 exhibit the highest δ_{DOS} values at all the simulated temperatures indicating that phonon transfer is easily facilitated between the nanoparticles and solvent atoms in reference to their heat transfer mechanism. Thus, the contribution of the DOS peak of nanoparticles at very low frequency to the overall thermal conductivity is greater. On the other hand, the δ_{DOS} values of GR1, CN1, GR2 and CN2 are lower than those of copper nanofluids ranging between 0.97 at 313 K and 0.90 at 373K. However, from Figure 4.6b it is evident that the higher values of thermal conductivity are observed for nanofluids consisting of 2D graphene and CNT. In other words, the high intrinsic k values of carbon allotropes compared to copper nanoparticles (*ca.* 4-5 times higher as shown in Table 4.5) are able to compensate for higher interfacial Kapitza resistance [309]. Kapitza resistance is defined as the thermal resistance to the flow of heat at the interface of the solid nanoparticles and the surrounding media. Here, a

Table 4.5: Intrinsic thermal conductvity, k (W m^{-1} K^{-1}) obtained using rNEMD of the different nanoparticles simulated as a function of temperature.

Nanoparticle	313 K	333 K	353 K	373 K
Copper nanosphere	0.26	0.25	0.23	0.22
2D graphene	1.04	0.92	0.85	0.77
CNT	0.94	0.87	0.83	0.80

significant difference in the mechanism of heat transfer between the metallic and carbon-based nanofluids is identified. It is to be pointed out that 2D graphene and CNT thermal properties are critically dependent on the size of the particles and surface modifications (such as dislocations, edge roughness, and vacancies) that may vary the DOS pattern [347].

4.3.2   Heat transfer coefficient

In order to further understand the heat transfer enhancement potential of nanofluids while under convection conditions, the achieved heat transfer coefficient, h in each case is computed by simulating Couette flow between two Fe atomic layers. As described in the section 'Simulation methodology', the moving top Fe layer is heated to 373 K and the stationary bottom Fe layer is maintained at 313 K. This leads to a temperature gradient, that over a long time becomes linear, as shown in Figure 4.9a. The corresponding velocity profile in the y-direction (v_y) is also shown in Figure 4.9b. The heat flux vector in the liquid for such a system is computed as

$$\mathbf{J} = \frac{1}{A \cdot l}[\sum_i e_i \mathbf{v}_i + \frac{1}{2}\sum_{i<j}(\mathbf{F}_{ij} \cdot (\mathbf{v}_i + \mathbf{v}_j))\mathbf{r}_{ij}]. \tag{4.9}$$

where e_i is per-atom total energy and the term $(\mathbf{F}_{ij} \cdot (\mathbf{v}_i + \mathbf{v}_j))\mathbf{r}_{ij}$ is the energy computed from the per-atom stress tensor. A is the cross-sectional area of the simulation box normal to the heat flux direction with a length of fluid enclosure, l. Thus, the heat transfer coefficient in our case is computed as

$$h = \frac{q}{\Delta T} = -\frac{J_z}{\Delta t \Delta T} \tag{4.10}$$

with the timestep of simulation - Δt and the temperature difference between the top and bottom layer of fluid being ΔT.

The heat transfer coefficients of the different fluids simulated are shown in Figure 4.10a. The solvent S1 has a h value of 19.3 $\times 10^{-6}$ W m^{-2} K^{-1}. The addition of Cu nanoparticles increases the h value to 27.6 $\times 10^{-6}$ W m^{-2} K^{-1}, whereas GR1 shows a higher value of 35.5 $\times 10^{-6}$ W m^{-2} K^{-1}. However, the highest h value among the nanoparticles is observed when CNT is added to the oil, showing a consequent increase of 96%. Subsequently, the addition
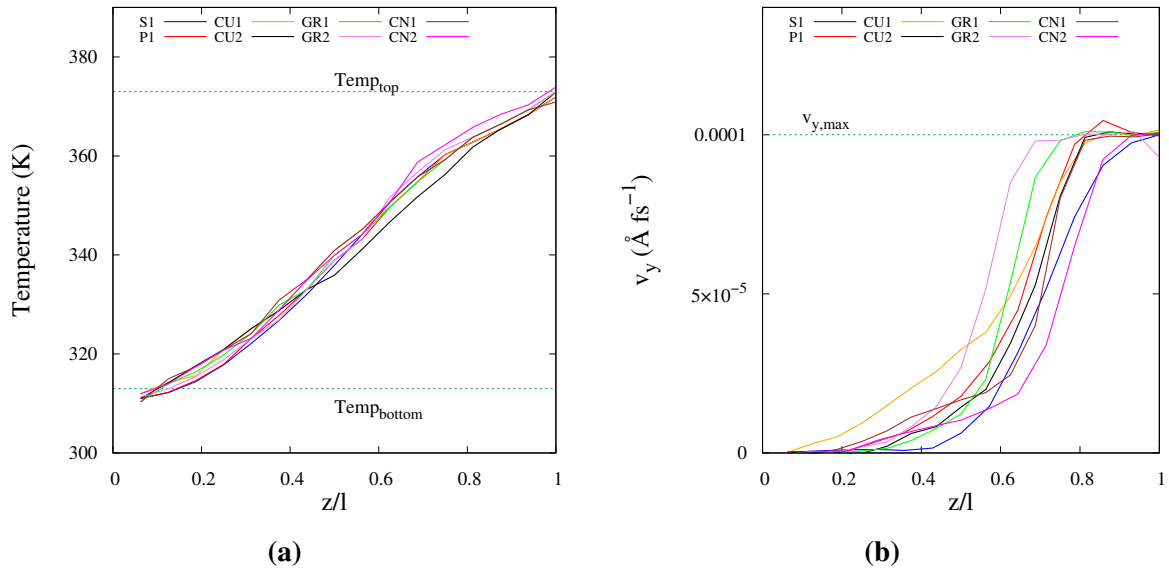
Figure 4.9: (a) The temperature profile in the z-direction during the Couette flow of the different simulated fluids. (b) The velocity profile of the simulated fluids in the y-direction as a function of dimensionless distance with $z/l = 0$ representing the bottommost layer of the fluid and $z/l = 1.0$ representing topmost layer of the fluid. Here, $v_{y,max} = 0.1$ Å ps^{-1} = 0.0001 Å fs^{-1}, Temp$_{top}$ = 373K, and Temp$_{bottom}$ = 313K.
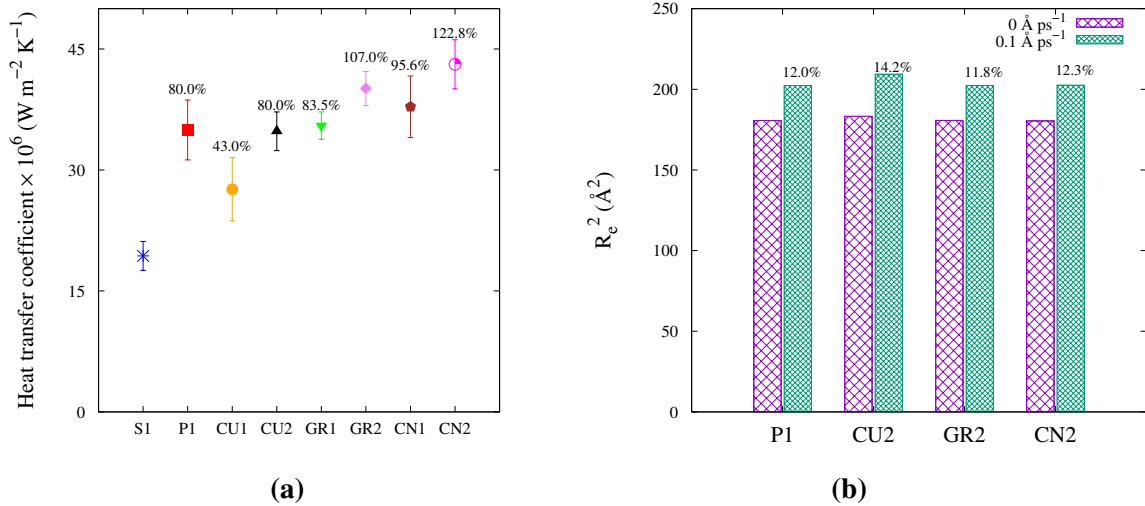
Figure 4.10: (a) The heat transfer coefficient (h) of the simulated fluids as a function of temperature. The percentage value above each data point shows the enhancement of mean h values with respect to the corresponding value of S1. (b) The squared end-to-end distance R_e^2 for the different polymer-added fluids under the conditions of $v_{y,max} = 0$ Å ps^{-1} and 0.1 Å ps^{-1}.

of an OCP polymer chain in the nanofluids shows a substantial increase in the heat transfer coefficients of the different nanofluids compared to the base solvent S1. While CU2 shows an increase of 80% of the h value compared to that of S1, GR2 shows an increase of 107% and CN2 shows an increase of 122%. Thus, the addition of the OCP polymer chain improves the ability of the solutions to transfer heat, which in turn points to a thinner thermal boundary layer. To investigate the relation between the structure of the polymer and the enhancement of the h values in the OCP dissolved nanofluids, computation of the end-to-end distance (R_e) of the OCP polymer chain is performed. Figure 4.10b shows the squared end-to-end distance, R_e^2 values under no flow condition in y-direction and under Couette flow at $v_{y,max}$ = 0.1 Å ps^{-1}. R_e^2 increases under the flow condition compared to the non-flow condition. This is a plausible reason contributing to the heat transfer coefficient enhancement in the polymer-additised nanofluids due to increasing polymer-solvent and polymer-nanoparticle interfacial heat transfer. An increase of 14.2% of the squared end-to-end distance of polymer chain in CU2 showcases an additional 40% net enhancement in h value compared to that of CU1. At the same time, an increase of 11.8% and 12.3% in the R_e^2 values demonstrate additional h value enhancements of 23.5% and 27.2% in GR2 and CN2, respectively. These variations indicate that the total enhancement of the heat transfer coefficients due to polymer addition is still limited by the Kapitza resistance. It is to be noted here that the addition of viscoelastic polymer chains reduces turbulence intensity [350], hindering heat transfer in turbulent flows. The arguments outlined in this section are relevant to laminar flows as simulated in this investigation.

4.3.3 Limitations

The presented research is concerned with nanofluids containing specific nanoparticles with sizes of the order of 1 nm. In real applications (or experiments), the nanoparticle size distributions range anywhere between 10 nm to 0.1 μm. The distinction is reflected in the order of magnitude differences in intrinsic thermal conductivities of the nanoparticles that are simulated (see Table 4.5) and which are available in the experimental literature [320, 321]. The nanofluids may agglomerate or disintegrate during the dynamic flow processes, which are not considered in the reported investigation. Such dynamic changes may affect the quantitative results of the reported heat transfer coefficient enhancements. Moreover, suspension-stabilising agents or surfactants are an important component of practical nanofluids that are not considered here. As reported by Sharma et al. [82], the addition of these dispersants can lead to further modifications in the rheological behaviour of the nanofluids, in essence affecting the heat transfer coefficients.

4.4   Conclusions

Strong evidence for the suitability of oil-based dilute viscoelastic nanofluids for dielectric immersive-cooling applications is demonstrated by the present investigation. Among the nanoparticles dispersed, CNT and 2D Graphene showed higher values of thermal conductivity compared to metallic copper nanospheres within the temperature range of 313-373 K. Such a difference in impact is observed as a result of the different mechanisms of heat transfer between the nanoparticles and solvent PAO-2. While copper shows a higher DOS at lower frequencies assisting in thermal conductivity enhancement, carbon-based nanoparticles are able to overcome the lower DOS matching degree with their high intrinsic thermal conductivity. Subsequently, the dilute nanofluids are shown to have higher heat transfer coefficients than PAO-2. Moreover, the addition of an OCP polymer chain is demonstrated to increase the heat transfer coefficients by more than 80% compared to the base solvent PAO-2 for the flows simulated here. The enhancement in the heat transfer coefficient is dependent on the extent of the polymer chain expansion in combination with the interfacial Kapitza resistance of the nanoparticles and the surrounding media. For the practical use of such nanofluids for immersion-cooling applications, the selection of an appropriate suspension-stabilising agent that does not negatively interfere with the heat transfer mechanisms requires further research.

4.5   Critical review

This section contains a brief commentary on the literature after the submission of the article corresponding to this chapter.

There is a recent work by Li et al. [351] in the field of nanofluids dedicated to the development of machine-learning interatomic potentials aiming at the prediction of thermophysical properties such as viscosity and thermal conductivity. This approach combining MD simulations, DFT and experiments to generate the relevant input data for machine learning algorithms is promising. The methodology may overcome the accuracy issues of the empirically-tuned interatomic force-field potentials, as those used in this work. However, the underlying physics needs to be carefully examined to enable these potentials to be transferable for any molecular system. In parallel, the investigation by Li et al. [352] intends to explain the microscopic heat transfer mechanism by coupling the MD simulations of multi-component nanofluid systems with the machine learning algorithms using 3D point cloud dataset. They may provide more insights into the design of novel nanocoolants.

Chapter 5

Summary and future works

The comprehensive research reported in this thesis addresses three aspects of molecular modelling to design novel heat transfer fluids for immersive-cooling applications. The primary investigation explored the use of a polymer chain such as OCP as an additive to improve the thermal conductivity of the base dielectric solvent such as PAO-2. The subsequent work aimed to develop a systematic mesoscale modelling tool based on mDPD to compute the rheological properties of dilute polymer solutions. Ultimately, the capabilities of viscoelastic nanofluids are probed using molecular dynamics to understand the heat transfer mechanisms and recommend the optimal additive chemistry.

It is observed that the addition of an OCP polymer chain in PAO-2 solvent modifies the rheological properties of the resultant mixture. OCP increases the viscosity of the resultant oil-based solution and acts as a thickener. The corresponding structural analysis confirmed how the addition of a polymer increases the hydrodynamic radii of the solvent molecules and under the shear force during Couette flow, the molecules stretch and align along the direction of the flow. The addition of a polymer chain leads to the shear thinning at a lower shear rate. More importantly, the addition of an OCP polymer chain shows an increase in the thermal conductivity values and demonstrates a lower temperature coefficient of thermal conductivity. Even though the initial investigation showcased the basic effects of the polymer addition to a dielectric solvent, any further study to understand the impact of polymer concentration required a coarse-grained model that can overcome the computational limitations of atomistic-scale studies. Thus, systematic development of a mesoscale modelling method is necessary to capture the atomistic behaviour, and assist in computing properties that can be used to overcome experimental limitations.

The necessity for a novel approach in mesoscale modelling is required in our case because polymers having different chemistries showed different responses to their radii of gyration as a function of temperature. These different responses determined the ability of a polymer chain to

act as a viscosity index improver. While comparing the radius of gyration of PMA and OCP, the values of the former polymer increase as a function of temperature, whereas the mean values of the latter remain the same. Therefore, the translation of these behaviours to the mesoscale model required the identification of the right model and tuning of the parameters relevant to the model. A many-body dissipative particle dynamics model was utilised to depict the interactions of the beads in the simulation combined with a FENE bonding energy and a cosine angle stiffness potential. The parameter tuning aimed to capture the rheology via Schmidt number matching, and structural properties via radius of gyration and radial distribution function. The important objective of the modelling exercise was to compute the relaxation times of the polymer solutions in the temperature range of 313 K to 373 K. The terminal relaxation time of the OCP and PMA polymer chains decreased as a function of shear rate. However, as a function of temperature, the terminal relaxation time of OCP decreased monotonically, while that of PMA showed an increase in values beyond 353 K.

The design of a thermofluid for immersive-cooling applications requires a mixture of heat transfer-enhancing additives. The choice of these additives extends to nanoparticles that are shown to enhance the thermal conductivity of liquids when added. However, the chemistry, morphology and concentration of such nanoparticles that are useful in the case of dielectric fluids pose a research scope. As the use of polymer additives was already established earlier, the behaviour of such fluids in the presence of copper nanospheres, 2D graphene and single-walled CNT is investigated. The research required the use of hybrid force-fields and thus, a fundamental investigation of the accurate model and corresponding parameters was carried out. The specific heat capacity of the PAO-2-based nanofluids with either graphene or CNT showed higher values than the bare solvent. However, the addition of a copper nanoparticle or OCP polymer chain decreased the C_p values. While all the nanoparticle chemistries increased the thermal conductivity of the resultant PAO-2 nanofluids, the heat transfer mechanisms of these nanoparticles were different. By computing the degree of phonon vibrational density of states (δ_{DOS}), it is determined that Cu nanoparticles have higher δ_{DOS} among the simulated nanoparticles, assisting in the phonon transfer between the solvent and Cu atoms. However, the higher intrinsic thermal conductivity of carbon allotropes helps in overcoming the lower δ_{DOS} to improve the overall thermal conductivity of the nanofluids. The addition of an OCP polymer chain that imparts viscoelasticity in the nanofluids leads to an increase in the heat transfer coefficient during Couette flow. The role of chain expansion and Kapitza resistance is observed in the enhancement of the heat transfer coefficient.

The research presented in this thesis has the potential to act as a building block for several future investigations in the field of thermofluids and design of heat transfer liquids. Two directions proposed are as follows: Firstly, the systematic mesoscale model developed in

this work can be extended to simulate viscoelastic nanofluids to study the aggregation of the particles and the consequent rheological impacts. Secondly, the use of nanofluids for practical heat transfer applications such as immersive-cooling requires suspension-stabilising agents such as oleic acid, cetyltrimethylammonium bromide, polyvinyl pyrrolidone, etc. It is important to explore how certain surfactants impact the aggregation of the nanoparticles and the heat transfer capabilities of the nanofluids. Moreover, the research here can be expanded to applications such as spray cooling and jet-impingement cooling of intricate components in electronics and electromechanical devices such as motors. Also, the knowledge about nanofluids gathered as part of the investigation can be put into use for biomedical applications such as drug delivery and antimicrobial treatments.

Chapter 6

Publications

Peer-reviewed journal publications (newest first)

- B. Ravikumar, I. K. Karathanassis, T. Smith, M. Gavaises, "Multi-scale modelling of dilute viscoelastic liquids: Atomistic to mesoscale mapping of polymer solutions", *Polymer*, 285:126360, 2023.

- B. Ravikumar, I. K. Karathanassis, T. Smith, M. Gavaises, "Dilute viscoelastic polymer solutions for dielectric heat transfer applications: A molecular dynamics study", *International Journal of Thermofluids*, 18:100333, 2023.

Pending journal publications

- B. Ravikumar, I. K. Karathanassis, T. Smith, M. Gavaises, "Atomistic exploration of viscoelastic nanofluids as heat transfer liquids for immersive-cooling applications".

Conference/workshop proceedings

- B. Ravikumar, I. K. Karathanassis, M. Gavaises, T. Smith, "Chemically specific multiscale modelling of viscoelastic dielectric liquids", *XIXth International Congress on Rheology (ICR)*, 2023.

- B. Ravikumar, I. K. Karathanassis, M.Gaviases, T. Smith, "Rheological characterisation of viscoelastic polymer solutions by mesoscale modelling", *7th IICR Cavitation and Multi-Phase Flows Workshop*, 2023.

References

[1] M. Bell, A. Gault, M. Thompson, J. Hill, D. Joffe, C. C. Committee, et al., Next steps for uk heat policy (2016).

[2] S. Pu, Y. Liao, K. Chen, J. Fu, S. Zhang, L. Ge, G. Conta, S. Bouzarif, T. Cheng, X. Hu, et al., Thermogalvanic hydrogel for synchronous evaporative cooling and low-grade heat energy harvesting, Nano Letters 20 (2020) 3791–3797.

[3] W. R. Stahel, The circular economy, Nature 531 (2016) 435–438.

[4] S. Rashidi, N. Karimi, B. Sunden, K. C. Kim, A. G. Olabi, O. Mahian, Progress and challenges on the thermal management of electrochemical energy conversion and storage technologies: Fuel cells, electrolysers, and supercapacitors, Progress in Energy and Combustion Science 88 (2022) 100966.

[5] A. Vassighi, M. Sachdev, Thermal and power management of integrated circuits, Springer Science & Business Media, 2006.

[6] M. Al-Zareer, I. Dincer, M. A. Rosen, A review of novel thermal management systems for batteries, International Journal of Energy Research 42 (2018) 3182–3205.

[7] F. S. Hwang, T. Confrey, S. Scully, D. Callaghan, C. Nolan, N. Kent, B. Flannery, Modelling of heat generation in an 18650 lithium-ion battery cell under varying discharge rates, in: ASTFE Digital Library, Begel House Inc., 2020.

[8] A. R. M. Siddique, S. Mahmud, B. Van Heyst, A comprehensive review on a passive (phase change materials) and an active (thermoelectric cooler) battery thermal management system and their limitations, Journal of Power Sources 401 (2018) 224–237.

[9] R. Van Gils, D. Danilov, P. Notten, M. Speetjens, H. Nijmeijer, Battery thermal management by boiling heat-transfer, Energy Conversion and Management 79 (2014) 9–17.

[10] H. Hirano, T. Tajima, T. Hasegawa, T. Sekiguchi, M. Uchino, Boiling liquid battery cooling for electric vehicle, in: 2014 IEEE Conference and Expo Transportation Electrification Asia-Pacific (ITEC Asia-Pacific), IEEE, 2014, pp. 1–4.

[11] Z. Xu, K. S. Park, Y. Diao, What is the assembly pathway of a conjugated polymer from solution to thin films?, Frontiers in Chemistry (2020) 1194.

[12] R. Armstrong, M. S. Jhon, Turbulence induced change in the conformation of polymer molecules, The Journal of Chemical Physics 79 (1983) 3143–3147.

[13] W. J. Han, Y. Z. Dong, H. J. Choi, Applications of water-soluble polymers in turbulent drag reduction, Processes 5 (2017) 24.

[14] E. Sadeghinezhad, M. Mehrali, R. Saidur, M. Mehrali, S. T. Latibari, A. R. Akhiani, H. S. C. Metselaar, A comprehensive review on graphene nanofluids: recent research, development and applications, Energy Conversion and Management 111 (2016) 466–487.

[15] J. Fan, L. Wang, Review of heat conduction in nanofluids, Journal of Heat Transfer 133 (2011) 040801.

[16] D. Frenkel, B. Smit, Understanding molecular simulation: from algorithms to applications, volume 1, Elsevier, 2001.

[17] A. Gavezzotti, Molecular aggregation: structure analysis and molecular simulation of crystals and liquids, volume 19, OUP Oxford, 2006.

[18] A. R. Leach, Molecular modelling: principles and applications, Pearson education, 2001.

[19] W. L. Jorgensen, J. Tirado-Rives, The opls [optimized potentials for liquid simulations] potential functions for proteins, energy minimizations for crystals of cyclic peptides and crambin, Journal of the American Chemical Society 110 (1988) 1657–1666.

[20] H. Sun, S. J. Mumby, J. R. Maple, A. T. Hagler, An ab initio cff93 all-atom force field for polycarbonates, Journal of the American Chemical Society 116 (1994) 2978–2987.

[21] D. A. Case, T. E. Cheatham III, T. Darden, H. Gohlke, R. Luo, K. M. Merz Jr, A. Onufriev, C. Simmerling, B. Wang, R. J. Woods, The amber biomolecular simulation programs, Journal of Computational Chemistry 26 (2005) 1668–1688.

[22] O. Borodin, Polarizable force field development and molecular dynamics simulations of ionic liquids, The Journal of Physical Chemistry B 113 (2009) 11463–11478.

[23] M. González, Force fields and molecular dynamics simulations, École thématique de la Société Française de la Neutronique 12 (2011) 169–200.

[24] M. S. Daw, M. I. Baskes, Semiempirical, quantum mechanical calculation of hydrogen embrittlement in metals, Physical Review Letters 50 (1983) 1285.

[25] M. S. Daw, M. I. Baskes, Embedded-atom method: Derivation and application to impurities, surfaces, and other defects in metals, Physical Review B 29 (1984) 6443.

[26] J. Tersoff, Empirical interatomic potential for carbon, with applications to amorphous carbon, Physical Review Letters 61 (1988) 2879.

[27] D. W. Brenner, Empirical potential for hydrocarbons for use in simulating the chemical vapor deposition of diamond films, Physical review B 42 (1990) 9458.

[28] J. M. Schmidt, R. Brueschweiler, R. R. Ernst, R. L. Dunbrack Jr, D. Joseph, M. Karplus, Molecular dynamics simulation of the proline conformational equilibrium and dynamics in antamanide using the charmm force field, Journal of the American Chemical Society 115 (1993) 8747–8756.

[29] J. L. Asensio, M. Martin-Pastor, J. Jimenez-Barbero, The use of cvff and cff91 force fields in conformational analysis of carbohydrate molecules. comparison with amber molecular mechanics and dynamics calculations for methyl α-lactoside, International Journal of Biological Macromolecules 17 (1995) 137–148.

[30] W. R. Scott, P. H. Hünenberger, I. G. Tironi, A. E. Mark, S. R. Billeter, J. Fennen, A. E. Torda, T. Huber, P. Krüger, W. F. van Gunsteren, The gromos biomolecular simulation program package, The Journal of Physical Chemistry A 103 (1999) 3596–3607.

[31] R. E. Rudd, J. Q. Broughton, Coarse-grained molecular dynamics and the atomic limit of finite elements, Physical Review B 58 (1998) R5893.

[32] K. Kremer, G. S. Grest, Dynamics of entangled linear polymer melts: A molecular-dynamics simulation, The Journal of Chemical Physics 92 (1990) 5057–5086.

[33] P. Espanol, P. Warren, Statistical mechanics of dissipative particle dynamics, EPL (Europhysics Letters) 30 (1995) 191.

[34] L. Verlet, Computer" experiments" on classical fluids. i. thermodynamical properties of lennard-jones molecules, Physical Review 159 (1967) 98.

[35] H. J. Berendsen, J. v. Postma, W. F. Van Gunsteren, A. DiNola, J. R. Haak, Molecular dynamics with coupling to an external bath, The Journal of Chemical Physics 81 (1984) 3684–3690.

[36] G. S. Grest, K. Kremer, Molecular dynamics simulation for polymers in the presence of a heat bath, Physical Review A 33 (1986) 3628.

[37] H. C. Andersen, Molecular dynamics simulations at constant pressure and/or temperature, The Journal of Chemical Physics 72 (1980) 2384–2393.

[38] S. Nosé, A unified formulation of the constant temperature molecular dynamics methods, The Journal of Chemical Physics 81 (1984) 511–519.

[39] W. G. Hoover, Canonical dynamics: Equilibrium phase-space distributions, Physical Review A 31 (1985) 1695.

[40] M. Parrinello, A. Rahman, Polymorphic transitions in single crystals: A new molecular dynamics method, Journal of Applied Physics 52 (1981) 7182–7190.

[41] D. J. Evans, G. P. Morriss, The isothermal/isobaric molecular dynamics ensemble, Physics Letters A 98 (1983) 433–436.

[42] D. J. Evans, W. G. Hoover, B. H. Failor, B. Moran, A. J. Ladd, Nonequilibrium molecular dynamics via gauss's principle of least constraint, Physical Review A 28 (1983) 1016.

[43] R. Edberg, G. Morriss, D. J. Evans, Rheology of n-alkanes by nonequilibrium molecular dynamics, The Journal of Chemical Physics 86 (1987) 4555–4570.

[44] P. T. Cummings, D. J. Evans, Nonequilibrium molecular dynamics approaches to transport properties and non-newtonian fluid rheology, Industrial & Engineering Chemistry Research 31 (1992) 1237–1252.

[45] P. J. Daivis, D. J. Evans, Comparison of constant pressure and constant volume nonequilibrium simulations of sheared model decane, The Journal of Chemical Physics 100 (1994) 541–547.

[46] M. Hloucha, U. Deiters, Fast coding of the minimum image convention, Molecular Simulation 20 (1998) 239–244.

[47] P. P. Ewald, Ewald summation, Ann. Phys 369 (1921) 1–2.

[48] B. A. Luty, W. F. van Gunsteren, Calculating electrostatic interactions using the particle-particle particle- mesh method with nonperiodic long-range interactions, The Journal of Physical Chemistry 100 (1996) 2581–2587.

[49] A. A. Chialvo, P. G. Debenedetti, On the use of the verlet neighbor list in molecular dynamics, Computer physics communications 60 (1990) 215–224.

[50] S. Plimpton, Fast parallel algorithms for short-range molecular dynamics, Journal of Computational Physics 117 (1995) 1–19.

[51] P. J. Daivis, B. Todd, A simple, direct derivation and proof of the validity of the sllod equations of motion for generalized homogeneous flows, The Journal of Chemical Physics 124 (2006) 194103.

[52] F. Müller-Plathe, A simple nonequilibrium molecular dynamics method for calculating the thermal conductivity, The Journal of Chemical Physics 106 (1997) 6082–6085.

[53] A. J. Liu, G. S. Grest, M. C. Marchetti, G. M. Grason, M. O. Robbins, G. H. Fredrickson, M. Rubinstein, M. O. De La Cruz, Opportunities in theoretical and computational polymeric materials and soft matter, Soft Matter 11 (2015) 2326–2332.

[54] R. Saidur, K. Leong, H. A. Mohammed, A review on applications and challenges of nanofluids, Renewable and Sustainable Energy Reviews 15 (2011) 1646–1668.

[55] R. Brighenti, Y. Li, F. J. Vernerey, Smart polymers for advanced applications: a mechanical perspective review, Frontiers in Materials 7 (2020) 196.

[56] M. Smeeth, H. Spikes, S. Gunsel, The formation of viscous surface films by polymer solutions: boundary or elastohydrodynamic lubrication?, Tribology Transactions 39 (1996) 720–725.

[57] G. Ver Strate, M. Struglinski, Polymers as lubricating-oil viscosity modifiers, in: D. N. Schulz, J. E. Glass (Eds.), Polymers as rheology modifiers, 1991, pp. 256–272.

[58] T. Stöhr, B. Eisenberg, M. Müller, A new generation of high performance viscosity modifiers based on comb polymers, SAE International Journal of Fuels and Lubricants 1 (2009) 1511–1516.

[59] S. Choi, Z. G. Zhang, W. Yu, F. Lockwood, E. Grulke, Anomalous thermal conductivity enhancement in nanotube suspensions, Applied Physics Letters 79 (2001) 2252–2254.

[60] H. Fujimoto, S. Sakane, T. Hama, H. Takuda, Transient contact behavior of aqueous polymer solution droplets with transparent hot solid, Experimental Thermal and Fluid Science 96 (2018) 1–10.

[61] G. Ramesh, K. Narayan Prabhu, Effect of polymer concentration on wetting and cooling performance during immersion quenching, Metallurgical and Materials Transactions B 47 (2016) 859–881.

[62] D. Rodman, C. Krause, F. Nürnberger, F.-W. Bach, K. Haskamp, M. Kästner, E. Reithmeier, Induction hardening of spur gearwheels made from 42crmo4 hardening and tempering steel by employing spray cooling, Steel Research International 82 (2011) 329–336.

[63] A. Cocci Jr, J. Picot, Rate of strain effect on the thermal conductivity of a polymer liquid, Polymer Engineering & Science 13 (1973) 337–341.

[64] D.-L. Lee, T. F. Irvine Jr, Shear rate dependent thermal conductivity measurements of non-newtonian fluids, Experimental Thermal and Fluid Science 15 (1997) 16–24.

[65] D. Wallace, C. Moreland, J. Picot, Shear dependence of thermal conductivity in polyethylene melts, Polymer Engineering & Science 25 (1985) 70–74.

[66] S. Eyerer, P. Eyerer, M. Eicheldinger, B. Tübke, C. Wieland, H. Spliethoff, Theoretical analysis and experimental investigation of material compatibility between refrigerants and polymers, Energy 163 (2018) 782–799.

[67] S. Eyerer, C. Wieland, A. Vandersickel, H. Spliethoff, Experimental study of an orc (organic rankine cycle) and analysis of r1233zd-e as a drop-in replacement for r245fa for low temperature heat utilization, Energy 103 (2016) 660–671.

[68] A. Mota-Babiloni, J. Navarro-Esbrí, F. Molés, Á. B. Cervera, B. Peris, G. Verdú, A review of refrigerant r1234ze (e) recent investigations, Applied Thermal Engineering 95 (2016) 211–222.

[69] J. R. Juhasz, L. D. Simoni, A review of potential working fluids for low temperature organic rankine cycles in waste heat recovery, in: 3rd International Seminar on ORC Power Systems, Brussels, Belgium, 2015, pp. 1–10. URL: http://asme-orc2015.fyper.com/online/proceedings/documents/177.pdf.

[70] C. M. Invernizzi, P. Iora, M. Preißinger, G. Manzolini, Hfos as substitute for r-134a as working fluids in orc power plants: A thermodynamic assessment and thermal stability analysis, Applied Thermal Engineering 103 (2016) 790–797.

[71] X. Dai, L. Shi, Q. An, W. Qian, Screening of working fluids and metal materials for high temperature organic rankine cycles by compatibility, Journal of Renewable and Sustainable Energy 9 (2017) 024702.

[72] A. Kotia, P. Rajkhowa, G. S. Rao, S. K. Ghosh, Thermophysical and tribological properties of nanolubricants: A review, Heat and mass transfer 54 (2018) 3493–3508.

[73] A. Rasheed, M. Khalid, W. Rashmi, T. Gupta, A. Chan, Graphene based nanofluids and nanolubricants–review of recent developments, Renewable and Sustainable Energy Reviews 63 (2016) 346–362.

[74] M. K. Dubey, J. Bijwe, S. Ramakumar, Ptfe based nano-lubricants, Wear 306 (2013) 80–88.

[75] W. Dai, B. Kheireddin, H. Gao, H. Liang, Roles of nanoparticles in oil lubrication, Tribology International 102 (2016) 88–98.

[76] Y. Wu, W. Tsui, T. Liu, Experimental analysis of tribological properties of lubricating oils with nanoparticle additives, Wear 262 (2007) 819–825.

[77] Z. Xiaodong, F. Xun, S. Huaqiang, H. Zhengshui, Lubricating properties of cyanex 302-modified mos2 microspheres in base oil 500sn, Lubrication Science 19 (2007) 71–79.

[78] G. Liu, X. Li, B. Qin, D. Xing, Y. Guo, R. Fan, Investigation of the mending effect and mechanism of copper nano-particles on a tribologically stressed surface, Tribology Letters 17 (2004) 961–966.

[79] X. Tao, Z. Jiazheng, X. Kang, The ball-bearing effect of diamond nanoparticles as an oil additive, Journal of Physics D: Applied Physics 29 (1996) 2932.

[80] S. U. Choi, J. A. Eastman, Enhancing thermal conductivity of fluids with nanoparticles, Technical Report, Argonne National Lab.(ANL), Argonne, IL (United States), 1995.

[81] A. Asadi, S. Aberoumand, A. Moradikazerouni, F. Pourfattah, G. Żyła, P. Estellé, O. Mahian, S. Wongwises, H. M. Nguyen, A. Arabkoohsar, Recent advances in preparation methods and thermophysical properties of oil-based nanofluids: A state-of-the-art review, Powder technology 352 (2019) 209–226.

[82] A. K. Sharma, A. K. Tiwari, A. R. Dixit, Rheological behaviour of nanofluids: A review, Renewable and Sustainable Energy Reviews 53 (2016) 779–791.

[83] H. Jin, T. Andritsch, I. A. Tsekmes, R. Kochetov, P. H. Morshuis, J. J. Smit, Properties of mineral oil based silica nanofluids, IEEE Transactions on Dielectrics and Electrical Insulation 21 (2014) 1100–1108.

[84] J. A. Esfahani, M. R. Safaei, M. Goharimanesh, L. R. De Oliveira, M. Goodarzi, S. Shamshirband, E. P. Bandarra Filho, Comparison of experimental data, modelling and non-linear regression on transport properties of mineral oil based nanofluids, Powder Technology 317 (2017) 458–470.

[85] K. Anoop, R. Sadr, M. Al-Jubouri, M. Amani, Rheology of mineral oil-sio2 nanofluids at high pressure and high temperatures, International Journal of Thermal Sciences 77 (2014) 108–115.

[86] V. Zhelezny, N. Lukianov, O. Y. Khliyeva, A. Nikulina, A. Melnyk, A complex investigation of the nanofluids r600a-mineral oil-al2o3 and r600a-mineral oil-tio2. thermophysical properties, International Journal of Refrigeration 74 (2017) 488–504.

[87] I. Mahbubul, R. Saidur, M. Amalina, Influence of particle concentration and temperature on thermal conductivity and viscosity of al2o3/r141b nanorefrigerant, International Communications in Heat and Mass Transfer 43 (2013) 100–104.

[88] I. M. Mahbubul, R. Saidur, M. Amalina, Thermal conductivity, viscosity and density of r141b refrigerant based nanofluid, Procedia Engineering 56 (2013) 310–315.

[89] L. Godson, B. Raja, D. M. Lal, S. Wongwises, Experimental investigation on the thermal conductivity and viscosity of silver-deionized water nanofluid, Experimental Heat Transfer 23 (2010) 317–332.

[90] J. Hone, M. Whitney, C. Piskoti, A. Zettl, Thermal conductivity of single-walled carbon nanotubes, Physical Review B 59 (1999) R2514.

[91] S. Frank, P. Poncharal, Z. Wang, W. A. d. Heer, Carbon nanotube quantum resistors, Science 280 (1998) 1744–1746.

[92] Z. Lou, M. Yang, Molecular dynamics simulations on the shear viscosity of al2o3 nanofluids, Computers & Fluids 117 (2015) 17–23.

[93] F. Jabbari, A. Rajabpour, S. Saedodin, Thermal conductivity and viscosity of nanofluids: a review of recent molecular dynamics studies, Chemical Engineering Science 174 (2017) 67–81.

[94] F. Jabbari, S. Saedodin, A. Rajabpour, Experimental investigation and molecular dynamics simulations of viscosity of cnt-water nanofluid at different temperatures and volume fractions of nanoparticles, Journal of Chemical & Engineering Data 64 (2018) 262–272.

[95] R. G. Larson, Flow-induced mixing, demixing, and phase transitions in polymeric fluids, Rheologica Acta 31 (1992) 497–520.

[96] I. Karathanassis, E. Pashkovski, M. Heidari-Koochi, H. Jadidbonab, T. Smith, M. Gavaises, C. Bruecker, Non-newtonian flow of highly-viscous oils in hydraulic components, Journal of Non-Newtonian Fluid Mechanics 275 (2020) 104221.

[97] A. Onuki, Phase transitions of fluids in shear flow, Journal of Physics: Condensed Matter 9 (1997) 6119.

[98] I. Karathanassis, K. Trickett, P. Koukouvinis, J. Wang, R. Barbour, M. Gavaises, Illustrating the effect of viscoelastic additives on cavitation and turbulence with x-ray imaging, Scientific Reports 8 (2018) 1–15.

[99] H. Naseri, K. Trickett, N. Mitroglou, I. Karathanassis, P. Koukouvinis, M. Gavaises, R. Barbour, D. Diamond, S. E. Rogers, M. Santini, et al., Turbulence and cavitation suppression by quaternary ammonium salt additives, Scientific Reports 8 (2018) 1–15.

[100] F. Del Giudice, G. D'Avino, F. Greco, P. A. Netti, P. L. Maffettone, Effect of fluid rheology on particle migration in a square-shaped microchannel, Microfluidics and Nanofluidics 19 (2015) 95–104.

[101] F. Del Giudice, S. J. Haward, A. Q. Shen, Relaxation time of dilute polymer solutions: A microfluidic approach, Journal of Rheology 61 (2017) 327–337.

[102] J. Zilz, C. Schäfer, C. Wagner, R. J. Poole, M. A. Alves, A. Lindner, Serpentine channels: micro-rheometers for fluid relaxation times, Lab on a Chip 14 (2014) 351–358.

[103] F. Del Giudice, G. D'Avino, F. Greco, I. De Santo, P. A. Netti, P. L. Maffettone, Rheometry-on-a-chip: measuring the relaxation time of a viscoelastic liquid through particle migration in microchannel flows, Lab on a Chip 15 (2015) 783–792.

[104] J. Zilz, R. Poole, M. Alves, D. Bartolo, B. Levaché, A. Lindner, Geometric scaling of a purely elastic flow instability in serpentine channels, Journal of Fluid Mechanics 712 (2012) 203–218.

[105] S. G. Kim, H. S. Lee, Concentration dependence of the extensional relaxation time and finite extensibility in dilute and semidilute polymer solutions using a microfluidic rheometer, Macromolecules 52 (2019) 9585–9593.

[106] S. Haward, Microfluidic extensional rheometry using stagnation point flow, Biomicrofluidics 10 (2016) 043401.

[107] L. Campo-Deano, C. Clasen, The slow retraction method (srm) for the determination of ultra-short relaxation times in capillary breakup extensional rheometry experiments, Journal of Non-Newtonian Fluid Mechanics 165 (2010) 1688–1699.

[108] P. C. Sousa, E. J. Vega, R. G. Sousa, J. M. Montanero, M. A. Alves, Measurement of relaxation times in extensional flow of weakly viscoelastic polymer solutions, Rheologica Acta 56 (2017) 11–20.

[109] D. C. Vadillo, W. Mathues, C. Clasen, Microsecond relaxation processes in shear and extensional flows of weakly elastic polymer solutions, Rheologica Acta 51 (2012) 755–769.

[110] D. Trevelyan, Molecular and multiscale simulations of complex fluids, Ph.D. thesis, 2014. URL: https://core.ac.uk/download/pdf/78075002.pdf.

[111] W.-S. Xu, J.-M. Y. Carrillo, C. N. Lam, B. G. Sumpter, Y. Wang, Molecular dynamics investigation of the relaxation mechanism of entangled polymers after a large step deformation, ACS Macro Letters 7 (2018) 190–195.

[112] B. H. Zimm, Dynamics of polymer molecules in dilute solution: viscoelasticity, flow birefringence and dielectric loss, The Journal of Chemical Physics 24 (1956) 269–278.

[113] J. Padding, W. J. Briels, Zero-shear stress relaxation and long time dynamics of a linear polyethylene melt: A test of rouse theory, The Journal of Chemical Physics 114 (2001) 8685–8693.

[114] Y. Shudo, A. Izumi, K. Hagita, T. Nakao, M. Shibayama, Structure-mechanical property relationships in crosslinked phenolic resin investigated by molecular dynamics simulation, Polymer 116 (2017) 506–514.

[115] Y. Shudo, A. Izumi, K. Hagita, T. Nakao, M. Shibayama, Large-scale molecular dynamics simulation of crosslinked phenolic resins using pseudo-reaction model, Polymer 103 (2016) 261–276.

[116] Q. Guo, P. S. Chung, H. Chen, M. S. Jhon, Molecular rheology of perfluoropolyether lubricant via nonequilibrium molecular dynamics simulation, Journal of Applied Physics 99 (2006) 08N105.

[117] M. Kröger, S. Hess, Rheological evidence for a dynamical crossover in polymer melts via nonequilibrium molecular dynamics, Physical Review Letters 85 (2000) 1128.

[118] J. M. Polson, M. J. Zuckermann, Simulation of short-chain polymer collapse with an explicit solvent, The Journal of Chemical Physics 116 (2002) 7244–7254.

[119] J. R. Prakash, Universal dynamics of dilute and semidilute solutions of flexible linear polymers, Current Opinion in Colloid & Interface Science 43 (2019) 63–79.

[120] R. Datta, L. Yelash, F. Schmid, F. Kummer, M. Oberlack, M. Lukáčová-Medvid'ová, P. Virnau, Shear-thinning in oligomer melts—molecular origins and applications, Polymers 13 (2021) 2806.

[121] R. Everaers, H. A. Karimi-Varzaneh, F. Fleck, N. Hojdis, C. Svaneborg, Kremer–grest models for commodity polymer melts: linking theory, experiment, and simulation at the kuhn scale, Macromolecules 53 (2020) 1901–1916.

[122] C. Svaneborg, R. Everaers, Characteristic time and length scales in melts of kremer–grest bead–spring polymers with wormlike bending stiffness, Macromolecules 53 (2020) 1917–1941.

[123] R. D. Groot, P. B. Warren, Dissipative particle dynamics: Bridging the gap between atomistic and mesoscopic simulation, The Journal of Chemical Physics 107 (1997) 4423–4435.

[124] M. Nafar Sefiddashti, M. Boudaghi-Khajehnobar, B. Edwards, B. Khomami, High-fidelity scaling relationships for determining dissipative particle dynamics parameters from atomistic molecular dynamics simulations of polymeric liquids, Scientific Reports 10 (2020) 1–13.

[125] Q. Rao, Y. Xia, J. Li, J. McConnell, J. Sutherland, Z. Li, A modified many-body dissipative particle dynamics model for mesoscopic fluid simulation: methodology, calibration, and application for hydrocarbon and water, Molecular Simulation 47 (2021) 363–375.

[126] S. Sarkar, R. P. Selvam, Molecular dynamics simulation of effective thermal conductivity and study of enhanced thermal transport mechanism in nanofluids, Journal of Applied Physics 102 (2007) 074302.

[127] H. Babaei, P. Keblinski, J. M. Khodadadi, Equilibrium molecular dynamics determination of thermal conductivity for multi-component systems, Journal of Applied Physics 112 (2012) 054310.

[128] H. Babaei, P. Keblinski, J. Khodadadi, Thermal conductivity enhancement of paraffins by increasing the alignment of molecules through adding cnt/graphene, International Journal of Heat and Mass Transfer 58 (2013) 209–216.

[129] W.-Q. Lu, Q.-M. Fan, Study for the particle's scale effect on some thermophysical properties of nanofluids by a simplified molecular dynamics method, Engineering Analysis with Boundary Elements 32 (2008) 282–289.

[130] T. Jia, Y. Zhang, H. Ma, J. Chen, Investigation of the characteristics of heat current in a nanofluid based on molecular dynamics simulation, Applied Physics A 108 (2012) 537–544.

[131] M. Javanmardi, K. Jafarpur, A molecular dynamics simulation for thermal conductivity evaluation of carbon nanotube-water nanofluids, Journal of Heat Transfer 135 (2013).

[132] N. Nair, M. Park, J.-W. Handgraaf, F. M. Cassiola, Coarse-grained simulations of polymer-grafted nanoparticles: structural stability and interfacial behavior, The Journal of Physical Chemistry B 120 (2016) 9523–9539.

[133] S. Costanzo, G. Ianniruberto, G. Marrucci, D. Vlassopoulos, Measuring and assessing first and second normal stress differences of polymeric fluids with a modular cone-partitioned plate geometry, Rheologica Acta 57 (2018) 363–376.

[134] H. Heinz, R. Vaia, B. Farmer, R. Naik, Accurate simulation of surfaces and interfaces of face-centered cubic metals using 12- 6 and 9- 6 lennard-jones potentials, The Journal of Physical Chemistry C 112 (2008) 17281–17290.

[135] X. Jin, H. Guan, R. Wang, L. Huang, C. Shao, The most crucial factor on the thermal conductivity of metal-water nanofluids: Match degree of the phonon density of state, Powder Technology 412 (2022) 117969.

[136] P. Birbarah, T. Gebrael, T. Foulkes, A. Stillwell, A. Moore, R. Pilawa-Podgurski, N. Miljkovic, Water immersion cooling of high power density electronics, International Journal of Heat and Mass Transfer 147 (2020) 118918.

[137] J. K. Mendizábal, M. Montazeri, D. Huitink, N. Miljkovic, Direct cooling of a planar magnetic converter using dielectric liquid forced convection enabled by additive manufacturing, International Journal of Heat and Mass Transfer 191 (2022) 122809.

[138] D. Shia, J. Yang, S. Sivapalan, R. Soeung, C. Amoah-Kusi, Corrosion study on single-phase liquid cooling cold plates with inhibited propylene glycol/water coolant for data centers, Journal of Manufacturing Science and Engineering 143 (2021).

[139] Y. Deng, C. Feng, E. Jiaqiang, H. Zhu, J. Chen, M. Wen, H. Yin, Effects of different coolants and cooling strategies on the cooling performance of the power lithium ion battery system: A review, Applied Thermal Engineering 142 (2018) 10–29.

[140] D. Lee, Development of bldc motor and multi-blade fan for hev battery cooling system, International Journal of Automotive Technology 15 (2014) 1101–1106.

[141] A. Manzoor, M. Saghir, Heat transfer enhancement in multiple pipes configuration using different fluid mixtures: A numerical approach, International Journal of Thermofluids 10 (2021) 100088.

[142] W. Lin, B. Sunden, Vehicle cooling systems for reducing fuel consumption and carbon dioxide: literature survey, SAE Technical Paper (2010) 1509.

[143] M. Lu, X. Zhang, J. Ji, X. Xu, Y. Zhang, Research progress on power battery cooling technology for electric vehicles, Journal of Energy Storage 27 (2020) 101155.

[144] J. Smith, R. Singh, M. Hinterberger, M. Mochizuki, Battery thermal management system for electric vehicle using heat pipes, International Journal of Thermal Sciences 134 (2018) 517–529.

[145] C. Roe, X. Feng, G. White, R. Li, H. Wang, X. Rui, C. Li, F. Zhang, V. Null, M. Parkes, et al., Immersion cooling for lithium-ion batteries–a review, Journal of Power Sources 525 (2022) 231094.

[146] X. Yin, C. Hu, M. Bai, J. Lv, An investigation on the heat transfer characteristics of nanofluids in flow boiling by molecular dynamics simulations, International Journal of Heat and Mass Transfer 162 (2020) 120338.

[147] K. Schmidmayer, P. Kumar, P. Lavieille, M. Miscevic, F. Topin, Heat transfer intensification in an actuated heat exchanger submitted to an imposed pressure drop, Plos One 14 (2019) e0219441.

[148] S. Antoun, S. Srinivasan, M. Z. Saghir, A refined molecular dynamics approach to predict the thermophysical properties of positively charged alumina nanoparticles suspended in water, International Journal of Thermofluids 12 (2021) 100114.

[149] R. Larson, The Structure and Rheology of Complex Fluids, Topics in Chemical Engineering, OUP USA, 1999. URL: https://books.google.co.uk/books?id=BgTjwAEACAAJ.

[150] J. Niu, C. Fu, W. Tan, Slip-flow and heat transfer of a non-newtonian nanofluid in a microtube, Plos One 7 (2012) e37274.

[151] H. Wu, C. Li, J. Li, Heat transfer enhancement by pulsating flow of a viscoelastic fluid in a microchannel with a rib plate, Nanoscale and Microscale Thermophysical Engineering (2022) 1–17.

[152] M. B. Khan, C. Sasmal, R. Chhabra, Flow and heat transfer characteristics of a rotating cylinder in a fene-p type viscoelastic fluid, Journal of Non-Newtonian Fluid Mechanics 282 (2020) 104333.

[153] H. A. Barnes, A handbook of elementary rheology, volume 1, University of Wales, Institute of Non-Newtonian Fluid Mechanics Aberystwyth, 2000.

[154] M. Hassan, F. Mebarek-Oudina, A. Faisal, A. Ghafar, A. Ismail, Thermal energy and mass transport of shear thinning fluid under effects of low to high shear rate viscosity, International Journal of Thermofluids 15 (2022) 100176.

[155] T. A. Pimenta, J. Campos, Friction losses of newtonian and non-newtonian fluids flowing in laminar regime in a helical coil, Experimental Thermal and Fluid Science 36 (2012) 194–204.

[156] Y. L. Xiong, C.-H. Bruneau, H. Kellay, A numerical study of two dimensional flows past a bluff body for dilute polymer solutions, Journal of Non-Newtonian Fluid Mechanics 196 (2013) 8–26.

[157] M. Poreh, U. Paz, Turbulent heat transfer to dilute polymer solutions, International Journal of Heat and Mass Transfer 11 (1968) 805–818.

[158] S. Parvar, C. B. da Silva, F. Pinho, Thermal boundary layer of laminar flow of dilute polymer solution, International Journal of Heat and Mass Transfer 185 (2022) 122248.

[159] S. Antignard, G. Dupuis, C. Favéro, L. Rodriguez, B. Grassl, Portable rheometer to overcome the challenge of measuring low viscosity solution of acrylamide-based polymers at high temperature with an affordable cost for o&g applications, Journal of Rheology 65 (2021) 1053–1063.

[160] S. L. Anna, G. H. McKinley, Effect of a controlled pre-deformation history on extensional viscosity of dilute polymer solutions, Rheologica Acta 47 (2008) 841–859.

[161] R. Benda, J. Bullen, A. Plomer, Synthetics basics: Polyalphaolefins—base fluids for high-performance lubricants, Journal of Synthetic Lubrication 13 (1996) 41–57.

[162] Y. S. Ko, W.-S. Kwon, M.-H. No, J.-H. Yim, A study on the control of microstructures of polyalphaolefins via cationic polymerization, Polymer (Korea) 39 (2015) 346–352.

[163] Synfluid PAO 2 cSt, Chevron Phillips Chemical Company LP, 2019. URL: https://www.cpchem.com/what-we-do/solutions/polyalphaolefins/products/synfluidr-pao-2-cst.

[164] M. J. Covitch, Olefin copolymer viscosity modifiers, in: Lubricant Additives, CRC Press, 2017, pp. 225–246. doi:10.1201/9781315120621-11.

[165] M. Negi, K. N. Kumar, A. Bhardwaj, G. Kapur, S. Ramakumar, Prediction of thickening efficiency of olefin copolymers and kinematic viscosities of the blended base oils by determining intrinsic viscosities of the copolymers in cyclohexane, Egyptian Journal of Petroleum 31 (2022) 7–14.

[166] M. J. Covitch, K. J. Trickett, et al., How polymers behave as viscosity index improvers in lubricating oils, Advances in Chemical Engineering and Science 5 (2015) 134.

[167] A. Sen, I. D. Rubin, Molecular structures and solution viscosities of ethylene-propylene copolymers, Macromolecules 23 (1990) 2519–2524.

[168] U. S. Ramasamy, S. Lichter, A. Martini, Effect of molecular-scale features on the polymer coil size of model viscosity index improvers, Tribology Letters 62 (2016) 1–7.

[169] P. Panwar, P. Michael, M. Devlin, A. Martini, Critical shear rate of polymer-enhanced hydraulic fluids, Lubricants 8 (2020) 102.

[170] A. A. Pesaran, Battery thermal models for hybrid vehicle simulations, Journal of Power Sources 110 (2002) 377–382.

[171] Q. Wang, B. Jiang, B. Li, Y. Yan, A critical review of thermal management models and solutions of lithium-ion batteries for the development of pure electric vehicles, Renewable and Sustainable Energy Reviews 64 (2016) 106–128.

[172] S. C. Kim, Thermal performance of motor and inverter in an integrated starter generator system for a hybrid electric vehicle, Energies 6 (2013) 6102–6119.

[173] W. L. Jorgensen, D. S. Maxwell, J. Tirado-Rives, Development and testing of the opls all-atom force field on conformational energetics and properties of organic liquids, Journal of the American Chemical Society 118 (1996) 11225–11236.

[174] S. W. Siu, K. Pluhackova, R. A. Böckmann, Optimization of the opls-aa force field for long hydrocarbons, Journal of Chemical Theory and Computation 8 (2012) 1459–1470.

[175] W. L. Jorgensen, J. Tirado-Rives, Molecular modeling of organic and biomolecular systems using boss and mcpro, Journal of Computational Chemistry 26 (2005) 1689–1700.

[176] K. Pluhackova, H. Morhenn, L. Lautner, W. Lohstroh, K. S. Nemkovski, T. Unruh, R. A. Böckmann, Extension of the lopls-aa force field for alcohols, esters, and monoolein bilayers and its validation by neutron scattering experiments, The Journal of Physical Chemistry B 119 (2015) 15287–15299.

[177] J. A. Rackers, Z. Wang, C. Lu, M. L. Laury, L. Lagardère, M. J. Schnieders, J.-P. Piquemal, P. Ren, J. W. Ponder, Tinker 8: software tools for molecular design, Journal of Chemical Theory and Computation 14 (2018) 5273–5289.

[178] S. S. Scheuermann, S. Eibl, P. Bartl, Detailed characterisation of isomers present in polyalphaolefin dimer and the effect of isomeric distribution on bulk properties, Lubrication Science 23 (2011) 221–232.

[179] D. Mathas, W. Holweger, M. Wolf, C. Bohnert, V. Bakolas, J. Procelewska, L. Wang, S. Bair, C.-K. Skylaris, Evaluation of methods for viscosity simulations of lubricants at different temperatures and pressures: a case study on pao-2, Tribology Transactions 64 (2021) 1138–1148.

[180] A. I. Jewett, D. Stelter, J. Lambert, S. M. Saladi, O. M. Roscioni, M. Ricci, L. Autin, M. Maritan, S. M. Bashusqeh, T. Keyes, et al., Moltemplate: A tool for coarse-grained modeling of complex biological matter and soft condensed matter physics, Journal of Molecular Biology 433 (2021) 166841.

[181] M. Len, U. S. Ramasamy, S. Lichter, A. Martini, Thickening mechanisms of polyisobutylene in polyalphaolefin, Tribology Letters 66 (2018) 1–9.

[182] L. Mohammed, H. Nourddine, D. Abdelali, R. Hamid, et al., Chitosan-covered liposomes as a promising drug transporter: Nanoscale investigations, RSC Advances 11 (2021) 1503–1516.

[183] S. S. Bair, High pressure rheology for quantitative elastohydrodynamics, Elsevier, 2019.

[184] J. Dymond, R. Malhotra, The tait equation: 100 years on, International Journal of Thermophysics 9 (1988) 941–951.

[185] A. Bakak, M. Lotfi, R. Heyd, A. Ammar, A. Koumina, Viscosity and rheological properties of graphene nanopowders nanofluids, Entropy 23 (2021) 979.

[186] S. Hamze, D. Cabaleiro, P. Estellé, Graphene-based nanofluids: A comprehensive review about rheological behavior and dynamic viscosity, Journal of Molecular Liquids 325 (2021) 115207.

[187] S. Temkin, S. Temkin, Elements of acoustics, Wiley New York, 1981.

[188] J.-P. Rivet, Green-kubo formalism for lattice gas hydrodynamics and monte-carlo evaluation of shear viscosities, Complex Systems 1 (1987) 839–851.

[189] Y. Nakamura, S. Hiraiwa, F. Suzuki, M. Matsui, High-pressure viscosity measurements of polyalphaorefins at elevated temperature, Tribology Online 11 (2016) 444–449.

[190] P. Luo, Y. Gu, Effects of asphaltene content on the heavy oil viscosity at different temperatures, Fuel 86 (2007) 1069–1078.

[191] I. O. Igwe, The effects of temperature on the viscosity of vegetable oils in solution, Industrial Crops and Products 19 (2004) 185–190.

[192] T. Budtova, P. Navard, Viscosity-temperature dependence and activation energy of cellulose solutions, Nordic Pulp & Paper Research Journal 30 (2015) 99–104.

[193] A. Tager, V. Y. Dreval, F. Khasina, Concentrated polymer solutions—iii. viscosity of polyisobutylene solutions in various solvents, Polymer Science USSR 4 (1963) 1097–1106.

[194] B. Ravikumar, M. Mynam, S. Repaka, B. Rai, Solvation shell dynamics explains charge transport characteristics of lib electrolytes, Journal of Molecular Liquids 338 (2021) 116613.

[195] A. Lees, S. Edwards, The computer study of transport processes under extreme conditions, Journal of Physics C: Solid State Physics 5 (1972) 1921.

[196] A. J. Wagner, I. Pagonabarraga, Lees–edwards boundary conditions for lattice boltzmann, Journal of Statistical Physics 107 (2002) 521–537.

[197] D. J. Evans, G. Morriss, Nonlinear-response theory for steady planar couette flow, Physical Review A 30 (1984) 1528.

[198] P. Santak, G. Conduit, Enhancing nemd with automatic shear rate sampling to model viscosity and correction of systematic errors in modeling density: Application to linear and light branched alkanes, The Journal of Chemical Physics 153 (2020) 014102.

[199] B. Purnode, M. Crochet, Polymer solution characterization with the fene-p model, Journal of non-newtonian fluid mechanics 77 (1998) 1–20.

[200] S. Sen, S. K. Kumar, P. Keblinski, Viscoelastic properties of polymer melts from equilibrium molecular dynamics simulations, Macromolecules 38 (2005) 650–653.

[201] P. Liu, J. Lu, H. Yu, N. Ren, F. E. Lockwood, Q. J. Wang, Lubricant shear thinning behavior correlated with variation of radius of gyration via molecular dynamics simulations, The Journal of Chemical Physics 147 (2017) 084904.

[202] S. Cui, S. Gupta, P. Cummings, H. Cochran, Molecular dynamics simulations of the rheology of normal decane, hexadecane, and tetracosane, The Journal of Chemical Physics 105 (1996) 1214–1220.

[203] J. Moore, S. Cui, H. Cochran, P. Cummings, Rheology of lubricant basestocks: A molecular dynamics study of c 30 isomers, The Journal of Chemical Physics 113 (2000) 8833–8840.

[204] N. Marx, L. Fernández, F. Barceló, H. Spikes, Shear thinning and hydrodynamic friction of viscosity modifier-containing oils. part i: shear thinning behaviour, Tribology Letters 66 (2018) 1–14.

[205] T. Selby, The non-newtonian characteristics of lubricating oils, ASLE transactions 1 (1958) 68–81.

[206] P. J. Flory, Principles of polymer chemistry, Cornell University Press, 1953.

[207] S. Rizvi, A Comprehensive Review of Lubricant Chemistry, Technology, Selection, and Design, ASTM manual series, ASTM International, 2009. URL: https://books.google.co.in/books?id=XKLJvQEACAAJ.

[208] J. Dale, The conformational consequences of replacing methylene groups by ether oxygen, Tetrahedron 30 (1974) 1683–1694.

[209] C.-C. Huang, G. Gompper, R. G. Winkler, Non-equilibrium relaxation and tumbling times of polymers in semidilute solution, Journal of Physics: Condensed Matter 24 (2012) 284131.

[210] X. Kong, Y. Han, W. Chen, F. Cui, Y. Li, Understanding conformational and dynamical evolution of semiflexible polymers in shear flow, Soft Matter 15 (2019) 6353–6361.

[211] R. G. Winkler, D. A. Fedosov, G. Gompper, Dynamical and rheological properties of soft colloid suspensions, Current Opinion in Colloid & Interface Science 19 (2014) 594–610.

[212] J. Snoeijer, A. Pandey, M. Herrada, J. Eggers, The relationship between viscoelasticity and elasticity, Proceedings of the Royal Society A 476 (2020) 20200419.

[213] A. Mordvinkin, D. Döhler, W. H. Binder, R. H. Colby, K. Saalwächter, Terminal flow of cluster-forming supramolecular polymer networks: Single-chain relaxation or micelle reorganization?, Physical Review Letters 125 (2020) 127801.

[214] L. Pekar, Advanced Analytic and Control Techniques for Thermal Systems with Heat Exchangers, Academic Press, 2020.

[215] T. S. Komatsu, N. Nakagawa, S.-i. Sasa, H. Tasaki, Steady-state thermodynamics for heat conduction: microscopic derivation, Physical Review Letters 100 (2008) 230602.

[216] Y. Wada, Y. Nagasaka, A. Nagashima, Measurements and correlation of the thermal conductivity of liquid n-paraffin hydrocarbons and their binary and ternary mixtures, International Journal of Thermophysics 6 (1985) 251–265.

[217] M. R. Rao, Thermal conductivity of liquids, The Journal of Chemical Physics 9 (1941) 120–121.

[218] C. Vélez, M. Khayet, J. O. De Zárate, Temperature-dependent thermal properties of solid/liquid phase change even-numbered n-alkanes: n-hexadecane, n-octadecane and n-eicosane, Applied Energy 143 (2015) 383–394.

[219] E. Booser, Tribology Data Handbook: An Excellent Friction, Lubrication, and Wear Resource, CRC Press, 1997. URL: https://books.google.co.uk/books?id=VRmLriy00pQC.

[220] C. F. Curtiss, R. Byron Bird, Thermal conductivity of dilute solutions of chainlike polymers, The Journal of Chemical Physics 107 (1997) 5254–5267.

[221] R. Byron, B. C. F. Curtiss, K. J. Beers, Polymer contribution to the thermal conductivity and viscosity in a dilute solution (fraenkel dumbbell model), Rheologica Acta 36 (1997) 269–276.

[222] T. Zhou, Z. Wu, H. K. Chilukoti, F. Müller-Plathe, Sequence-engineering polyethylene–polypropylene copolymers with high thermal conductivity using a molecular-dynamics-based genetic algorithm, Journal of Chemical Theory and Computation 17 (2021) 3772–3782.

[223] N. Nirmalkar, R. Chhabra, R. Poole, Effect of shear-thinning behaviour on heat transfer from a heated sphere in a yield-stress fluids, Industrial & Engineering Chemistry Research 52 (2013) 13490–13504.

[224] L. F. Mercier Franco, A. Firoozabadi, Computation of shear viscosity by a consistent method in equilibrium molecular dynamics simulations: applications to 1-decene oligomers, The Journal of Physical Chemistry B 127 (2023) 10043–10051.

[225] K. Khajeh, D. Talukdar, S. Yamamoto, S. Endo, K. Kamio, H. Washizu, A comparative study of polymer viscosity modifiers: Flow field challenges & alternative trends, Journal of Molecular Liquids 393 (2024) 123590.

[226] J. Liu, H. Chen, M. Yang, S. Huang, K. Wang, Comparative study of natural ester oil and mineral oil on the applicability of the immersion cooling for a battery module, Renewable Energy 224 (2024) 120187.

[227] A. T. Kumaran, S. Hemavathi, Optimization of lithium-ion battery thermal performance using dielectric fluid immersion cooling technique, Process Safety and Environmental Protection (2024).

[228] P. Tan, H. Wang, F. Xiao, X. Lu, W. Shang, X. Deng, H. Song, Z. Xu, J. Cao, T. Gan, et al., Solution-processable, soft, self-adhesive, and conductive polymer composites for soft electronics, Nature Communications 13 (2022) 358.

[229] K. Zhou, K. Xian, L. Ye, Morphology control in high-efficiency all-polymer solar cells, InfoMat 4 (2022) e12270.

[230] X. Li, C. Pu, X. Chen, Improved foam stability through the combination of silica nanoparticle and thixotropic polymer: An experimental study, Journal of Molecular Liquids 346 (2022) 117153.

[231] R. Cerbino, F. Giavazzi, M. E. Helgeson, Differential dynamic microscopy for the characterization of polymer systems, Journal of Polymer Science 60 (2022) 1079–1089.

[232] A. Yazdani, M. Deng, B. Caswell, G. E. Karniadakis, Flow in complex domains simulated by dissipative particle dynamics driven by geometry-specific body-forces, Journal of Computational Physics 305 (2016) 906–920.

[233] V. Harmandaris, V. Mavrantzas, D. Theodorou, M. Kröger, J. Ramirez, H. C. Öttinger, D. Vlassopoulos, Crossover from the rouse to the entangled polymer melt regime: signals from long, detailed atomistic molecular dynamics simulations, supported by rheological experiments, Macromolecules 36 (2003) 1376–1387.

[234] C. Baig, B. J. Edwards, D. J. Keffer, H. D. Cochran, Rheological and structural studies of liquid decane, hexadecane, and tetracosane under planar elongational flow using nonequilibrium molecular-dynamics simulations, The Journal of Chemical Physics 122 (2005) 184906.

[235] J. Moore, S. Cui, H. Cochran, P. Cummings, A molecular dynamics study of a short-chain polyethylene melt.: I. steady-state shear, Journal of Non-Newtonian Fluid Mechanics 93 (2000) 83–99.

[236] C. Baig, V. A. Harmandaris, Quantitative analysis on the validity of a coarse-grained model for nonequilibrium polymeric liquids under flow, Macromolecules 43 (2010) 3156–3160.

[237] A. Menzel, P. Daivis, B. Todd, Equilibrium and nonequilibrium molecular dynamics methods to compute the first normal stress coefficient of a model polymer solution, Physical Review Fluids 5 (2020) 084201.

[238] W. A. Pisani, M. S. Radue, S. Chinkanjanarot, B. A. Bednarcyk, E. J. Pineda, K. Waters, R. Pandey, J. A. King, G. M. Odegard, Multiscale modeling of peek using reactive molecular dynamics modeling and micromechanics, Polymer 163 (2019) 96–105.

[239] J. Zhao, S. Chen, K. Zhang, Y. Liu, A review of many-body dissipative particle dynamics (mdpd): Theoretical models and its applications, Physics of Fluids 33 (2021) 112002.

[240] Q. Sun, R. Faller, Phase separation in polyisoprene/polystyrene blends by a systematically coarse-grained model, The Journal of Chemical Physics 126 (2007) 144908.

[241] B. Bayramoglu, R. Faller, Coarse-grained modeling of polystyrene in various environments by iterative boltzmann inversion, Macromolecules 45 (2012) 9205–9219.

[242] M.-T. Lee, R. Mao, A. Vishnyakov, A. V. Neimark, Parametrization of chain molecules in dissipative particle dynamics, The Journal of Physical Chemistry B 120 (2016) 4980–4991.

[243] S. Izvekov, B. M. Rice, Multi-scale coarse-graining of non-conservative interactions in molecular liquids, The Journal of Chemical Physics 140 (2014) 104104.

[244] A. Dequidt, J. G. Solano Canchaya, Bayesian parametrization of coarse-grain dissipative dynamics models, The Journal of Chemical Physics 143 (2015) 084122.

[245] I. Santos de Oliveira, B. Fitzgerald, W. K. den Otter, W. J. Briels, Mesoscale modeling of shear-thinning polymer solutions, The Journal of Chemical Physics 140 (2014) 104903.

[246] A. L. Harmat, S. J. Nikkhah, M. Sammalkorpi, Dissipative particle dynamics simulations of h-shaped diblock copolymer self-assembly in solvent, Polymer 233 (2021) 124198.

[247] J. T. Padding, W. J. Briels, Time and length scales of polymer melts studied by coarse-grained molecular dynamics simulations, The Journal of Chemical Physics 117 (2002) 925–943.

[248] P. Posocco, M. Fermeglia, S. Pricl, Morphology prediction of block copolymers for drug delivery by mesoscale simulations, Journal of Materials Chemistry 20 (2010) 7742–7753.

[249] F. Goodarzi, S. Zendehboudi, Effects of salt and surfactant on interfacial characteristics of water/oil systems: molecular dynamic simulations and dissipative particle dynamics, Industrial & Engineering Chemistry Research 58 (2019) 8817–8834.

[250] I. Pagonabarraga, D. Frenkel, Dissipative particle dynamics for interacting systems, The Journal of Chemical Physics 115 (2001) 5015–5026.

[251] P. Warren, Vapor-liquid coexistence in many-body dissipative particle dynamics, Physical Review E 68 (2003) 066702.

[252] P. Espanol, Dissipative particle dynamics with energy conservation, Europhysics Letters 40 (1997) 631.

[253] A. Boromand, S. Jamali, J. M. Maia, Viscosity measurement techniques in dissipative particle dynamics, Computer Physics Communications 196 (2015) 149–160.

[254] A. Chatterjee, Modification to lees–edwards periodic boundary condition for dissipative particle dynamics simulation with high dissipation rates, Molecular Simulation 33 (2007) 1233–1236.

[255] M. Whittle, K. P. Travis, Dynamic simulations of colloids by core-modified dissipative particle dynamics, The Journal of Chemical Physics 132 (2010) 124906.

[256] S. Khani, M. Yamanoi, J. Maia, The lowe-andersen thermostat as an alternative to the dissipative particle dynamics in the mesoscopic simulation of entangled polymers, The Journal of Chemical Physics 138 (2013) 174903.

[257] N. Mai-Duy, N. Phan-Thien, B. C. Khoo, Investigation of particles size effects in dissipative particle dynamics (dpd) modelling of colloidal suspensions, Computer Physics Communications 189 (2015) 37–46.

[258] K. Le-Cao, N. Phan-Thien, B. Khoo, N. Mai-Duy, A dissipative particle dynamics model for thixotropic materials exhibiting pseudo-yield stress behaviour, Journal of Non-Newtonian Fluid Mechanics 241 (2017) 1–13.

[259] L. Zhao, Z. Li, Z. Wang, B. Caswell, J. Ouyang, G. E. Karniadakis, Active-and transfer-learning applied to microscale-macroscale coupling to simulate viscoelastic flows, Journal of Computational Physics 427 (2021) 110069.

[260] J. Zhao, S. Chen, N. Phan-Thien, Rheology of polymers in many-body dissipative particle dynamics simulations: Schmidt number effect, Molecular Simulation 44 (2018) 797–814.

[261] S. Jamali, A. Boromand, S. Khani, J. Wagner, M. Yamanoi, J. Maia, Generalized mapping of multi-body dissipative particle dynamics onto fluid compressibility and the flory-huggins theory, The Journal of Chemical Physics 142 (2015) 164902.

[262] X. Qin, X. Li, W. Wang, Q. Li, T. Wang, L. Cao, J. Piao, S. Chen, Synthesis of poly ethyl acrylate interpenetrated poly methyl acrylate elastomer coating and its corrosion resistance properties, Materials Letters 314 (2022) 131880.

[263] B. Ravikumar, I. K. Karathanassis, T. Smith, M. Gavaises, Dilute viscoelastic polymer solutions for dielectric heat transfer applications: A molecular dynamics study, International Journal of Thermofluids 18 (2023) 100333.

[264] R. C. Krafnick, A. E. García, Efficient schmidt number scaling in dissipative particle dynamics, The Journal of Chemical Physics 143 (2015) 243106.

[265] M. Ripoll, K. Mussawisade, R. Winkler, G. Gompper, Dynamic regimes of fluids simulated by multiparticle-collision dynamics, Physical Review E 72 (2005) 016701.

[266] M. Rubinstein, R. H. Colby, et al., Polymer physics, volume 23, Oxford University Press New York, 2003.

[267] P. J. Flory, Thermodynamics of high polymer solutions, The Journal of Chemical Physics 9 (1941) 660–660.

[268] B. D. Todd, P. J. Daivis, Nonequilibrium molecular dynamics: theory, algorithms and applications, Cambridge University Press, 2017.

[269] G. Giunta, P. Carbone, Cross-over in the dynamics of polymer confined between two liquids of different viscosity, Interface Focus 9 (2019) 20180074.

[270] W. Nowicki, The longitudinal superdiffusive motion of block copolymer in a tight nanopore, Polymers 12 (2020) 2931.

[271] M. Hinczewski, X. Schlagberger, M. Rubinstein, O. Krichevsky, R. R. Netz, End-monomer dynamics in semiflexible polymers, Macromolecules 42 (2009) 860–875.

[272] M. Adam, M. Delsanti, Dynamical properties of polymer solutions in good solvent by rayleigh scattering experiments, Macromolecules 10 (1977) 1229–1237.

[273] L. Jiang, N. Watari, R. G. Larson, How accurate are stochastic rotation dynamics simulations of polymer dynamics?, Journal of Rheology 57 (2013) 1177–1194.

[274] A. Jukic, E. Vidovic, Z. Janovic, Alkyl methacrylate and styrene terpolymers as lubricating oil viscosity index improvers, Chemistry and Technology of Fuels and Oils 43 (2007) 386–394.

[275] J. Wang, Z. Ye, S. Zhu, Topology-engineered hyperbranched high-molecular-weight polyethylenes as lubricant viscosity-index improvers of high shear stability, Industrial & Engineering Chemistry Research 46 (2007) 1174–1178.

[276] N. I. Fisher, Statistical analysis of circular data, Cambridge University Press, 1995.

[277] J. F. Rudzinski, S. Kloth, S. Wörner, T. Pal, K. Kremer, T. Bereau, M. Vogel, Dynamical properties across different coarse-grained models for ionic liquids, Journal of Physics: Condensed Matter 33 (2021) 224001.

[278] K. M. Lebold, W. Noid, Dual approach for effective potentials that accurately model structure and energetics, The Journal of Chemical Physics 150 (2019).

[279] D. Reith, M. Pütz, F. Müller-Plathe, Deriving effective mesoscale potentials from atomistic simulations, Journal of Computational Chemistry 24 (2003) 1624–1636.

[280] K. Zhang, C. W. Manke, Simulation of polymer solutions by dissipative particle dynamics, Molecular Simulation 25 (2000) 157–166.

[281] T. Soddemann, B. Dünweg, K. Kremer, Dissipative particle dynamics: A useful thermostat for equilibrium and nonequilibrium molecular dynamics simulations, Physical Review E 68 (2003) 046702.

[282] Y. Fan, R. I. Tanner, N. Phan-Thien, Fully developed viscous and viscoelastic flows in curved pipes, Journal of Fluid Mechanics 440 (2001) 327–357.

[283] M. Norouzi, M. Kayhani, C. Shu, M. Nobari, Flow of second-order fluid in a curved duct with square cross-section, Journal of Non-Newtonian Fluid Mechanics 165 (2010) 323–339.

[284] S. Saha, M. Alam, Normal stress differences, their origin and constitutive relations for a sheared granular fluid, Journal of Fluid Mechanics 795 (2016) 549–580.

[285] T. Schweizer, Measurement of the first and second normal stress differences in a polystyrene melt with a cone and partitioned plate tool, Rheologica acta 41 (2002) 337–344.

[286] D. Heyes, D. Dini, E. Smith, Viscuit and the fluctuation theorem investigation of shear viscosity by molecular dynamics simulations: The information and the noise, The Journal of Chemical Physics 154 (2021).

[287] C. Lindsey, G. Patterson, Detailed comparison of the williams–watts and cole–davidson functions, The Journal of Chemical Physics 73 (1980) 3348–3357.

[288] T. Curk, Dissipative particle dynamics for coarse-grained models, The Journal of Chemical Physics 160 (2024).

[289] Y. Wang, R. Hernandez, Construction of multiscale dissipative particle dynamics (dpd) models from other coarse-grained models, ACS omega 9 (2024) 17667–17680.

[290] R. S. Mukkamala, M. J. Hore, Simulation and analysis of molecular bottlebrush dynamics in dilute solutions, Macromolecules 57 (2024) 445–455.

[291] T. Tan, L. Rennels, B. Parthum, The social costs of hydrofluorocarbons and the benefits from their expedited phase-down, Nature Climate Change 14 (2024) 55–60.

[292] A. Woodcock, Hydrofluorocarbons, climate, and health—moving the montreal protocol beyond ozone-layer recovery, New England Journal of Medicine 388 (2023) 2404–2406.

[293] S. Gota, C. Huizenga, K. Peet, N. Medimorec, S. Bakker, Decarbonising transport to achieve paris agreement targets, Energy Efficiency 12 (2019) 363–386.

[294] G. Baysset, P. Chessé, D. Chalet, A. Lefebvre, Optimal hev cooling system design through a computer-aided virtual development chain, Proceedings of the Institution of Mechanical Engineers, Part D: Journal of Automobile Engineering 237 (2023) 655–667.

[295] C. Piao, T. Chen, A. Zhou, P. Wang, J. Chen, Research on electric vehicle cooling system based on active and passive liquid cooling, in: Journal of Physics: Conference Series, volume 1549, IOP Publishing, 2020, p. 042146. doi:10.1088/1742-6596/1549/4/042146.

[296] T. Wang, K. Tseng, J. Zhao, Z. Wei, Thermal investigation of lithium-ion battery module with different cell arrangement structures and forced air-cooling strategies, Applied Energy 134 (2014) 229–238.

[297] X. Cui, J. Wang, G. Xia, Enhanced thermal conductivity of nanofluids by introducing janus particles, Nanoscale 14 (2022) 99–107.

[298] S. U. S. Choi, J. A. Eastman, Enhancing thermal conductivity of fluids with nanoparticles, Technical Report, Argonne National Lab.(ANL), Argonne, IL (United States), 1995.

[299] D. Wen, Y. Ding, Experimental investigation into convective heat transfer of nanofluids at the entrance region under laminar flow conditions, International journal of heat and mass transfer 47 (2004) 5181–5188.

[300] S. Z. Heris, S. G. Etemad, M. N. Esfahany, Experimental investigation of oxide nanofluids laminar flow convective heat transfer, International Communications in Heat and Mass Transfer 33 (2006) 529–535.

[301] T. T. Baby, S. Ramaprabhu, Experimental investigation of the thermal transport properties of a carbon nanohybrid dispersed nanofluid, Nanoscale 3 (2011) 2208–2214.

[302] B. T. Branson, P. S. Beauchamp, J. C. Beam, C. M. Lukehart, J. L. Davidson, Nanodiamond nanofluids for enhanced thermal conductivity, Acs Nano 7 (2013) 3183–3189.

[303] P. Maheshwary, C. Handa, K. Nemade, A comprehensive study of effect of concentration, particle size and particle shape on thermal conductivity of titania/water based nanofluid, Applied Thermal Engineering 119 (2017) 79–88.

[304] Y. Yang, Z. G. Zhang, E. A. Grulke, W. B. Anderson, G. Wu, Heat transfer properties of nanoparticle-in-fluid dispersions (nanofluids) in laminar flow, International Journal of Heat and Mass Transfer 48 (2005) 1107–1116.

[305] B. Salman, H. Mohammed, K. Munisamy, A. S. Kherbeet, Characteristics of heat transfer and fluid flow in microtube and microchannel using conventional fluids and nanofluids: a review, Renewable and Sustainable Energy Reviews 28 (2013) 848–880.

[306] A. Senatore, V. D'Agostino, V. Petrone, P. Ciambelli, M. Sarno, Graphene oxide nanosheets as effective friction modifier for oil lubricant: materials, methods, and tribological results, ISRN Tribology 2013 (2013) 1–9.

[307] Z. Cai, M. Tian, G. Zhang, Experimental study on the flow and heat transfer of graphene-based lubricants in a horizontal tube, Processes 8 (2020) 1675.

[308] S. Aberoumand, A. Jafarimoghaddam, Experimental study on synthesis, stability, thermal conductivity and viscosity of cu–engine oil nanofluid, Journal of the Taiwan Institute of Chemical Engineers 71 (2017) 315–322.

[309] S. Alosious, S. K. Kannam, S. P. Sathian, B. Todd, Nanoconfinement effects on the kapitza resistance at water–cnt interfaces, Langmuir 37 (2021) 2355–2361.

[310] T.-K. Hong, H.-S. Yang, C. Choi, Study of the enhanced thermal conductivity of fe nanofluids, Journal of Applied Physics 97 (2005).

[311] J. C. Maxwell, A treatise on electricity and magnetism, volume 1, Clarendon press, 1873.

[312] R. Hamilton, O. Crosser, Thermal conductivity of heterogeneous two-component systems, Industrial & Engineering chemistry fundamentals 1 (1962) 187–191.

[313] R. H. Davis, The effective thermal conductivity of a composite material with spherical inclusions, International Journal of Thermophysics 7 (1986) 609–620.

[314] S.-Y. Lu, H.-C. Lin, Effective conductivity of composites containing aligned spheroidal inclusions of finite conductivity, Journal of Applied Physics 79 (1996) 6761–6769.

[315] W. Yu, S. U. S. Choi, The role of interfacial layers in the enhanced thermal conductivity of nanofluids: a renovated maxwell model, Journal of Nanoparticle Research 5 (2003) 167–171.

[316] S. P. Jang, S. U. S. Choi, Role of brownian motion in the enhanced thermal conductivity of nanofluids, Applied Physics Letters 84 (2004) 4316–4318.

[317] J. Guo, Y. Zhao, B. Sun, P. Wang, Z. Wang, H. Dong, Research progress of nano copper lubricant additives on engineering tribology, Metals 11 (2021) 2006.

[318] G. R. Kannan, R. Karvembu, R. J. A. E. Anand, Effect of metal based additive on performance emission and combustion characteristics of diesel engine fuelled with biodiesel, Applied Energy 88 (2011) 3694–3703.

[319] G. Bree, D. Horstman, C. T. J. Low, Light-weighting of battery casing for lithium-ion device energy density improvement, Journal of Energy Storage 68 (2023) 107852.

[320] K. Elsaid, M. A. Abdelkareem, H. M. Maghrabie, E. T. Sayed, T. Wilberforce, A. Baroutaji, A. Olabi, Thermophysical properties of graphene-based nanofluids, International Journal of Thermofluids 10 (2021) 100073.

[321] Y.-K. Kwon, P. Kim, Unusually high thermal conductivity in carbon nanotubes, High Thermal Conductivity Materials (2006) 227–265.

[322] I.-C. Yeh, M. L. Berkowitz, Ewald summation for systems with slab geometry, The Journal of Chemical Physics 111 (1999) 3155–3162.

[323] S. Assadi, M. Kalteh, M. Bagheri Motlagh, Investigating convective heat transfer coefficient of nanofluid couette flow in a nanochannel by molecular dynamics simulation, Molecular Simulation 48 (2022) 702–711.

[324] L. Lindsay, D. Broido, Optimized tersoff and brenner empirical potential parameters for lattice dynamics and phonon thermal transport in carbon nanotubes and graphene, Physical Review B 81 (2010) 205441.

[325] S. Foiles, M. Baskes, M. S. Daw, Embedded-atom-method functions for the fcc metals cu, ag, au, ni, pd, pt, and their alloys, Physical Review B 33 (1986) 7983.

[326] T. Luo, J. R. Lloyd, Enhancement of thermal energy transport across graphene/graphite and polymer interfaces: a molecular dynamics study, Advanced Functional Materials 22 (2012) 2495–2502.

[327] P. Erhart, K. Albe, Analytical potential for atomistic simulations of silicon, carbon, and silicon carbide, Physical Review B 71 (2005) 035211.

[328] X.-Y. Shen, M. Hekmatifar, M. Y. A. Shukor, A. a. Alizadeh, Y.-L. Sun, D. Toghraie, R. Sabetvand, Molecular dynamics simulation of water-based ferro-nanofluid flow in the microchannel and nanochannel: Effects of number of layers and material of walls, Journal of Molecular Liquids 338 (2021) 116924.

[329] K. Anitha, S. Namsani, J. K. Singh, Removal of heavy metal ions using a functionalized single-walled carbon nanotube: a molecular dynamics study, The Journal of Physical Chemistry A 119 (2015) 8349–8358.

[330] L. Wang, J. Jin, P. Yang, Y. Zong, Q. Peng, Graphene adhesion mechanics on iron substrates: insight from molecular dynamic simulations, Crystals 9 (2019) 579.

[331] X. He, Q. Bai, R. Shen, Atomistic perspective of how graphene protects metal substrate from surface damage in rough contacts, Carbon 130 (2018) 672–679.

[332] J. Tersoff, Modeling solid-state chemistry: Interatomic potentials for multicomponent systems, Physical Review B 39 (1989) 5566.

[333] L. A. Girifalco, M. Hodak, R. S. Lee, Carbon nanotubes, buckyballs, ropes, and a universal graphitic potential, Physical Review B 62 (2000) 13104.

[334] K. Kanhaiya, S. Kim, W. Im, H. Heinz, Accurate simulation of surfaces and interfaces of ten fcc metals and steel using lennard–jones potentials, npj Computational Materials 7 (2021) 17.

[335] L. Wu, B. Song, L. M. Keer, L. Gu, Molecular dynamics investigation of graphene nanoplate diffusion behavior in poly-α-olefin lubricating oil, Crystals 8 (2018) 361.

[336] X. Dou, A. R. Koltonow, X. He, H. D. Jang, Q. Wang, Y.-W. Chung, J. Huang, Self-dispersed crumpled graphene balls in oil for friction and wear reduction, Proceedings of the National Academy of Sciences 113 (2016) 1528–1533.

[337] L. Zhang, Y. Jing, P. Qu, W. Wang, X. Yao, L. Tian, Effect of microstructure of nanoparticles and surrounding alcohol groups on energy transfer efficiency, Applied Thermal Engineering 215 (2022) 119031.

[338] A. W. Kuziel, K. Z. Milowska, P.-L. Chau, S. Boncel, K. K. Koziol, N. Yahya, M. C. Payne, The true amphipathic nature of graphene flakes: a versatile 2d stabilizer, Advanced Materials 32 (2020) 2000608.

[339] M. P. Allen, D. J. Tildesley, Computer simulation of liquids, Oxford university press, 2017.

[340] A. Mohebbi, Prediction of specific heat and thermal conductivity of nanofluids by a combined equilibrium and non-equilibrium molecular dynamics simulation, Journal of Molecular Liquids 175 (2012) 51–58.

[341] C. Caleman, P. J. Van Maaren, M. Hong, J. S. Hub, L. T. Costa, D. Van Der Spoel, Force field benchmark of organic liquids: density, enthalpy of vaporization, heat capacities, surface tension, isothermal compressibility, volumetric expansion coefficient, and dielectric constant, Journal of Chemical Theory and Computation 8 (2012) 61–74.

[342] D. Baird, J. Ferentinos, Application of mil-c-87252 in f-22 liquid cooling system, SAE transactions (1998) 247–259.

[343] T. Singh, I. W. Almanassra, T. Al-Ansari, G. McKay, M. A. Atieh, Performance investigation of graphene oxide-based water/oil nanofluids for high pressure and high temperature solar thermal technologies for sustainable energy systems, FlatChem 35 (2022) 100420.

[344] J. Hone, Phonons and Thermal Properties of Carbon Nanotubes, Springer Berlin Heidelberg, Berlin, Heidelberg, 2001, pp. 273–286. doi:10.1007/3-540-39947-X_11.

[345] M. F. Pakdaman, M. Akhavan-Behabadi, P. Razi, An experimental investigation on thermo-physical properties and overall performance of mwcnt/heat transfer oil nanofluid flow inside vertical helically coiled tubes, Experimental thermal and fluid science 40 (2012) 103–111.

[346] J. A. Narvaez, Thermal conductivity of poly-alpha-olefin (pao)-based nanofluids, Master's thesis, University of Dayton, 2010.

[347] E. Pop, V. Varshney, A. K. Roy, Thermal properties of graphene: Fundamentals and applications, MRS bulletin 37 (2012) 1273–1281.

[348] J. Lan, B. Li, Thermal rectifying effect in two-dimensional anharmonic lattices, Physical Review B 74 (2006) 214305.

[349] J. Chen, G. Zhang, B. Li, Tunable thermal conductivity of si1- xgex nanowires, Applied Physics Letters 95 (2009).

[350] P. Ptasinski, B. Boersma, F. Nieuwstadt, M. Hulsen, B. Van den Brule, J. Hunt, Turbulent channel flow near maximum drag reduction: simulations, experiments and mechanisms, Journal of Fluid Mechanics 490 (2003) 251–291.

[351] H. Li, Y. Zhu, M. Chu, H.-K. Dong, G. Zhang, Thermal conductivity of irregularly shaped nanoparticles from equilibrium molecular dynamics, Journal of Physics: Condensed Matter (2024).

[352] G. Li, H. Sun, D. Han, S. Cheng, G. Zhao, Y. Guo, Applying machine learning to reveal the microscopic heat transfer mechanism of nanofluids as coolants, Thermochimica Acta (2024) 179788.

[353] C. Chen, L. Zhuang, X. Li, J. Dong, J. Lu, A many-body dissipative particle dynamics study of forced water–oil displacement in capillary, Langmuir 28 (2012) 1330–1336.

[354] Y. Xia, J. Goral, H. Huang, I. Miskovic, P. Meakin, M. Deo, Many-body dissipative particle dynamics modeling of fluid flow in fine-grained nanoporous shales, Physics of Fluids 29 (2017) 056601.

[355] P. Español, Dissipative particle dynamics for a harmonic chain: A first-principles derivation, Physical Review E 53 (1996) 1572.

[356] X. Yong, Hydrodynamic interactions and entanglements of polymer solutions in many-body dissipative particle dynamics, Polymers 8 (2016) 426.

Appendix A

Force-field

L-OPLS-AA [19, 173, 174] force-field of the following generic form is used in this simulation to model the interactions:

$$
\begin{aligned}
V(r) = & \sum_{bonds} k_b (b - b_0)^2 \\
& + \sum_{angles} k_\theta (\theta - \theta_0)^2 \\
& + \sum_{dihedrals} \sum_{n=1}^{4} k_\phi (1 + (-1)^{n-1} \cos(n\phi)) \\
& + \sum_{vdW} 4\varepsilon_{ij} \left[\left(\frac{\sigma_{ij}}{r_{ij}} \right)^{12} - \left(\frac{\sigma_{ij}}{r_{ij}} \right)^{6} \right] \\
& + \sum_{Coulomb} \frac{q_i q_j}{\varepsilon_0 r_{ij}}.
\end{aligned}
\tag{A1}
$$

Here, the terms 1 to 4 on the right-hand side computes the bonded interaction energies due to bond stretching, bending, twisting, and out-of-plane torsions. The last two terms compute the interactions due to van der Waals's forces and electrostatics. The following tables show the different parameters used.

Table A1: Bonding parameters used in term 1 in Equation A1.

Bond	k_b (kcal mol^{-1}Å^{-2})	b_0 (Å)
C-C	268	1.529
C-H	340	1.090

Table A2: Angle parameters used in term 2 in Equation A1.

Angle	k_θ (kcal mol^{-1}rad^{-2})	θ_0 (deg)
C-C-H	37.50	110.7
H-C-H	33.00	107.8
C-C-C	58.35	112.7

Table A3: Dihedral parameters used in term 3 in Equation A1.

Dihedral	$k_{\phi 1}$ (kcal mol^{-1})	$k_{\phi 2}$ (kcal mol^{-1})	$k_{\phi 3}$ (kcal mol^{-1})	$k_{\phi 4}$ (kcal mol^{-1})
C-C-C-C	0.6446926386	-0.2143420172	0.1782194073	0.0000
H-C-C-H	0.0000	0.0000	0.3000	0.0000
C-C-C-H	0.0000	0.0000	0.3000	0.0000
C-C$_{CH}$-C-C	1.3000	-0.0500	0.2000	0.0000
C$_{CH}$-C-C-C	1.3000	-0.0500	0.2000	0.0000
C-C$_{CH}$-C$_{CH}$-C	1.3000	-0.0500	0.2000	0.0000
C$_{CH}$-C$_{CH}$-C -C	1.3000	-0.0500	0.2000	0.0000

Table A4: LJ parameters and partial charges of the atoms used in terms 4 and 5 in Equation A1.

Atom type	ε_{ii} (kcal mol^{-1})	σ_{ii} (Å)	q_i (e$^-$)
C$_{CH_3}$	0.066	3.5	-0.222
C$_{CH_2}$	0.066	3.5	-0.148
C$_{CH}$	0.066	3.5	-0.060
H$_{CH_3}$	0.030	2.5	0.074
H$_{CH_2}$	0.026	2.5	0.074
H$_{CH}$	0.030	2.5	0.060

Radial distribution function

The pairwise radial distribution function $g_{o,p}(r)$ is computed using the equation

$$g_{o,p}(r) = \frac{n(r)}{4\pi\rho_{n,p}r^2\delta r} \tag{A2}$$

where $n(r)$ is the number of p atoms, with a number density $\rho_{n,p}$ in the simulation box, present in a spherical shell of thickness δr from the central atom o.
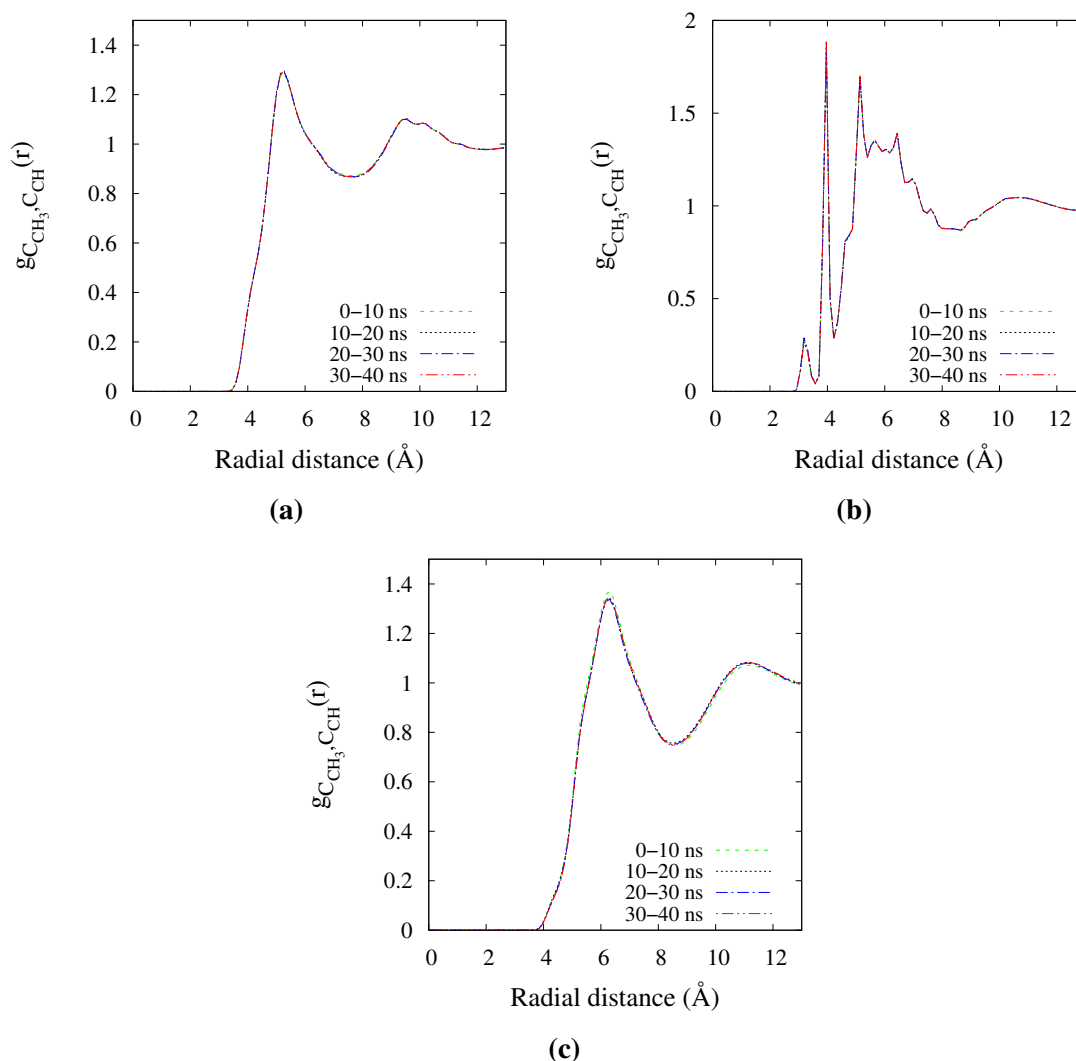

Figure A1: The radial distribution functions $g_{o,p}(r)$ of (a) C_{CH_3}-C_{CH_3} pair (b) C_{CH_3}-C_{CH_2} pair and (c) C_{CH_3}-C_{CH} pair in the solvent system computed from the data in the consequent windows of 10 ns during the production run of a simulation at 293 K. The overlapping radial distribution functions show that the system is well equilibrated.

Simulated density values
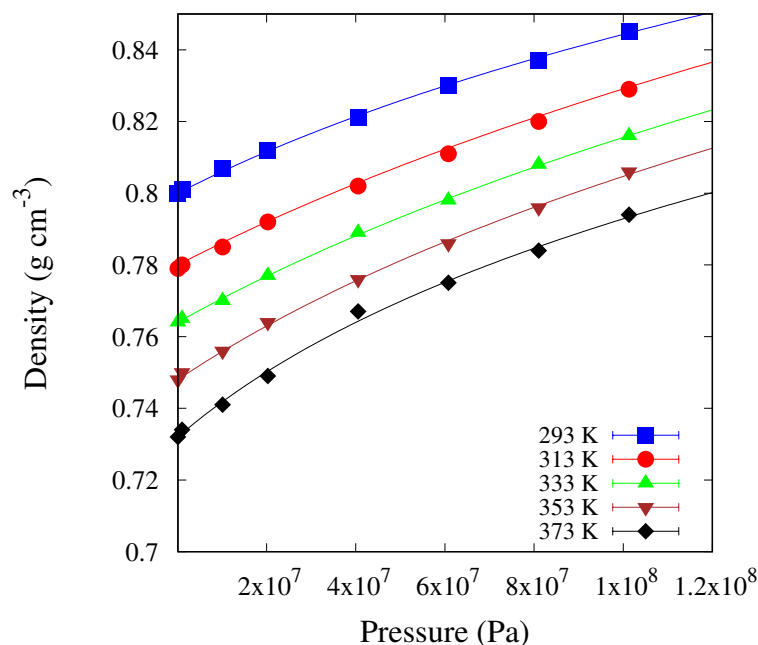
Figure A2: The density (ρ) of pure solvent (PAO-2) as a function of pressure at different temperatures. The points show the simulated data, and the lines show the modified Tait equation fit as described in Equation 2.2 in Chapter 2.

Experimental determination of density and isothermal compressibility

The density and the isothermal compressibility are determined by use of a high precision piston- cylinder system made of INVAR steel. In a first step the density is determined as a function of temperature at atmospheric pressure according to DIN EN ISO 1183 by use of a hydrostatic balance in accordance to the principle of Archimedes. The typical accuracy of this instrument is higher than +/- 0.2 per mille. In a second step the piston-cylinder system is used in order to determine the density as a function of pressure. The principle of this instrument is the following: The piston-cylinder system will be filled with the testing fluid; during the isothermal measurement of the density as a function of pressure the mass of the sample remains constant while the volume is varied according to the applied pressure. The variation of the volume is transformed into the movement of the piston which is measured by a highly sensitive

Table A5: Experimental density (ρ_0) and isothermal compressibility (κ_T) of pure solvent systems at various temperatures.

Temperature (K)	Density (g cm^{-3})	$\kappa_T \times 10^{11}$(Pa^{-1})
293	0.793	79.55
313	0.780	89.98
333	0.766	101.70
353	0.752	115.22

Table A6: Simulated density (ρ_0) and isothermal compressibility (κ_T) of the polymer solution at various temperatures.

Temperature (K)	Density (g cm^{-3})	$\kappa_T \times 10^{11}$(Pa^{-1})
293	0.808	68.21
313	0.791	80.09
333	0.774	88.09
353	0.765	92.25
373	0.753	112.5

differential transformer system. The typical accuracy of this instrument is higher than +/- 0.5 per mille.

From the experimental values obtained, density is modelled using the following empirical relationship:

$$\rho(\text{p},\text{T}) = \frac{\rho(\text{T})}{1 - 0.0902 \, ln \frac{5348.3 - 23.93\text{T} + 0.0396\text{T}^2 - 2.39 \times 10^{-5}\text{T}^3 + \text{p}}{5348.3 - 23.93\text{T} + 0.0396\text{T}^2 - 2.39 \times 10^{-5}\text{T}^3}}. \tag{A3}$$

Subsequently, the isothermal compressibility is obtained using the equation

$$\kappa_T = \frac{0.0902\rho(\text{p},\text{T})}{(5348.3 - 23.93\text{T} + 0.0396\text{T}^2 - 2.39 \times 10^{-5}\text{T}^3 + \text{p})\rho(\text{T})}. \tag{A4}$$

Transport properties
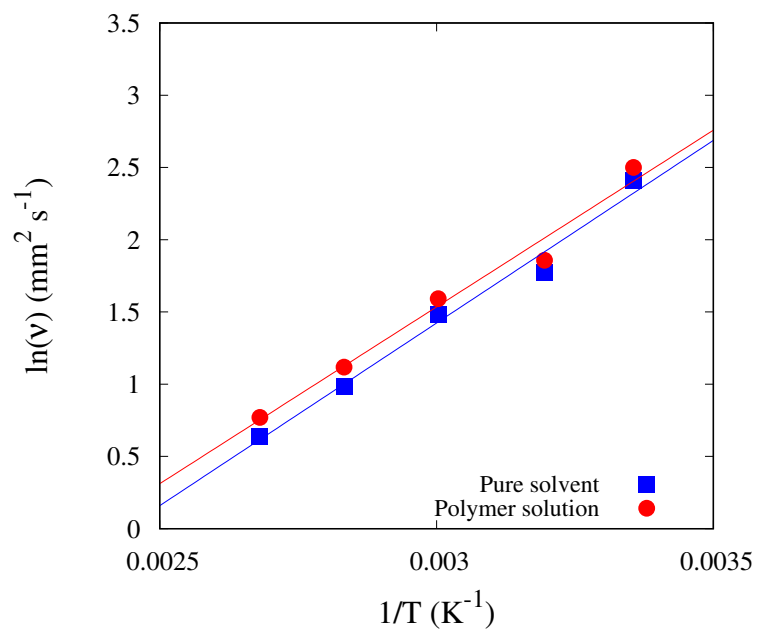
Figure A3: The kinematic viscosity (ν_0) of the pure solvent system and polymer solution as a function of temperature. The closed symbols show the simulated values - blue (pure solvent) and red (polymer solution). The lines show the Arrhenius fit as described in Equation 2.6 in Chapter 2.
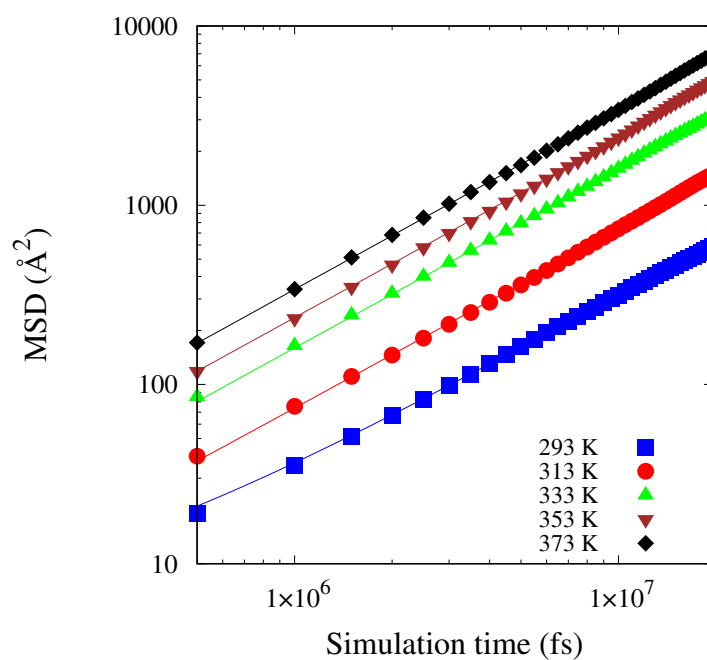
Figure A4: Mean squared displacement (MSD) of the PAO-2 molecules in pure solvent system as a function of simulation time for a single simulation run at different temperatures using multiple time origins. The closed symbols show the simulated MSD values. The lines show the fits of linear functions whose slope is used to compute the centre of mass self-diffusion coefficient, D_{COM}.
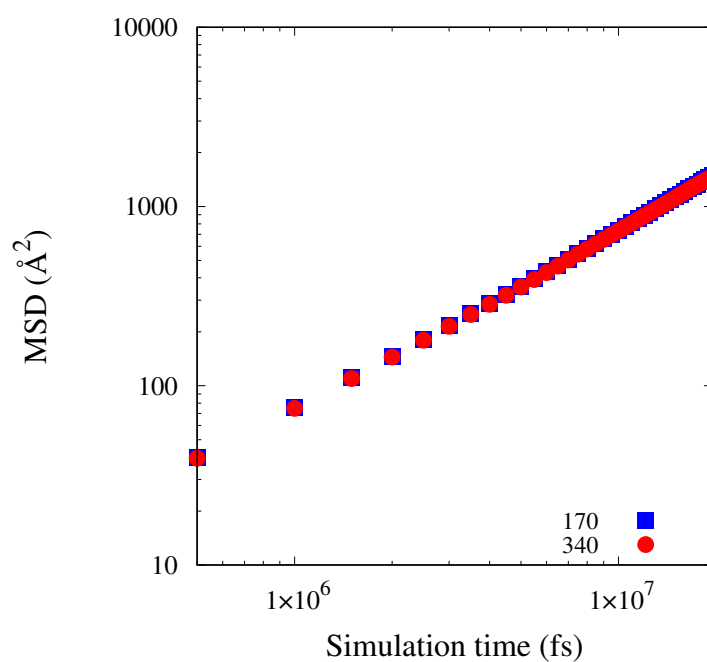
Figure A5: MSD of the PAO-2 molecules in pure solvent as a function of simulation time for a single simulation run at 313 K using multiple time origins. The closed symbols show the simulated values - blue (170 molecules) and red (340 molecules). The computed MSD shows that it is independent of the system size and the trajectories evolve similarly over time.

Table A7: Comparison of zero-shear dynamic viscosity (η_0) of pure solvent and polymer solution systems from equilibrium MD (Green-Kubo method) and NEMD (Carreau-model fitting).

| Pure solvent		
Temperature (K)	Green-Kubo (Pa s)	Carreau-model (Pa s)
293	0.0088	0.009
313	0.0044	0.0048
333	0.0033	0.0033
353	0.0020	0.0021
373	0.0014	0.0013
Polymer solution		
Temperature (K)	Green-Kubo (Pa s)	Carreau-model (Pa s)
293	0.0093	0.0130
313	0.0051	0.0065
333	0.0035	0.0039
353	0.0023	0.0025
373	0.0016	0.0017
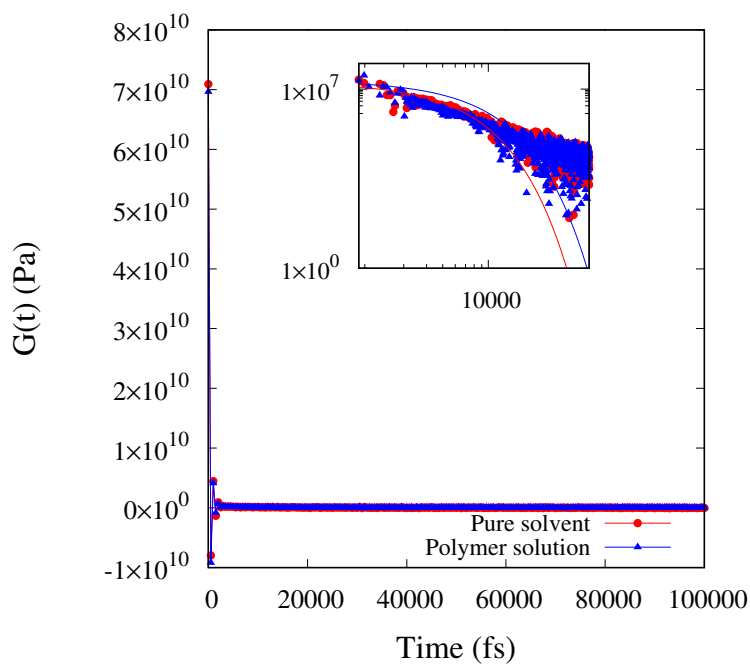
Figure A6: $G(t)$ as a function of simulation time for pure solvent and polymer solution systems at 313 K. Inset shows $G(t)$ values (points) smoothened by doing a running average between 0.9t and 1.1t as described by Sen et al. [200], and their corresponding fits (lines) of Equation 2.13 in Chapter 2.

Structural characterisation
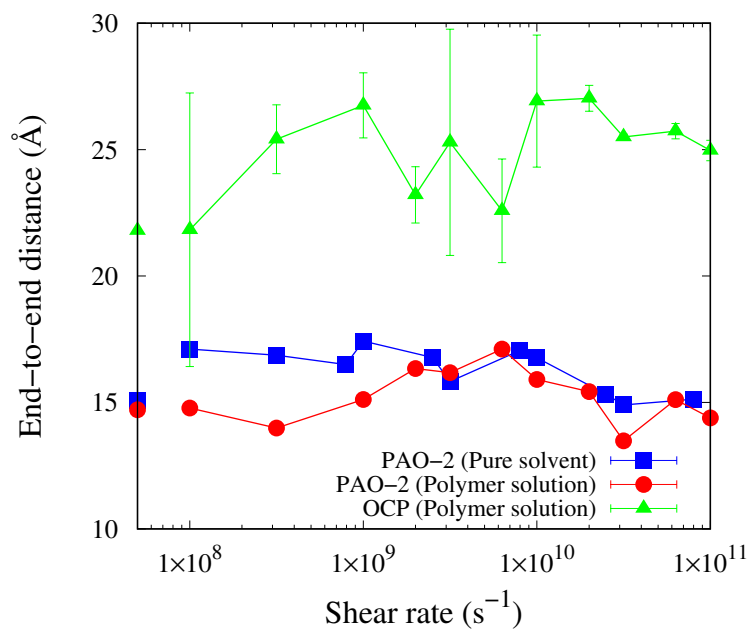
Figure A7: The end-to-end distance (R_e) of PAO-2 and OCP in pure solvent and polymer solution as a function of shear rate at 313 K. The data points on the y-axis show the values of R_e at zero shear rate. The data shows that R_e of OCP increases as a function of shear rate whereas that of PAO-2 remains constant.

Terminal relaxation time
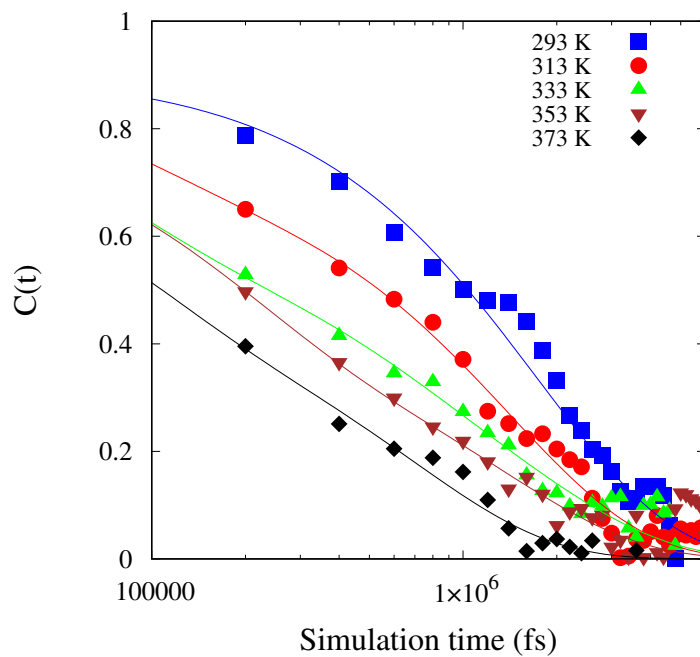
Figure A8: The end-to-end vector autocorrelation ($C(t)$) of OCP as a function of simulation time for a single simulation run of polymer solution at different temperatures. The closed symbols show the simulated $C(t)$ values. The lines show the a fit of a sum of exponential function as described by Equation 2.18 in Chapter 2.

Appendix B

Basics of mDPD modelling

The force-field of mDPD is composed of three different interactions. A conservative force that is repulsive in nature, a dissipative force that introduces a viscous component into the system and a random force compensating the excess dissipation. The basis of the model is the Langevin equation. Here, the force between two mesoscale beads i and j,

$$\mathbf{F}_{ij} = \sum_{j \neq i} (F_{ij}^C + F_{ij}^D + F_{ij}^R) \tag{B1}$$

where F_{ij}^C is the conservative force, F_{ij}^D is the dissipative force, and F_{ij}^R is the random force. The conservative force is modelled as

$$F_{ij}^C = (A_{ij}\omega^C(r_{ij}) + B_{ij}(\bar{\rho}_i + \bar{\rho}_j)\omega^d(r_{ij}))\hat{\mathbf{r}}_{ij}. \tag{B2}$$

Here, the first term controls the long-range attractive interactions that are dependent on the system density, ρ within a cut-off radius of r_C. The second term controls the short-range repulsion forces that depend upon the weighted average of the local densities, $\bar{\rho}_i$ and $\bar{\rho}_j$ within a cut-off radius of r_d. This formulation distinguishes mDPD from the standard DPD model [123]. In the equation, r_{ij} represents the distance and $\hat{\mathbf{r}}_{ij}$ is the unit displacement vector between particles i and j. The dissipative force is modelled as

$$F_{ij}^D = -\gamma_{ij}\omega^D(r_{ij})(\hat{\mathbf{r}}_{ij} \cdot \mathbf{v}_{ij})\hat{\mathbf{r}}_{ij} \tag{B3}$$

with $\mathbf{v}_{ij} = \mathbf{v}_i - \mathbf{v}_j$ representing the velocity difference between particles i and j. The force is computed within a cut-off radius of r_D (not to be confused with r_d). The random force is modelled as

$$F_{ij}^R = \sigma_{ij}\omega^R(r_{ij})\zeta_{ij}\hat{\mathbf{r}}_{ij} \tag{B4}$$

where σ_{ij} defines the strength of the random force applied and ζ_{ij} is a Gaussian random variable. The weight functions in equations Equation B3 and Equation B4 are linked via the fluctuation-dissipation theorem such that

$$\omega^R(r_{ij}) = \sqrt{\omega^D(r_{ij})} = \begin{cases} \left(1 - \frac{r_{ij}}{r_D}\right) & r_{ij} \leq r_D, \\ 0 & r_{ij} > r_D. \end{cases} \tag{B5}$$

Similarly, the conservative weight parameter of A_{ij} is defined as

$$\omega^C(r_{ij}) = \begin{cases} \left(1 - \frac{r_{ij}}{r_C}\right) & r_{ij} \leq r_C, \\ 0 & r_{ij} > r_C. \end{cases} \tag{B6}$$

In DPD as well as traditional mDPD, $r_C = r_D$, simplifying the modelling parameters. However, in our work we follow the example of Rao et al.[125] and r_D is modelled separately as explained in the next section. Coming to the short-range repulsive interactions defined by B_{ij}, the weight parameter $\omega^d(r_{ij})$ is computed as

$$\omega^d(r_{ij}) = \begin{cases} \frac{15}{2\pi r_d^3} \left(1 - \frac{r_{ij}}{r_d}\right)^2 & r_{ij} \leq r_d, \\ 0 & r_{ij} > r_d. \end{cases} \tag{B7}$$

In this work, r_d is treated as equal to $0.75 r_C$, as seen in the literature [353, 354].

Additional modelling details

In other words,

$$V_{bonded} = V_{FENE} + V_{angle} \tag{B8}$$

where

$$V_{FENE} = \begin{cases} -0.5 k_f r_0^2 ln \left(1 - \left(\frac{r_{ij}}{r_0}\right)^2\right) & 0 \leq r_{ij} \leq r_0, \\ 0 & r_{ij} > r_0, \end{cases} \tag{B9}$$

and

$$V_{angle} = k_{angle}(1 + cos(\theta)). \tag{B10}$$

Here, k_f is the FENE bond energy while k_{angle} is the angle stiffness energy. Also, r_0 is the equilibrium bond distance between the monomeric beads and θ is the equilibrium angle formed between three of the monomeric beads. In literature, bonded interactions of polymers are also

handled by a simple spring force in mesoscale simulations [355, 356]. However, given that the polymer chains showcase elasticity akin to FENE interactions in dilute concentrations, we have decided to retain the specific modelling approach. This ensures the utility of the model for a wide range of polymer solutions exhibiting viscoelastic behaviour. The initial values of k_{angle} of the different polymer chains are derived from the work of Everaers et al[121]. Additionally, the polymer chains are prevented from chain-crossing by adding a segmental-repulsive potential such that

$$F_{ij}^{SRP} = \begin{cases} F_0 \left(1 - \dfrac{R}{R_c}\right) \hat{\mathbf{R}}_{mn} & R < R_c, \\ 0 & R \geq R_c, \end{cases} \tag{B11}$$

where R and $\hat{\mathbf{R}}_{mn}$ are the distance and unit vector between two bonds m and n, respectively. Moreover, F_0 value is set as 100, and R_c is set as 1.5 for all the simulations.

Atomistic molecular dynamics simulation

L-OPLS-AA [19, 173, 174] force-field of the following generic form is used in this simulation to model the interactions:

$$
\begin{aligned}
V(r) = & \sum_{bonds} k_b (b - b_0)^2 \\
& + \sum_{angles} k_\theta (\theta - \theta_0)^2 \\
& + \sum_{dihedrals} \sum_{n=1}^{4} k_\phi (1 + (-1)^{n-1} \cos(n\phi)) \\
& + \sum_{impropers} K_\phi (1 + d \cos(n\phi)) \\
& + \sum_{vdW} 4\varepsilon_{ij} \left[\left(\frac{\sigma_{ij}}{r_{ij}}\right)^{12} - \left(\frac{\sigma_{ij}}{r_{ij}}\right)^{6} \right] \\
& + \sum_{Coulomb} \frac{q_i q_j}{\varepsilon_0 r_{ij}}.
\end{aligned}
\tag{B12}
$$

Here, the terms 1 to 4 on the right-hand side computes the bonded interaction energies due to bond stretching, bending, twisting, and out-of-plane torsions. The last two terms compute the interactions due to van der Waals forces and electrostatics. The following tables show the different parameters used [173, 175, 176, 174, 177].

Table B1: Bonding parameters used in term 1 in Equation B12.

Bond	k_b (kcal mol^{-1}Å^{-2})	b_0 (Å)
C-C	268	1.529
C-H	340	1.090
=C-O	214	1.327
C=O	570	1.229
=C-C	317	1.522
C-O	320	1.410

The pure PAO-2 solvent simulation box is created using 170 molecules of 9,10-dimethyl-octadecane [179]. The OCP polymer chain studied here is made up of 50 mole percent of ethylene (C2) monomers and 50 mole percent propylene (C3) monomers with a molecular mass of 3016 g mol^{-1}. The polymer of this particular weight and chain size is chosen as it provides low relaxation times representative of weakly viscoelastic liquids. The chain consists of 43 molecules each of C2 and C3 monomers with the two ends of the chain terminated using hydrogen atoms. Similarly, the PMA polymer chain consists of 86 monomers of dodecyl methacrylate ($C_{16}H_{30}O_2$). We use Nosé-Hoover thermostat to maintain the temperatures at various stages of the equilibrium MD. The corresponding barostat as implemented by LAMMPS is used to set the pressures. The distance cut-off for van der Waals interactions is set to 13 Å. A faster Ewald summation methodology called particle-particle-particle-mesh (PPPM) is used to compute the long-range electrostatic interactions. Velocity Verlet algorithm is used to integrate the equations of motion with a time-step of 1 fs.

1-4 intra-molecular non-bonded pairwise interactions are given a weight of 0.5 for pure solvent simulations, whereas it is switched-off in case of the simulations of polymer solutions. Energy minimization and equilibration under NPT is carried out for 20 ns after which a production run of 40 ns under NVT ensemble. The system after the 40 ns run is utilised for NEMD simulations. A Lees-Edwards boundary condition is applied to ensure stability of the system [195, 196]. We use SLLOD equations of motion to solve for the trajectories of the atoms [51].

Table B2: Angle parameters used in term 2 in Equation B12.

Angle	k_θ (kcal mol^{-1}rad^{-2})	θ_0 (deg)
C-C-H	37.50	110.7
H-C-H	33.00	107.8
C-C-C	58.35	112.7
C-C=O	80.00	120.4
=C-O-C	81.00	111.4
O=C-O	83.00	123.4
=C-C-C	63.00	111.1
O-C-C	50.00	109.5
=C-C-H	35.00	109.5
O-C-H	35.0	109.5
O-C$_{||}$-C	83.0	116.9

Table B3: Dihedral parameters used in term 3 in Equation B12.

Dihedral	$k_{\phi1}$ (kcal mol^{-1})	$k_{\phi2}$ (kcal mol^{-1})	$k_{\phi3}$ (kcal mol^{-1})	$k_{\phi4}$ (kcal mol^{-1})
C-C-C-C	0.6446926386	-0.2143420172	0.1782194073	0.0000
H-C-C-H	0.0000	0.0000	0.3000	0.0000
C-C-C-H	0.0000	0.0000	0.3000	0.0000
C-C$_{CH}$-C-C	1.3000	-0.0500	0.2000	0.0000
C$_{CH}$-C-C-C	1.3000	-0.0500	0.2000	0.0000
C-C$_{CH}$-C$_{CH}$-C	1.3000	-0.0500	0.2000	0.0000
C$_{CH}$-C$_{CH}$-C-C	1.3000	-0.0500	0.2000	0.0000
O=C-C-C	0.0000	0.0000	0.0000	0.0000
O=C-C-H	0.0000	0.0000	0.0000	0.0000
O-C$_{||}$-C-C	0.0000	0.0000	-0.553	0.0000
O-C$_{||}$-C-H	0.0000	0.0000	0.1320	0.0000
C-O-C=O	0.0000	5.1240	0.0000	0.0000
C-O-C$_{||}$-C	4.6690	5.1240	0.0000	0.0000
=C-C-C-C	-2.0600	-0.3130	0.3150	0.0000
=C-C-C-H	0.0000	0.0000	-0.1000	0.0000
H-C-C-O	0.0000	0.0000	0.4680	0.0000
C-C-O-C$_{||}$	-1.2200	-0.1260	0.4220	0.0000
H-C-O-C$_{||}$	0.0000	0.0000	0.1980	0.0000
C-C-C-O	1.3000	-0.05000	0.2000	0.0000

Table B4: Improper parameters used in term 4 in Equation B12.

Improper	K_ϕ (kcal mol^{-1})
=O-C-C$_{||}$-O	10.5

9,10-dimethyloctadecane (PAO-2)

$$CH_3$$

$$CH_2 \quad CH_2 \quad CH_2 \quad CH_2 \quad CH \quad CH_2 \quad CH_2 \quad CH_2 \quad CH_3$$

$$CH_3 \quad CH_2 \quad CH_2 \quad CH_2 \quad CH \quad CH_2 \quad CH_2 \quad CH_2 \quad CH_2$$

$$CH_3$$

Olefin Co-Polymer (OCP)

Ethylene monomers   Propylene monomers

$$-(CH_2-CH_2)_{43} \qquad \qquad \begin{bmatrix} CH-CH_2 \\ | \\ CH_3 \end{bmatrix}_{43}$$

Poly dodecyl methacrylate (PMA)

$$\begin{bmatrix} & O \\ & \| \\ H_2C \!\!-\!\! C \!\!-\!\! OCH_2(CH_2)_{10}CH_3 \\ | \\ CH_3 \end{bmatrix}_n$$

1-dodecyl methacrylate
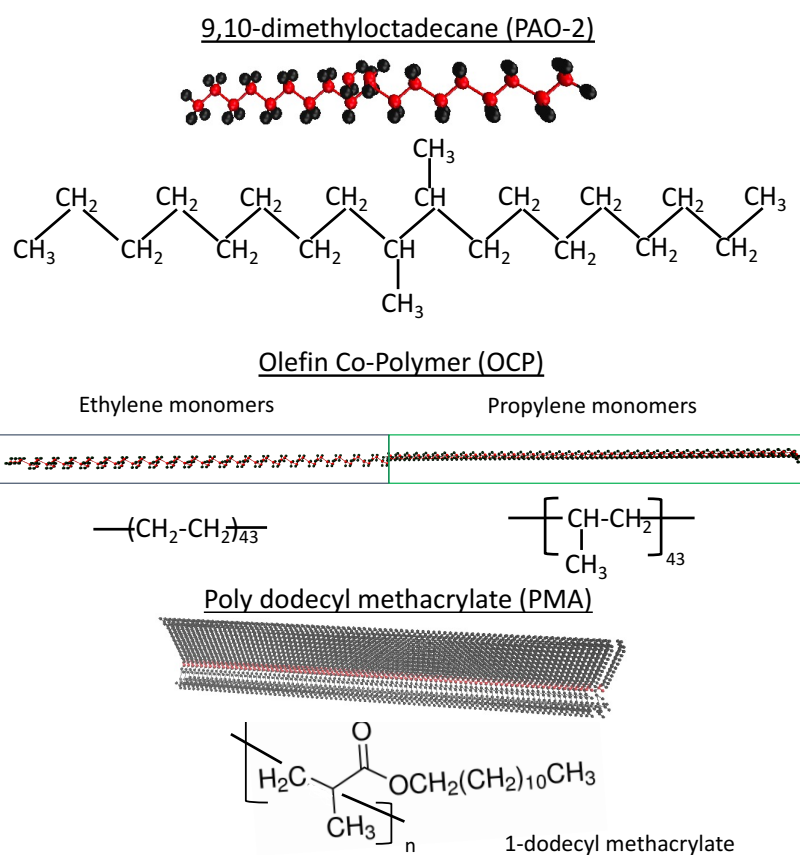
Figure B1: Schematics of the solvent - PAO-2 molecule, and polymer chains - OCP molecule and PMA molecule used in this simulation study.

Table B5: LJ parameters and partial charges of the atoms used in terms 5 and 6 in Equation B12.

| Atom type	ε_{ii} (kcal mol^{-1})	σ_{ii} (Å)	q_i (e$^-$)
All			
C_{CH_3}	0.066	3.5	-0.222
C_{CH_2}	0.066	3.5	-0.148
C_{CH}	0.066	3.5	-0.060
H_{CH_3}	0.030	2.5	0.074
H_{CH_2}	0.026	2.5	0.074
H_{CH}	0.030	2.5	0.060
PMA			
C_C	0.066	3.5	0.0
$C_{C-O-C=}$	0.066	3.5	0.190
$C_{\parallel}$	0.105	3.75	0.510
$O_{\parallel}$	0.210	2.960	-0.430
$O_{O-C=O}$	0.170	3.00	-0.330
H_{H-C-O}	0.015	2.42	0.030
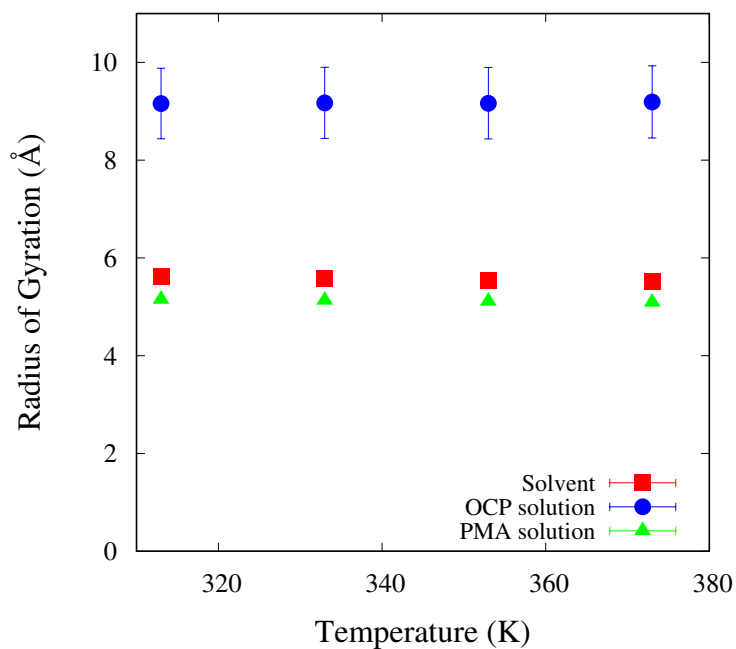
Figure B2: Hydrodynamic radius of PAO-2 as a function of temperature, T in pure solvent, OCP solution and PMA solution in the atomistic scale simulations.
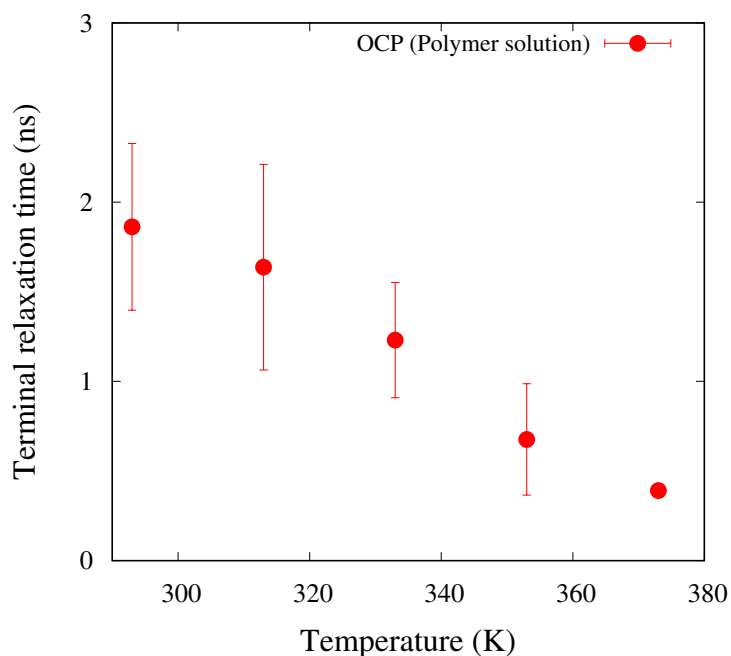

Figure B3: Terminal relaxation time of OCP polymer chain as a function of temperature, T in the atomistic scale simulations.

Mesoscale simulation

Table B6: Various parameters of mDPD simulations at 333 K.

OCP in PAO-2	
A_{ii}	-103.08
A_{ij}	-103.08
B_{ii}	41.61
B_{ij}	41.61
γ_{ij}	16.0
r_D	1.68
k_f	30.0
r_0	1.5
$k_{angle,1}$	2.15
$k_{angle,2}$	0.70

PMA in PAO-2	
A_{ii}	-103.08
A_{ij}	-103.19
B_{ii}	41.61
B_{ij}	41.61
γ_{ij}	16.0
r_D	1.68
k_f	30.0
r_0	1.5
k_{angle}	1.71

Table B7: Various parameters of mDPD simulations at 353 K.

OCP in PAO-2	
A_{ii}	-81.78
A_{ij}	-81.78
B_{ii}	32.46
B_{ij}	32.46
γ_{ij}	16.0
r_D	1.69
k_f	30.0
r_0	1.5
$k_{angle,1}$	2.15
$k_{angle,2}$	0.70

PMA in PAO-2	
A_{ii}	-81.78
A_{ij}	-81.83
B_{ii}	43.5
B_{ij}	43.5
γ_{ij}	16.0
r_D	1.69
k_f	30.0
r_0	1.5
k_{angle}	2.19
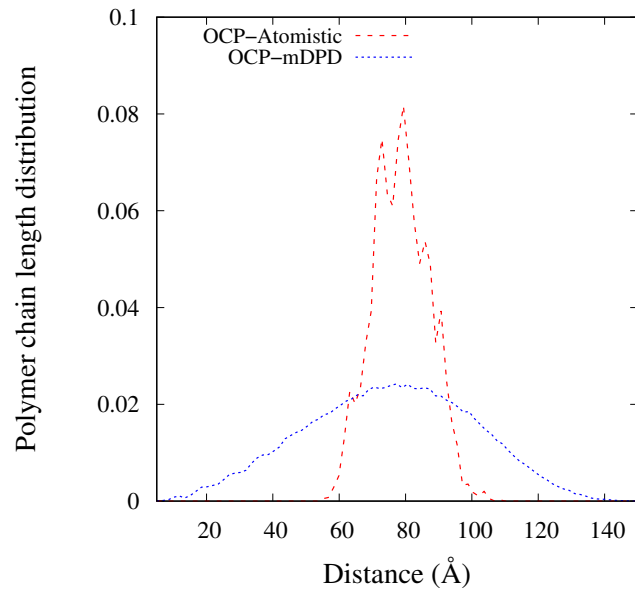
Figure B4: Polymer chain length distribution for OCP at 313 K in atomistic MD and mDPD.

Table B8: Various parameters of mDPD simulations at 373 K.

OCP in PAO-2	
A_{ii}	-60.015
A_{ij}	-60.015
B_{ii}	23.23
B_{ij}	23.23
γ_{ij}	16.0
r_D	1.78
k_f	30.0
r_0	1.5
$k_{angle,1}$	2.15
$k_{angle,2}$	0.70

PMA in PAO-2	
A_{ii}	-60.015
A_{ij}	-60.020
B_{ii}	23.23
B_{ij}	23.23
γ_{ij}	16.0
r_D	1.78
k_f	30.0
r_0	1.5
k_{angle}	2.89

Table B9: The properties of the PAO-2 system in mDPD units and corresponding values in real units at 333 K.

Property	mDPD units	Real units
Density (ρ)	7.9	0.764 g cm^{-3}
m$_b$	1.0	4.683×10^{-25} kg
r_C	1.0	16.9 Å
dt	0.01	0.17 ps
Energy (k$_B T$)	1.0	4.597×10^{-21} J
Pressure (p)	0.107	1 atm

Table B10: The properties of the PAO-2 system in mDPD units and corresponding values in real units at 353 K.

Property	mDPD units	Real units
Density (ρ)	7.9	0.748 g cm^{-3}
m_b	1.0	4.683×10^{-25} kg
r_C	1.0	17.03 Å
dt	0.01	0.17 ps
Energy ($k_B T$)	1.0	4.874×10^{-21} J
Pressure (p)	0.103	1 atm

Table B11: The properties of the PAO-2 system in mDPD units and corresponding values in real units at 373 K.

| Property	mDPD units	Real units
Density (ρ)	7.9	0.732 g cm^{-3}
m_b	1.0	4.683×10^{-25} kg
r_C	1.0	17.16 Å
dt	0.01	0.17 ps
Energy ($k_B T$)	1.0	5.150×10^{-21} J
Pressure (p)	0.099	1 atm
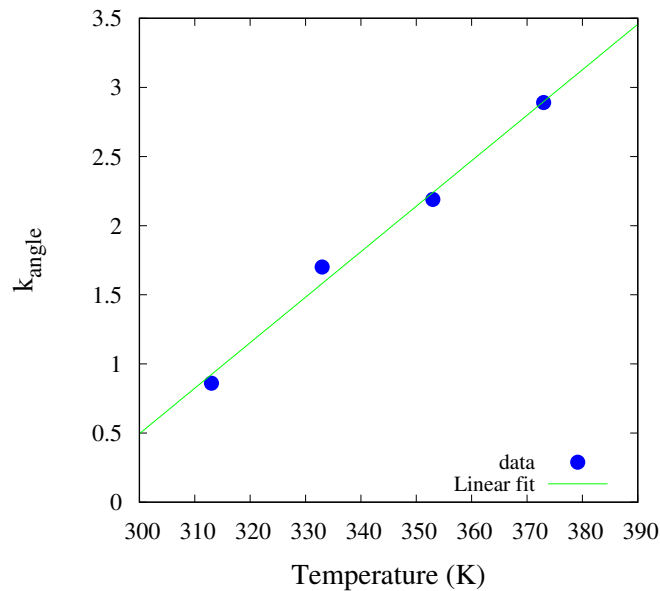
Figure B5: k_{angle} as a function of temperature, T for PMA.

Structural characteristics
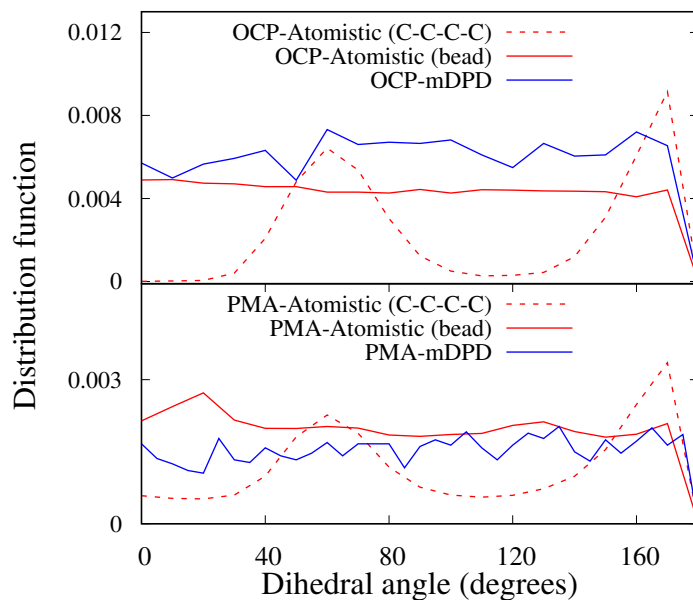
Figure B6: Dihedral distribution function of polymer chains in OCP solution (top) and PMA solution (bottom) at 313 K in the atomistic scale and mesoscale simulations. Under atomistic scale, the red dashed lines show the atomistic dihedral distribution between carbon atoms, and the red solid lines show the distribution of the dihedral angle of center of bonded beads as depicted in Figure 3.4b in Chapter 3.
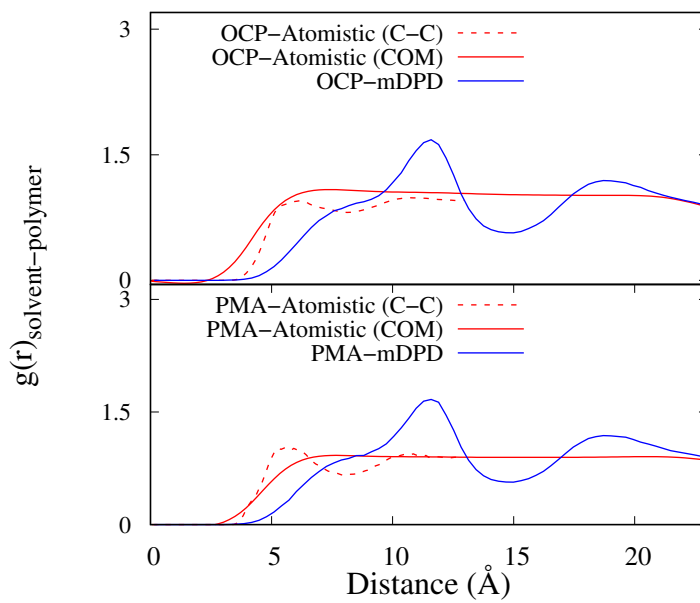
Figure B7: The radial distribution function ($g(r)_{solvent-polymer}$) between solvent and polymer beads in OCP solution (top) and PMA solution (bottom) at 313 K in the atomistic scale and mesoscale simulations. Under atomistic scale, the red dashed lines show the $g(r)$ between the carbon atoms of the solvent and polymer molecules, whereas the red solid lines show the $g(r)$ between the centre of mass (COM) of solvent bead and polymer chain beads equivalent to that in the mesoscale simulation. Mesoscale model shows more structural ordering than the atomistic scale model while comparing the blue and red solid lines.

Viscosity
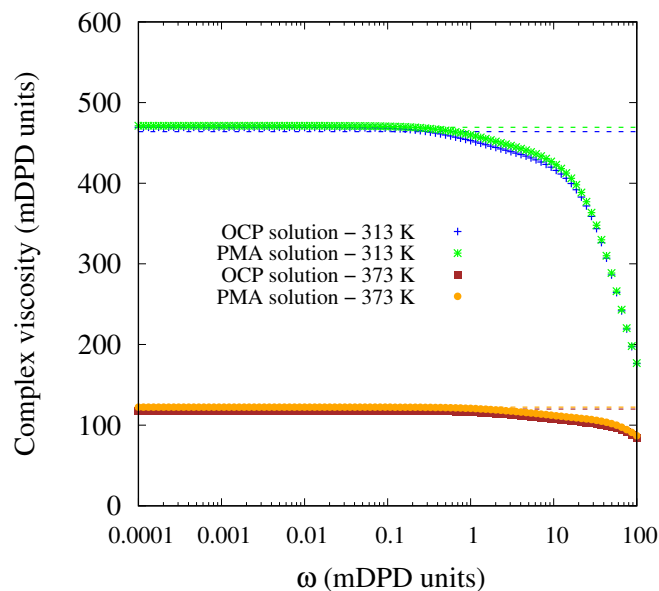
Figure B8: Complex viscosity ($\eta^*(\omega)$) as a function of ω for the OCP and PMA polymer solutions at 313 K and 373 K. The values agree with the η_0 from Green-Kubo equation [188].

Terminal relaxation time
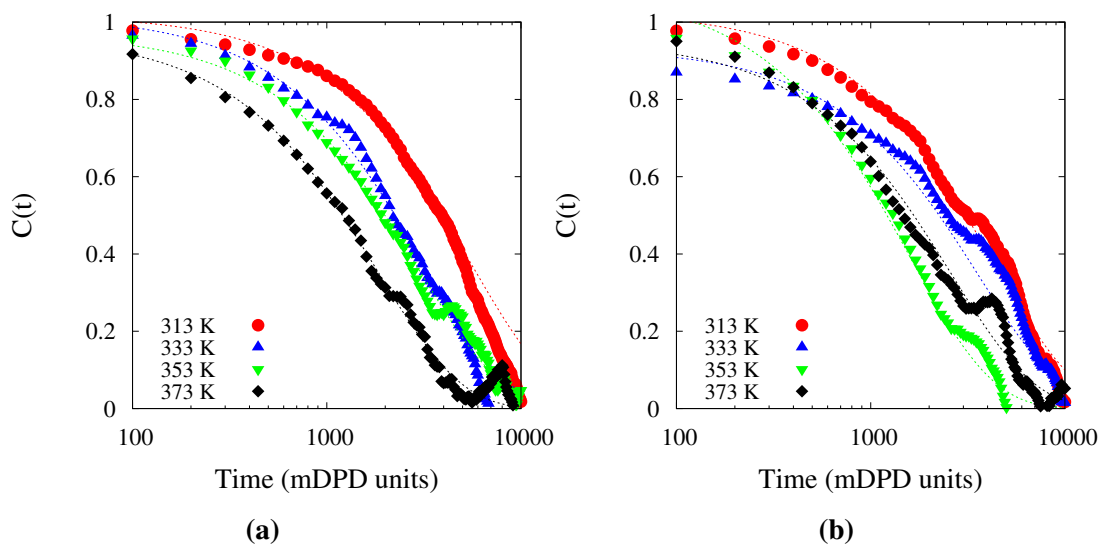
Figure B9: $C(t)$ as a function of time for (a) OCP polymer chain and (b) PMA polymer chain at different temperatures. The dashed lines show the exponential fit.

Table B12: Comparison of τ_Z from Equation 3.19 and τ_{term} from Equation 3.23.

Temperature (K)	τ_Z (mDPD units)	τ_{term} (mDPD units)
OCP		
313	2100	5455
333	1273	3287
353	984	2334
373	675	1824
PMA		
313	1800	4408
333	1332	3363
353	714	2014
373	780	2462

STATEMENT OF CO-AUTHORS of JOINT PUBLICATIONS

Titles of publications: 1) Dilute viscoelastic polymer solutions for dielectric heat transfer applications: A molecular dynamics study. 2) Multi-scale modelling of dilute viscoelastic liquids: Atomistic to mesoscale mapping of polymer solutions. 3) Atomistic exploration of viscoelastic nanofluids as heat transfer liquids for immersive- cooling applications.

Name of candidate: Bharath Ravikumar

Title of research thesis: Molecular dynamics modelling of complex-rheology heat transfer liquids

Name of first supervisor: Dr. Ioannis K. Karathanassis

We, the undersigned, co-authors of the above publication, confirm that the above publication has not been submitted as evidence for which a degree or other qualification has already been awarded.

We, the undersigned, further indicate the candidate's contribution to the publication in our joint statement below.

Signature:

Name: Dr. Ioannis K. Karathanassis
Date: 11th July 2024

Signature:

Name: Prof. Manolis Gavaises
Date: 11th July 2024

Signature:

Name: Dr. Timothy Smith
Date: 11th July 2024

Statement indicating the candidate's contribution to the publication

The candidate has contributed to the conceptualisation, methodology, validation, data curation, formal analysis, investigation, writing and visualisation of the articles.